# Characterization and simulation of the mechanical forces that control the process of Dorsal Closure during Drosophila melanogaster embryogenesis

Maxime Dureau

# THESE

en vue de l'obtention du grade de

**Docteur de l'Università degli Studi di Genova**

**En cotutelle avec l'Ecole Normale Supérieure de Lyon**

**Disciplines:** Physique & Sciences de la Vie

**Laboratoires:** Dipartimento di Ingegneria Meccanica, Energetica, gestionale e dei trasporti & Laboratoire de Biologie Moléculaire de la Cellule

**Ecoles Doctorales:** Scienze e Tecnologie per l'Ingegneria, corso Ingegneria Matematica e Simulazione & Biologie Moléculaire Integrative et Cellulaire

Présentée et soutenue publiquement le 29 juin 2015

Par Maxime Dureau

---

# Characterization and simulation of the mechanical forces that control the process of Dorsal Closure during Drosophila melanogaster embryogenesis

---

**Directeurs de Thèse:**

Patrizia Bagnerini, Stéphane Vincent.

**Après l'avis de:**

Jacques Demongeot, Professeur

Giorgio Battistelli, Professeur

**Devant un jury composé de:**

Jacques Demongeot, Professeur

Giorgio Battistelli, Professeur

Olivier Hamant, Directeur de Recherche

Stefano Vignolo, Professeur

Patrizia Bagnerini, Maître de Conférence

Stéphane Vincent, Maître de Conférence

UNIVERSITÀ DEGLI STUDI
DI GENOVA

**PhD Manuscript**

submitted in fulfillment of the requirements for the degree of
**Doctor of the Università degli Studi di Genova**
**Jointly with the Ecole Normale Supérieure de Lyon**

**Disciplines:** Physics & Life Sciences

**Laboratories:** Dipartimento di Ingegneria Meccanica, Energetica, gestionale e dei trasporti & Laboratoire de Biologie Moléculaire de la Cellule

**Doctoral Schools:** Scienze e Tecnologie per l'Ingegneria, corso Ingegneria Matematica e Simulazione & Biologie Moléculaire Integrative et Cellulaire

Presented & Defended publicly on June 29, 2015
By Maxime Dureau

---

# Characterization and simulation of the mechanical forces that control the process of Dorsal Closure during Drosophila melanogaster embryogenesis

---

**Tutors:**
Patrizia Bagnerini, Stéphane Vincent.

**After an opinion from:**

Jacques Demongeot, Professor
Giorgio Battistelli, Professor

**In front of a jury composed of:**

Jacques Demongeot, Professor
Olivier Hamant, Director of Research
Patrizia Bagnerini, Lecturer
Giorgio Battistelli, Professor
Stefano Vignolo, Professor
Stéphane Vincent, Lecturer

UNIVERSITÀ DEGLI STUDI
DI GENOVA

# Contents

# Summaries

## Français

Le travail de thèse présenté ici vise à caractériser et simuler les forces mécaniques impliquées dans le processus de fermeture dorsale chez l'organisme *Drosophila melanogaster*. Ce processus est embryonnaire: il est l'un des événements participant à la formation de la larve. En particulier, la fermeture dorsale participe à l'acquisition par l'embryon de sa forme finale par le biais de forces générées par de tissus cellulaires. Ainsi, l'objectif du travail présenté ici est d'approfondir nos connaissances sur la mécanique des tissus, ainsi que sur leur role dans l'embryogenèse.

Les tissus impliqués dans la fermeture dorsale sont l'épiderme et l'amnioséreuse. A ce stade du développement, l'épiderme entoure quasiment tout l'embryon. Cependant, l'amnioséreuse couvre encore une zone située du côté dorsal, appelée trou dorsal. La fermeture dorsale consiste donc en la fermeture de ce trou dorsale, ainsi qu'en la jonction des parties latérales de l'épiderme, dans un processus similaire à la cicatrisation.

Afin de réaliser la jonction de l'épiderme au niveau de la ligne dorsale, celui-ci doit être tracté. Cette traction est réalisée à la fois par l'amnioséreuse couvrant le trou dorsal, et par la rangée la plus dorsale de cellules de l'épiderme (Leading Edge cells). Celles ci participent à la fermeture de deux manières. D'une part, ces cellules forment un cable d'actine entourant l'ensemble du trou dorsal, qui, en se contractant, participe à réduire l'aire de l'amnioséreuse. D'autre part, les cellules du Leading Edge émettent des protrusions, qui s'arriment au Leading Edge opposé, et le tractent vers elles,

jusqu'à ce que les deux parties de l'épiderme fusionnent. Ces protusions ayant une taille limitée, la traction et la fusion (appelées aussi zipping) ne sont possibles qu'aux extrémités antérieures et postérieures du trou dorsal (appelées canthi), là où la distance entre les deux leading edge est suffisamment petite.

Par ailleurs, l'amnioséreuse tracte elle aussi l'épiderme vers la ligne dorsale. Elle produit des filaments d'actine et de la myosine (un moteur moléculaire), qui forment un réseau contractile au sein des cellules leur permettant de tirer sur les cellules du leading edge. Par ailleurs, les cellules de l'amnioséreuse voient l'aire de leur côté supérieur (côté apical) varier de manière périodique. Bien que ces variations d'aire aient été largement décrites, leur rôle dans la fermeture dorsale reste inconnu.

L'objet de cette thèse est d'améliorer notre compréhension des concepts mécaniques impliqués dans ces oscillations, et de construire un modèle physique représentant ces mouvements. Le travail présenté ici étudie aussi les mouvements des cellules du leading edge, dans le but de comprendre l'effet du cable d'actine sur la dynamique de la fermeture dorsale.

Afin d'étudier les mouvements des cellules et des tissus impliqués dans la fermeture dorsale, un algorithme permettant de détecter les contours des cellules, leur position ainsi que celle de leurs vertex (points de jonction entre trois à quatre cellules) et de suivre leur déplacements au cours du temps a été développé. Un interface utilisateur a été construit pour faciliter l'ajustement des paramètres permettant cette détection, ainsi que la correction d'erreurs éventuelles.

Différents modèles dynamiques ont ensuite été construits, prenant en compte les différents comportements mécaniques que les cellules peuvent avoir. Ces modèles ont été construits selon l'approche lagrangienne. Les systèmes d'équations dérivant des équations d'Euler-Lagrange ont été résolues numériquement, et leurs prédictions ont été comparées aux données issues de l'algorithme de détection selon l'approche des moindres carrés. Les résultats ont été validés en testant les résidus grâce à la fonction d'autocorrélation.

Finalement, la dynamique du leading edge a été étudiée en caractérisant les

mouvements des cellules situées à l'interface entre l'épiderme et l'amnioséreuse, grâce à l'algorithme de détection. Les dynamiques d'embryons non mutés (wild-type) ont été comparées à celles d'embryons portant une mutation affectant spécifiquement le cable d'actine.

Les résultats présentés dans cette thèse nous permettent de mieux comprendre les processus mécaniques impliqués dans les oscillations des cellules de l'amnioséreuse. Ils nous donnent aussi des indices sur leurs caractéristiques biologiques. Ils nous permettent enfin de mieux appréhender le rôle du cable d'actine dans ce processus proche de la cicatrisation.

# Italiano

Il lavoro di tesi presentato qui cerca di caratterizzare e simulare le forze meccaniche implicate nel processo di chiusura dorsale dall'organismo *Drosophila melanogaster*. Questo processo è embrionale: è uno dei avvenimenti che partecipano alla formazione della larva. In particolare, la chiusura dorsale partecipa all'acquisizione per l'embrione della sua forma finale attraverso le forze generate da tessuti cellulari. In tal modo, l'obiettivo del lavoro presentato qui è di approfondire i nostre conoscenze sulla meccanica dei tessuti, così come sul loro ruolo nell'embriogenesi.

I tessuti implicati nella chiusura dorsale sono l'epidermide e l'amniosierosa. A questo stadio dello sviluppo, l'epidermide cinge quasi tutto l'embrione. L'amniosierosa copre tuttavia ancora una zona localizzata del lato dorsale, chiamato buco dorsale. La chiusura dorsale consiste nella chiusura di questo buco dorsale, così come nella congiunzione delle parti laterali dell'epidermide, in un processo similare alla cicatrizzazione.

Per realizzare la congiunzione dell'epidermide al livello della linea dorsale, questo deve essere trainato. Questa trazione è realizzata al tempo stesso dall'amniosierosa che copre il buco dorsale, e per la fila più dorsale di cellule dell'epidermide, le Leading Edge cells. Queste partecipano alla chiusura di due modi. Da una parte, queste cellule formano un cavo di actine che cinge l'insieme del buco dorsale che, contrarsisi, participio a ridurre l'area dell'amniosierosa. D'altra parte, le cellule del Leading Edge emettono dei protrusioni che si stivano al Leading Edge oppositore, ed li tirano verso esse, finché le due parti dell'epidermide fondono. Questi protrusioni hanno una taglia limitata. Cosi, la trazione e la fusione, chiamate tanto zipping, sono possibili solamente alle estremità anteriori e posteriori del buco dorsale, chiamate canthi, là dove la distanza tra i due leading edge è sufficientemente piccola.

Peraltro, l'amniosierosa tira lei anche l'epidermide verso la linea dorsale. Produce dei filamenti di actine e del myosine, un motore molecolare che forma una rete contrattile in seno alle cellule. Questa rete permette loro

di tirare sulle cellule del leading edge. Peraltro, le cellule dell'amniosierosa vedono l'area del loro lato superiore, lato apicale, variare in modo periodico. Sebbene queste variazioni di area siano state descritte largamente, il loro ruolo nella chiusura dorsale resta sconosciuto.

L'oggetto di questa tesi è di migliorare la nostra comprensione dei concetti meccanici implicati in queste oscillazioni, e di costruire un modello fisico rappresentante questi movimenti. Il lavoro presentato qui studia anche i movimenti delle cellule del leading edge, nello scopo di comprendere l'effetto del cavo di actine sulla dinamica della chiusura dorsale.

Per studiare i movimenti delle cellule e dei tessuti implicate nella chiusura dorsale, un algoritmo che permette di scoprire i contorni delle cellule, la loro posizione così come quella dei loro vertici (punti di congiunzione tra tre a quattro cellule) e di seguire i loro spostamenti durante il tempo è stato sviluppato. Un interfaccia utente è stato costruito per facilitare l'adeguamento dei parametri che permettono questa localizzazione, così come la correzione di errori eventuali.

Differenti modelli dinamici sono stati costruiti poi, prendendo in conto i differenti comportamenti meccanici che le cellule possono avere. Questi modelli sono stati costruiti secondo l'approccio di Lagrangia. I sistemi di equazioni che derivano delle equazioni di Euler-Lagrange sono stati risolti numericamente, e le loro predizioni sono state paragonate ai dati generati dell'algoritmo di localizzazione secondo l'approccio degli minimi quadrati. I risultati sono stati convalidati provando i resti grazie alla funzione di autocorrelazione.

Finalmente, la dinamica del leading edge è stata studiata caratterizzando i movimenti delle cellule localizzate all'interfaccia tra l'epidermide e l'amniosierosa, grazie all'algoritmo di localizzazione. Le dinamiche di embrioni non mutante (wild-type) sono state paragonate a queste di embrioni che portano una mutazione che affetta specificamente il cavo di actine.

I risultati presentati in questa tesi ci permettono di comprendere meglio i processi meccanici implicati negli oscillazioni delle cellule dell'amnioséreuse. Ci danno anche degli indizi sulle loro caratteristiche biologiche. Ci perme-

ttono infine di temere meglio il ruolo del cavo di actine in questo processo vicino alla cicatrizzazione.

## English

The work presented here aims at characterizing and simulating the mechanical forces involved in the process of Dorsal Closure in the organism *Drosophila melanogaster*. This process is embryonic: it is an event participating in the formation of the larvae. In particular, Dorsal Closure participates in the acquisition of the final form of the embryo. Therefore, the work presented here aims at fathoming our knowledge on tissues mechanics, as well as their role in embryogenesis.
The tissues involved in Dorsal Closure are the epidermis and the amnioserosa. At this stage of development, the epidermis surrounds almost all the embryo. Nevertheless, the amnioserosa still covers a large area of the dorsal side called dorsal hole. Hence, Dorsal Closure aims at shutting this hole and joining the lateral sides of the epidermis, in a process similar to wound healing.
In order to fuse the two sides of the epidermis on the dorsal line, the epidermis must be drawn dorsalward. This movement is driven by the amnioserosa on the one hand, and by the dorsalmost row of the epidermis (called Leading Edge cells) on the other hand. The latter participate in Dorsal Closure in two ways. First, the Leading Edge cells form atranscellular Actin Cable around the dorsal hole. The cable, contracting, will reduce the area of the dorsal hole covered by te amnioserosa. Second, the Leading Edge cells emit protrusions that will attach to the opposite Leading Edge and drag it toward themselves, untill the two sides of the epidermis fuse. These protrusions have a limited range, hence the dragging and fusion only take place at the anterior and posterior ends of the dorsal hole (called canthi), where the distance between the two Leading Edges is small enough.
The Amnioserosa also drags the epidermis toward the dorsal line. Its cells produce actin filaments and myosin (a molecular motor), that will form a contractile network within the cells. Interstingly, Amnioserosa cells see the

area of their top side (apical side) vary in a periodic way. Although these variations have been widely studied, their role in Dorsal Closure remains unknown.

This PhD aims at improving our knowledge of the mechanical concepts involved in these oscillations, and to build a physical model representing these movements. The work presented here also studies the movements of the Leading Edge cells, in order to understand the effect of the Actin Cable on the dynamics of Dorsal Closure.

In order to study the cells movements and the role of the tissues involved in Dorsal Closure, an algorithm was developped, allowing to detect the cells edges, their position, as well as those of their vertices (multiple junction between three or four cells) and to track them over time. A user interface was also developped, in order to facilitate the adjustment of the parameters allowing the detection, as well as the correction of possible errors.

Various dynamical models were then built, taking into account the possible mechanical behaviors cells may have. These models were built following the lagrangian approach. The systems of equations deriving from the Euler-Lagrange equations were numerically solved, and their predictions compared to the biological data extracted thanks to the algorithm presented earlier, following the least square approach. The model validation was performed thanks to the autocorrelation function test.

Finally, the Leading Edge dynamics was studied characterising the cellular movements at the interface between the epidermis and the amnioserosa. Wild type embryos dynamics were compared to those of mutated embryos showing specific defects in the Actin Cable formation.

The results presented in this manuscript allow a better understanding of the processes involved in in Amnioserosa cells osciclations. They also give clues on their biological characteristics. Finally, they assess the role of the actin cable in this process similar to wound healing.

# Chapter 1

# Introduction

This doctoral thesis aims at improving our understanding of biological phenomena with mean coming from physics. The system chosen for the following work is Dorsal Closure, a developmental event occurring during the embryogenesis of the model organism *Drosophila Melanogaster*.

## 1.1 The *Drosophila Melanogaster* model

A model organism is an organism extensively studied to understand biological phenomena, viewing to extend these discoveries to other organisms, and in particular, to humans. *Drosophila Melanogaster* is a well-known model organism used in laboratories for over a century.

### 1.1.1 A brief history of flies in science

#### First uses of the fruit fly

Scientists began to use *Drosophila Melanogaster*, also called fruit fly, or vinegar fly, for experimental purposes in the first decades of the $XX^{th}$ century. Although Charles W. Woodworth is credited to be the first to extensively breed fruit flies, and for suggesting that these species could be used for genetic studies, the first experimental studies on the *Drosophila Melanogaster*

as a model organism began in 1909 under the direction of Thomas Hunt Morgan at Columbia University.

Thomas Morgan's early work on drosophila focused on sex determining factors [1], [2]. At this time, the Sutton-Boveri theory, or chromosome theory of inheritance, developed by Teodor Boveri and Walter Sutton in the first years of the $XX^{th}$ century, was slowly settling. Chromatin was first observed by Walther Friedmann in 1879, who later discovered the pairs of chromosomes. Mitosis was described during the following decades, meiosis discovered in 1905 by J.B. Farmer and J.E.S. Moore, and XY the sex-determination system was first suggested by E.B. Wilson and Nettie Stevens the same year [3].

T.H. Morgan gave a proof of this sex-determination system thanks to the drosophila model. He crossed white-eyed male fruit flies with red-eye female flies, and then the 100% red-eyed progeny together, in the first test cross ever performed with *Drosophilas*. While Mendel's laws predicted a gender-independent repartition of red and white-eyed flies, Morgan got every 100% of the females with red eyes, and an equal repartition of red and white eyes in males, as shown in Figure 1.1. These ratios can only be understood considering that the eye color character is transmitted through the "accessory chromosomes" proposed by Wilson and Stevens.

Let us consider that males carry only one X chromosome, and an other one called Y not accounting for eye color, while females carry two X chromosomes. Let the white-eye allele be recessive. Hence, crossing red-eye females with white-eye males as shown in Figure 1.2a, one expects every fly in the first generation of the test cross to have red eyes. Female progeny will carry both the red-eye X chromosome ($X^+$) and the white-eye X chromosome ($X^W$). The white eye allele being recessive, they will have red eyes. Males, on the other hand, will carry the Y chromosome given by the father, not determining eye color, and the X chromosome from the mother: $X^+$. At this

| Cross | Outcome | |
|---|---|---|
| | Expected Phenotypes | Observed Phenotypes |
| P1 Red ♀ × P1 White ♂ | F1 = All Red | F1 = All Red |
| F1 Red ♀ × F1 Red ♂ | 75% Red ♀ and ♂<br>25% White ♀ and ♂ | 50% Red ♀<br>25% Red ♂<br>25% White ♂ |

**Figure 1.1:** *Expected test cross results according to Mendel laws versus Morgan's results. Morgan's results show a gender-related bias. [4]*

point, statistics do not show any difference with Mendel law's predictions.

Differences arise with the next generation (Figure 1.2b): crossing $X^+X^W$ females with $X^+Y$ males, Morgan obtained a progeny where every female had red eyes: they inherited the $X^+$ chromosome from their father, and thus had red eyes, regardless of the chromosome given by the mother. Males would receive the Y chromosome from their father, and hence, their eye color would be determined by the chromosome they received from their mother: 50% chances to receive the $X^+$, 50% to receive the $X^W$. Mendel laws couldn't explain these results: they are bound to somatic (non sexual) chromosomes. These statistics could only arise from the idea that sex is determined by "Accessory chromosomes", having a different inheritance pattern. Just by watching *Drosophilas* eye color, Morgan was able to determine the existence, and the importance in gender determination, of these sexual chromosomes.

Later on, still working with *Drosophila*, Morgan studied recombination and genetic linkage, i.e. the tendency of characters to be transmitted together. Gathering data on genetic linkage, and considering that this linkage was due to a physical proximity on chromosomes, he was able to build the first genetic maps representing the position of genes on chromosomes [5]. He received the first Nobel Prize rewarding a work on *Drosophila* in 1933, "for

| | | Male Gametes | |
|---|---|---|---|
| | | $X^w$ | $Y$ |
| Female Gametes | $X^+$ | $X^+X^w$ | $X^+Y$ |
| | $X^+$ | $X^+X^w$ | $X^+Y$ |

**(a)** *Cross table of Morgan's first cross.*

| | | Male Gametes | |
|---|---|---|---|
| | | $X^+$ | $Y$ |
| Female Gametes | $X^+$ | $X^+X^+$ | $X^+Y$ |
| | $X^w$ | $X^+X^w$ | $X^wY$ |

**(b)** *Cross table of Morgan's second cross.*

**Figure 1.2:** *Morgan's crosses tables for sexual chromosomes. $X^W$ stands for the chromosome carrying the recessive white-eye allele, and $X^+$ for the chromosome carrying the dominant wild type red-eye allele. [4]*

his discoveries concerning the role played by the chromosome in heredity".

These studies were the first step in the building of the knowledge of both drosophila's genetic, and the genetic toolbox that makes the fruit fly such a handy lab animal nowadays.

### Other major discoveries through fruit flies

T.H. Morgan's outstanding results with the *Drosophila* model subsequently encouraged other scientists to use this species for experimental biology. Since then, many great scientific advances stem from works on the fruit flies. Only taking into account Nobel Prizes, four other major discoveries have to be remembered.

Hermann Joseph Muller (one of Thomas Morgan's students) was awarded the Nobel Prize of Physiology and Medicine in 1946 "for the discovery of the production of mutations by means of X-ray irradiation", work published in 1927. Irradiating flies with various doses of X-rays, he found a correlation between the amount of radiation received and the number of lethal muta-

tions appearing in flies. He later communicated on the dangers of radiations for humans. Later on, his work also allowed scientists to generate genetically modified flies, for instance to assess the effect of mutated genes [6].

In a paper released in 1980 [7], and later works [8], Christiane Nusslein-Volhard and Eric F. Wieschaus used the full potential of *Drosophila* in experimental biology: they produced mutations in flies DNA randomly using Ethyl methanesulfonate, and analyzed the effects of these mutations on over 40 000 flies lines in just three years of time. They were then able to identify which gene was mutated for each embryonic defect they monitored. They discovered that of the 13 000 genes in *Drosophila*'s genome, 5000 were important for embryonic development, and 140 were critical. They identified numerous genes that are critical for embryonic shape establishment, not only in *Drosophila*, but also in all *Metazoans* (animals). With this screen, they unveiled a large part of the mechanism allowing multicellular organisms to form from one single cell. For this work, they were awarded the Nobel Prize in 1995 together with Edward Lewis, "for their discoveries concerning the genetic control of early embryonic development".

Two others Nobel Prizes awarded findings on *Metazoan* systems were due to *Drosophila*. In 2004, Richard Axel and Linda Buck, "for their discoveries of odorant receptors and the organization of the olfactory system" - a work mostly performed on rats though. And in 2011, Jules Hoffman, Bruce Beutler and Ralph Steinmann for their discoveries around innate and adaptive immunity. The former working on *Drosophila*, and the two latter on mice, their work unraveled a shared system to protect both insects and mammals against microbes. The two formers, in particular, identified a family of genes responsible for anti-fungal and anti-microbian reactions both in *Drosophila* and Mammals.

These works made the fruit flies an organisms of a great importance in Biology. This non-exhaustive list of findings shows how much can be

learned from this organism. Used at first because of its breeding convenience, drosophila has now become a major model organism.

### A convenient fly

There are several reasons why the fruit flies are used on a large-scale in laboratories. First of all, *Drosophila melanogaster* is very convenient on the context of a laboratory. They are cheap to feed, can be stocked in large amounts in small spaces, and are vastly bred, since their generation time is only two week.

This short generation time offers great possibilities in the genetic field. Together with the fact that fruit flies have only four pairs of chromosomes (three autosomal and one sexual), that female have a very high fecundity (roughly 100 eggs per day), it enables the geneticists to generate great amounts of lines (producing mutations or insertions for instance), and to study them over several generations, in a reasonable amount of time.

Interestingly, although *Drosophila* is evolutionarily more distinct from human than other model organisms, such as mouse or rat, it still shows a astonishing genetic similarity with mammalians in general. In fact, 75% of the genes involved in human disease have homologs in *Drosophila*, and 50% of the proteins produced by the fruit flies cells match a protein found in mammals. In view of this, *Drosophila* comes very handy, since they are much more convenient for experimentations than other species closer to humans, while they still show a satisfactory genetic similarity with us.

### 1.1.2 *Drosophila*'s development

#### *Drosophila*'s life cycle

Drosophila life and reproduction cycle is short. Under ideal conditions ($25°C$), their development is achieved from one generation to the next in 10 days. The egg, under such conditions, achieves its embryogenesis in approximately 12 to 15 hours, and then hatches. The resulting larva develops during 4 days, molding twice in the process, one and two days after hatching. The larva will then encapsulate in the pupa, and undergo metamorphosis for about four days. The adult fly will then emerge, and it will take another 8 to 12 hours for the females to become fertile. *Drosophila* are then ready to start another life cycle.

#### *Drosophila*'s embryogenesis

In what follows, we will focus on particular features of *Drosophila* embryo. We will describe briefly the fruit fly's egg maturation. Pictures of a few embryonic stages are presented in Figure 1.3.

*Drosophila* embryogenesis is divided in seventeen stages regrouping every event necessary to go from the unicellular state right after fertilization to the ready-to-hatch larva [9, 10].
During the first four stages, the embryo undergoes thirteen nuclear divisions, with no membrane division. The embryo becomes a huge cell containing a great number of nuclei. The embryo also experiences some morphological changes (buds appearing and disappearing on the membrane, nuclei positioning at the periphery). Cell walls start to appear at stage 5, in a process called Cellularization. Midventral cells are also preparing for their later invagination. These stages last altogether roughly three hours.

Midventral cells invagination starts at stage six: ventral cells enter the gastrulation process, forming a tissue called the ventral furrow. Mesoderm and endoderm originate from these cells. A groove also appears at the an-

terior part, marking the separation with the future head. At stage seven, precursor tissues to the gut also invaginate. At stage 8 to 10, precursor cells to the digestive system keep on invaginating, while the germ band (an embryonic tail) is formed. The germ band is a ventral band of cells, that expands and folds at the posterior end of the embryo, to eventually colonize the dorsal side. Driven by a convergence and extension phenomenon (cells intercalate to increase the number of cell "columns", and then expand along the anterio-posterior axis), germ band eventually becomes a u-shaped structure surrounding the Amnioserosa. In the beginning of germ band extension, the yolk sac (a nutrientfull bag) is also formed, and cells precursors to the neural system (neuroblasts) start to multiply. At this point, the embryo has approximately reached its fifth hour of development.

During the eleventh stage, the embryo experiences a major growth phase, while parasegmental grooves start to form, and mandibula, labium and maxilla begin to appear. At this stage, the Germ Band has reached its maximal extension.

At stage twelve, the Germ Band starts to retract, due to its traction by Amnioserosa, and by a lengthening of germband cells along the Dorso-Ventral axis, and a shortening in the Antero-Posterior axis. The germ band hence widens Dorso-Ventrally during the process, and the Amnioserosa cells, which were elongated at early stage twelve, widen Antero-Posteriorly. The Germ Bands movement causes one part of the gut (hindgut) to relocate at the dorso-posterior part of the embryo, while the two other parts (anterior and posterior midgut) fuse. The epidermal segments also form during the process.

At stage 13, the Germ Band retraction is complete, leaving the Amnioserosa to cover the dorsal hole previously occupied by the Germ Band. The Head Involution, aiming at covering the head with epidermis, and Dorsal Closure, both start during stage thirteen. Dorsal Closure consists in

achieving the junction between the left and right sides of the epidermis, separated by the Amnioserosa at the time, on the dorsal midline of the embryo.

During stage fourteen, these two event continue, while the anal plate moves ventrally from the posterior tip and the spiracles (external tracheal apertures) become evident. At early stage fifteen, Dorsal Closure and Head Involution are finished, and the guts have achieved a full fusion, and now enclose the yolk sac. During stage 16, the epidermis reaches the full segmentation that will be present in the larva. This segmented body plan is important: the segments formed during embryogenesis are closely related to those of the adult fly, and each adult segment is specialized in forming particular structures (wings, legs...). At stage 17, the trachea are filled in with air, and the larva hatches.

The *Drosophila* Embryonic Stages were presented here in a short and simplified description of some of the processes required to form a healthy larva, i.e. to perform a proper development. Many events of a great importance weren't thoroughly introduced, the goal of this paragraph being to give an overview of *Drosophila*'s embryogenesis. In their globality, these processes are of many types, and serve many purposes, from the acquisition of cell and tissue identity to the shaping of the future larva. In the next section, we will present an event belonging to the latter type, event which is the subject of study of this thesis: Dorsal Closure.

## 1.2 The actors of Dorsal Closure

As presented earlier, Dorsal Closure is an embryonic event occurring between stage 13 and 15, i.e. approximately between the tenth and the twelfth hour of development. It aims at fusing the lateral sides of the epidermis on the dorsal midline, in a process similar to wound healing. To reach a proper closure, and in order to achieve an accurate pairing of epidermal segments

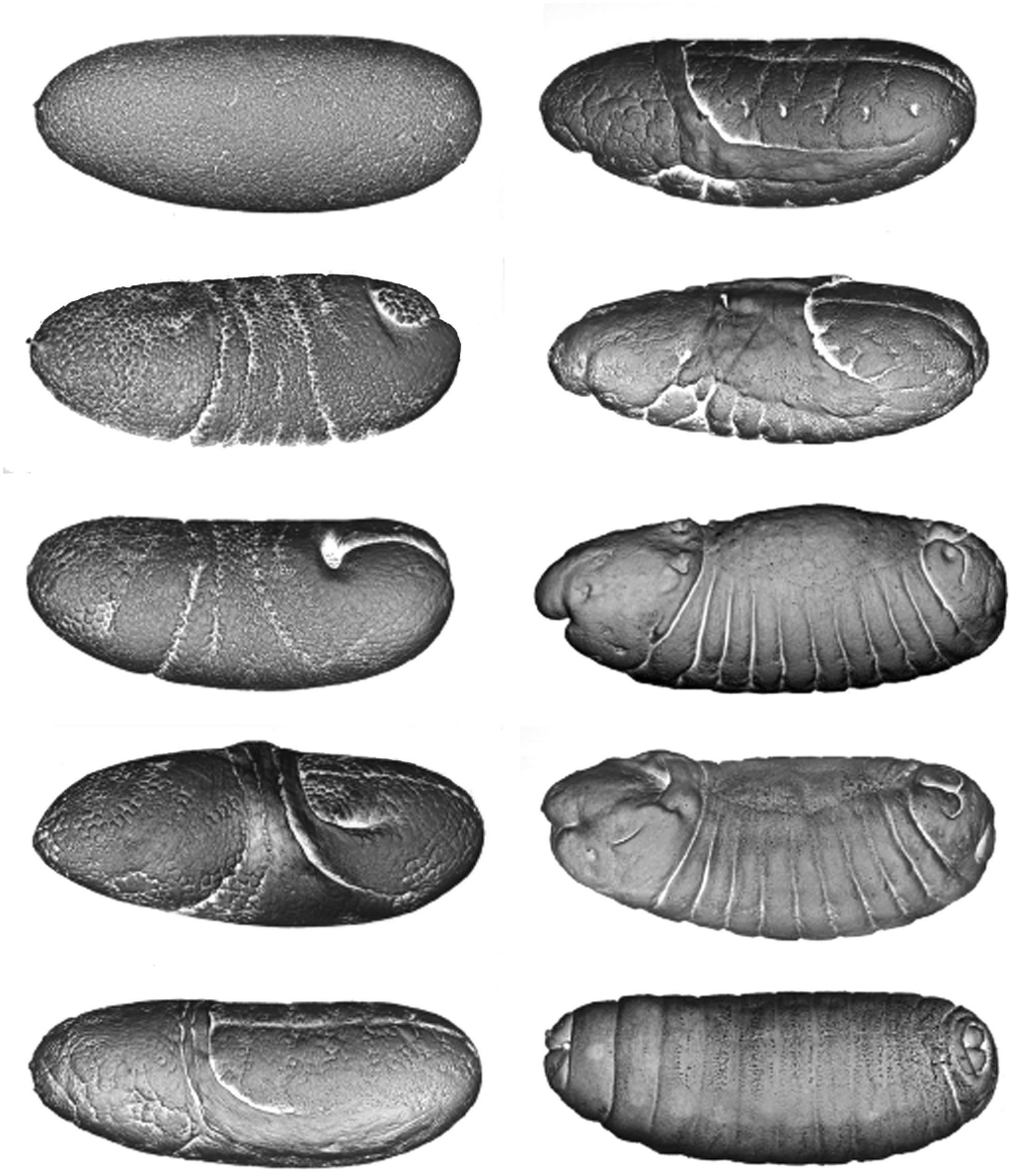

**Figure 1.3:** *Table of several embryonic stages. Pictures taken thanks to electronic microscopy. [11]*

(each segment has to fuse with the corresponding one on the other side of the epidermis), several motors of closure are required.

There are three of them:

- The Zipping: at the Canthi (i.e. the antero-posterior extremities of the eye-shaped Dorsal Hole), protrusions (filopodia) sent by the dorsal-most epidermal cells (Leading Edge cells) of both sides of the epidermis fuse with the opposite Leading Edge, and pull both sides of the epidermis toward each other. Filopodia also allow segment recognition. They only fuse with cells of the same segment than the cell from which they originate, allowing to achieve a proper segment matching [12].
- The Actin Cable: a transcellular structure produced by the Leading Edge cells, made of actin (a filamentous protein) and non-muscular Myosin II (a contractile protein). The Actin Cable surrounds the whole dorsal hole, and, contracting, tends to reduce the hole's surface.
- The Amnioserosa: Amnioserosa is an extra-embryonic tissue (i.e. a tissue that will not form any tissue nor organ in the larva) that covers the Dorsal Hole. Forming acto-myosin complexes, Amnioserosa cells pull both sides of the epidermis toward the dorsal midline. The tissue is eliminated during the process through area reduction and cell death.

Those structures and tissues are of great importance for the proper achievement of Dorsal Closure. In the following sections, we will detail their roles and known behaviors.

### 1.2.1 The Zipping

The zipping is most important in the last steps of Dorsal Closure, when epidermal cells are close enough to each other. Every cell of the Leading Edge sends protrusions, called filopodia, toward the center of the dorsal hole. Filopodia have a limited range, and hence manage to connect with the opposite Leading Edge only when it is close enough, i.e. at the canthi, or

toward the end of dorsal closure. Therefore, zipping is mainly responsible of the eye-shaped form of the dorsal hole: the dorsal edge of the epidermis is convex at the extremities, and concave in its center.

The zipping also serve a second function: segment recognition. Indeed, epidermal cells have various identities, and the location of these identities follows a specific spatial pattern. It is visible on the last three pictures of Figure 1.3 that the epidermis of the embryo has areas separated by grooves: they are the segments. These segments' appearance is due to complex gene interactions during embryogenesis.

Segment formation begins with the diffusion of maternal factors like *bicoid* or *caudal* from the anterior and posterior extremities of the embryo and inward. These factors activate the transcription of a group of genes called "Gap genes" (hunchback, knirps for instance) coding transcription factors. Each of these gap genes encompass wide zones of the epidermis, covering areas that will give rise to several segments. These genes act as regulators for each other, as well as for another set of genes: the pair-rule genes. The pair-rule genes (such as even-skipped or hairy) are present in seven stripes on the embryo, each stripe covering every other segment. They are to set the transcription of another class of genes: the segment polarity genes (wingless, hedgehog, engrailed...). Most of these genes are expressed in the fourteen pre-segmentary stripes. As their names suggests, they give a polarity to the segments, i.e., between the grooves separating each segment, different cell types are found in the anterior and posterior halves. The result of this cascade is an embryo with spatially repeated expression patterns, and cell identities [13].

Therefore, different cellular identities are present in the epidermis, with a spatially periodic pattern. In addition, each segment will have a particular purpose to form the adult fly. On one will be formed the wings, on another one pair of legs... Hence, it is important that, when joining both sides of the

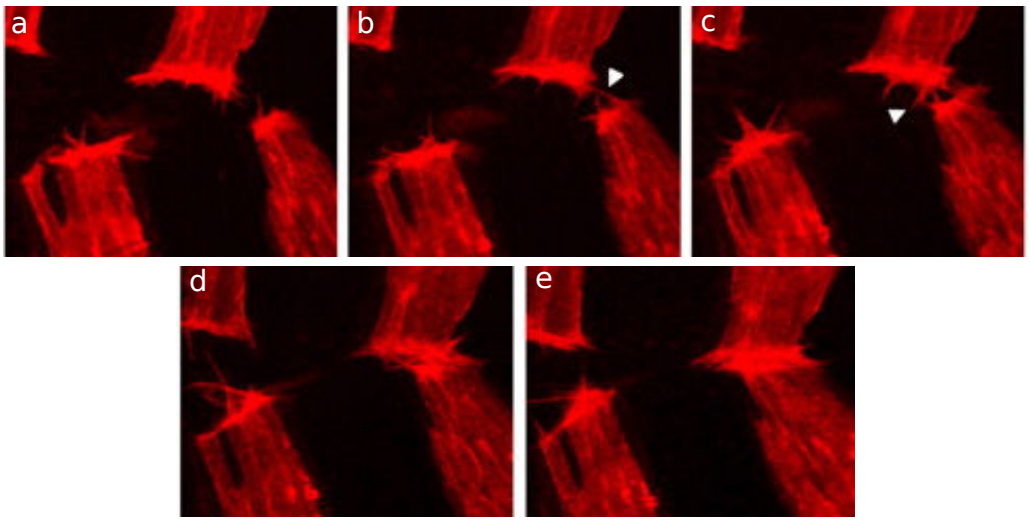


**Figure 1.4:** *Still images of a live movie of an embryo expressing Engrailed-Gal4, together with UAS-Moesin-RFP. In red, the sub-segmental compartments expressing the segment polarity gene Engrailed. In (a), filopodia are send over the dorsal hole but don't find any corresponding filopodia to fuse with. In (b) and (c), one can see filopodia meeting over the dorsal hole, and then pulling the segments toward each other to perform fusion ((d) and (e)). [12]*

epidermis, each segment fuses with the corresponding one on the other side of the epidermis. The zipping serves this purpose. Indeed, when exploring the space in front of them, the filopodia only fuse with other cells or other filopodia of the same cell type and segment than themselves [14]. An example of cell matching is shown in Figure 1.4.

### 1.2.2 The Actin Cable

Another effector of Dorsal Closure is the Actin Cable. It is a transcellular structure of non-muscular Myosin II, and actin filaments. The Actin Cable is located at the dorsal-most edge of the Leading Edge cells, and goes from a cantus to another and further, in the cells that used to be part of the Leading Edge, before they fused with the opposite edge [16, 17].

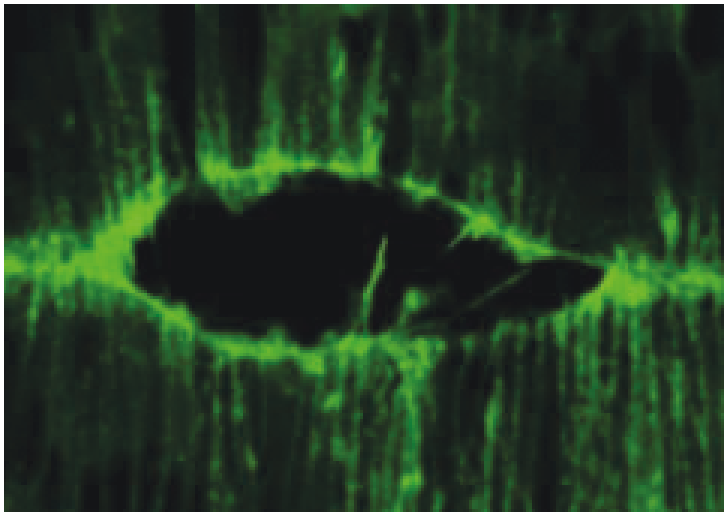

**Figure 1.5:** *Still confocal image of an embryo expressing actin::GFP, displaying the Actin Cable at the border between the Amnioserosa and the Epidermis, as well as the filopodia. [15]*

First discovered in the early nineties, it plays a significant part in closure's dynamics. Indeed, when the actin cable is disrupted (by laser cuts, or genetic impairment), the closure processes in a slower manner [18]. It was also found that the structure of the Leading Edge cells was impared [19]. When the cable is present, the Leading Edge cells display a shape stretched dorso-ventrally, while when it is absent, the stretching is less visible, and the orientation of their longest axis is rather random.

Being an important actor of closure, the effect of the Actin Cable on closure dynamics has extensively been studied. Several studies assessed for instance the mechanisms underlying its appearance. The Jun-Kinase and Dpp pathways are known to be involved in the differentiation of the first dorsalmost rows of epidermal cells [20–22]. Yet, the acquisition of polarity they induce is not sufficient for the Actin Cable to appear. A step gradient of Echinoid, a transmembranar protein, is also required between the Amnioserosa and the Epidermis [23]. This gradient was shown to appear at the onset of Dorsal Closure, when Amnioserosa stops to produce the Echi-

noid protein, and coincide with the appearance of the Actin Cable. When Amnioserosa cells express ectopically Echinoid, causing the step gradient to disappear, the Actin Cable does not form.

Nevertheless, although the impairment of Actin Cable have a significant impact on the closure speed, the affected embryos still manage to achieve a complete closure [18]. The Amnioserosa is in fact able to achieve Dorsal Closure by itself [24].

### 1.2.3 The Amnioserosa

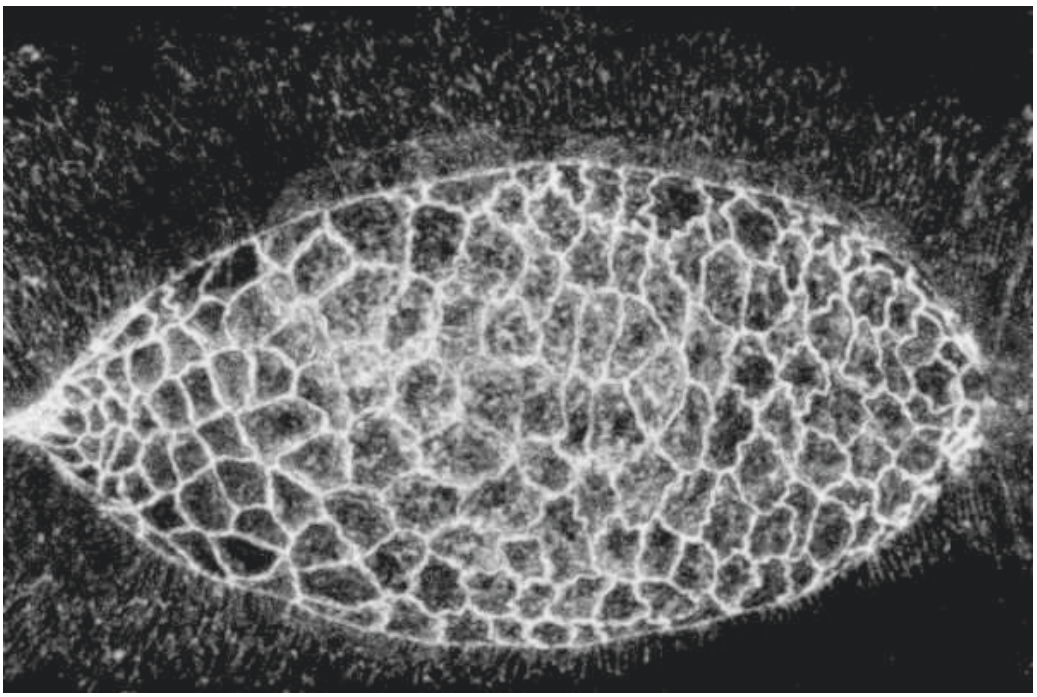

**Figure 1.6:** *Still confocal image of an embryo expressing DE-Cadherin::GFP, showing the Amnioserosa at the beggining of Dorsal Closure, surrounded by the epidermis.*

The Amnioserosa is an extra-embryonic tissue, i.e. it is a tissue present in the embryo, but that will not form any structure in the living larva, and

therefore needs to be removed by the end of the embryogenesis.

The Amnioserosa is a squamous (i.e. made of wide, flat cells) epithelium. It originates from the cellular blastoderm, an epithelium surrounding the whole embryo at stage five, right after Cellularization. At stage six, during gastrulation, the Amnioserosa is formed, and partly covers the central dorsal part of the embryo. During Germ Band elongation, the Amnioserosa and its cells are stretched, forming a long and narrow tissue joining each sides' base of the Germ Band [10], as it is visible in the second picture of the right panel in Figure 1.3. During Germ Band retraction, the amnioserosa pulls the base of the Germ Band toward the central dorsal part of the embryo, participating in its retraction [25]. When this process is over, the Amnioserosa is made of flat, wide cells, surrounded by the epidermis, and its cells start to pulse: their apical area undergoes periodic variations, driven by the alternate aggregation and disaggregation of an acto-myosin complex at their center. The apical area of Amnioserosa cells oscillates in antiphase with the amount of central Myosin II (Figure 1.7, panels A, B & C, [26,27].). Dorsal Closure starts by the time Amnioserosa cells start to pulse.

Interestingly, some of the amnioserosa cells experience apoptosis during Dorsal Closure. These events, triggered by mitochondrial Reactive Oxygen Species [28], are rather rare (around 10% of Amnioserosa cells undergo apoptosis), but yet, they account for an increase of 40% of the closure speed. This process was called Apoptotic force, and is thought to increase the tension accumulated in the Amnioserosa. Indeed, the cells surrounding the dying cell show a stretch toward that dying cell, and this stretch eventually disappear. Hence, Toyama et al. [29] propose that tension is generated by the loss of cells, is first transmitted to their nearest neighbor and then throughout the whole tissue, therefore fastening the Dorsal Closure.

The Amnioserosa plays a part in the Germ Band retraction, as a tissue able to exert a pulling force on the Germ Band [25,30]. The participation

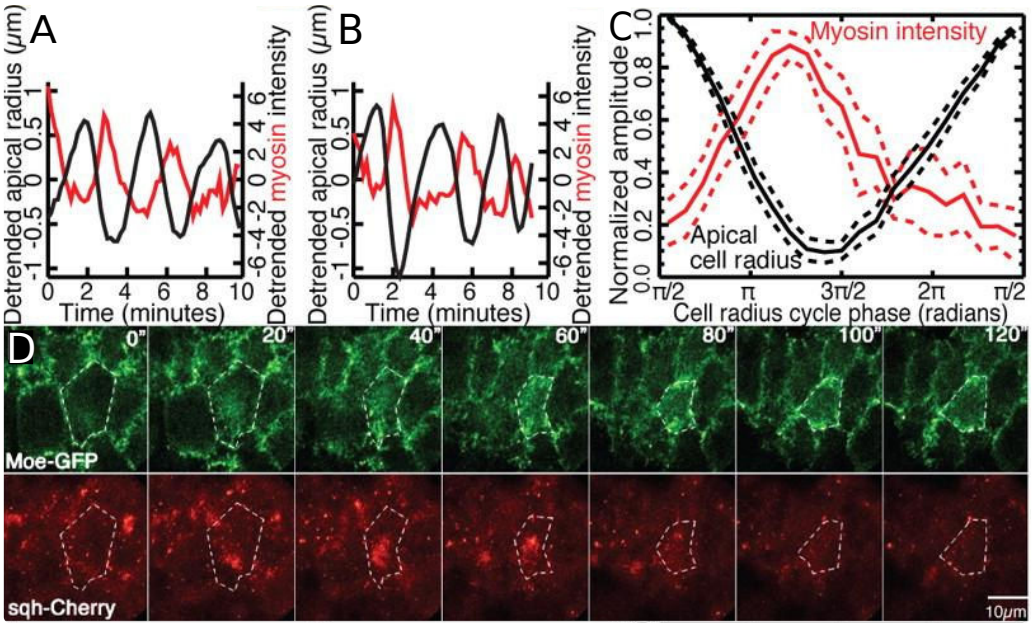


**Figure 1.7:** *A & B: plots of the apical radius of two amnioserosa cells, versus the intensity of central Myosin II fluorescence. C: Mean values of apical mean radius, versus Myosin II intensity. D: Still images of a confocal movie, of an embryo expressing a fusion of Myosin II Heavy Chain (Moesin) with GFP, together with a fusion of Myosin II Regulatory Light Chain (Spaghetti Squash) with mCherry (a red fluorescent protein). [27]*

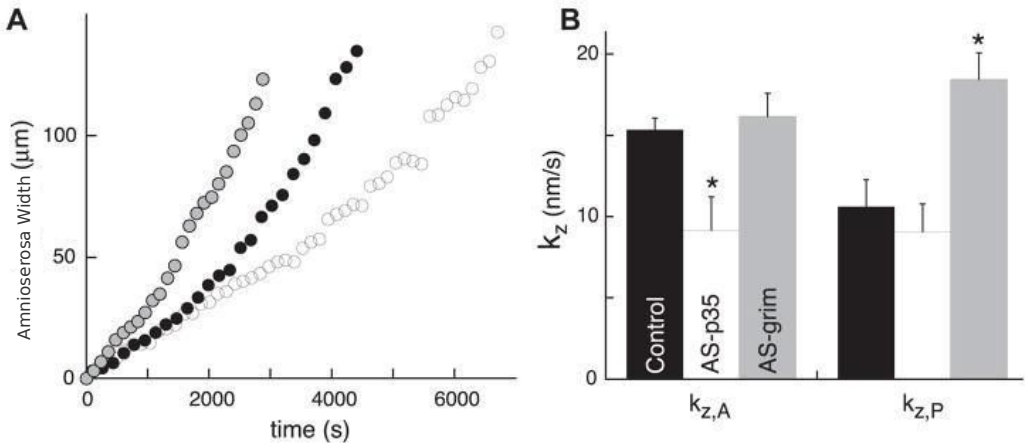


**Figure 1.8:** *A: Amnioserosa advancement: the width at a given time is subtracted to the original width. In black, the control cases, in white, embryos showing no cell death, and in grey embryos with an increased cell death. B: Closure speeds in control embryos (in black), in embryos expressing p35 (an inhibitor of apoptosis, in white), and in embryos expressing grim, a gene triggering apoptosis, in grey. [29]*

of the Amnioserosa is required to achieve the process, even though it leads to the disappearance of the tissue. In fact, it was recently shown that without the Amnioserosa, the Dorsal Closure cannot be completed, making this tissue the most important in the closure [24, 31].

The force exerted by the Amnioserosa is produced by a network of Actin and non-muscular Myosin II present at the center (in a transient manner), and at the periphery of each cell (in a permanent manner) [27]. Indeed, the removal of Myosin II specifically in the Amnioserosa leads to a Dorsal Open phenotype [31]. In addition, Dorsal Closure is thought to display two distinct phases: an early phase (Slow phase), and a later phase (Fast phase). In the Fast phase, the density of Myosin II in amnioserosa cells is dramatically increased compared to the early phase (Figure 1.9). Yet, it is not clear whether this increase in density coincide with the fastening of Dorsal Closure. Anyway, the closure speed is dramatically increased in a second phase. Even though the cells keep on oscillating in this second phase, they show a decrease of their mean area. The apical area of the peripheral Amnioserosa

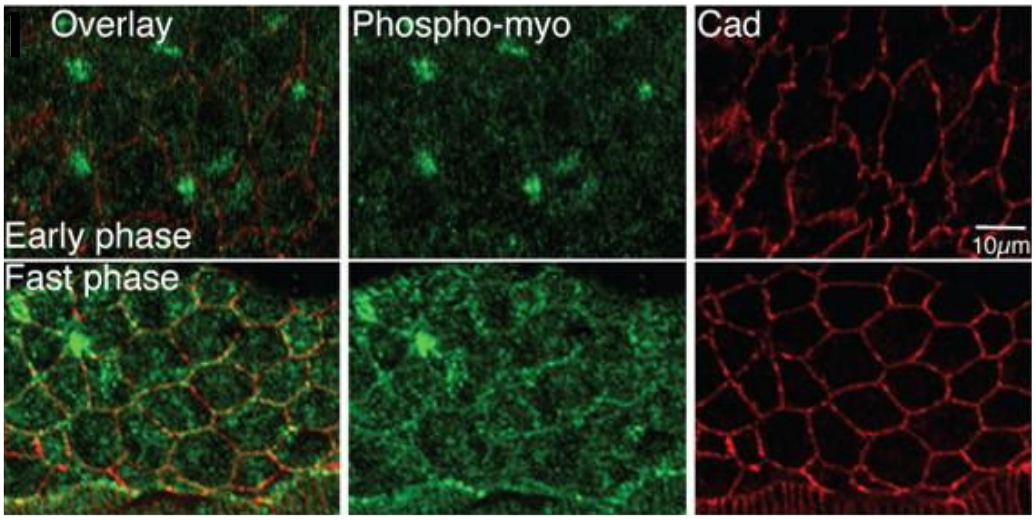


**Figure 1.9:** *Immuno-stained embryos in the early steps of Dorsal Closure (top row), and in the later steps of Closure (bottom row). Myosin II is stained in green, and Cadherin in red. [27]*

cells also shrinks and their oscillations stop, but faster than the rest of the cells [32].
It is also interesting to note that most of the Amnioserosa dynamics is concentrated at the apical side of the cells. Indeed, when cells are cut at their basal extremity, no cell relaxation is observed, while huge relaxations are observed when the apical side is cut [33]. These results suggests that most of the tension responsible for the contribution of Amnioserosa cells to Dorsal Closure originates from their apical extremity.

This polarity, with accumulation of MyosinII in the apical part, is a recurring feature during embryogenesis. It is responsible for instance of the apical constriction, and hence of tissue bending, for instance during mesoderm invagination in *Drosophila* [34]. Periodic variations of Myosin II concentration were also reported during another event of *Drosophila* embryogenesis. Indeed, during Germ Band Elongation, epidermal cells also display Myosin II pulses at the center of their apical area [35]. Interestingly, when these pulses coincidate with a transient increase of Myosin II intensity at the periphery

of the cell, the cell shrinks and stays in this contracted state, while when no peripheral pulse is observed, the cell expands back to its original size. During Dorsal Closure, we did not monitor any peripheral pulse, suggesting that Amnioserosa cells display a behavior of the second type that is when cells are able to regain their original size. Yet, some cells shrink and stop ocillating early in Dorsal Closure (the peripheral Amnioserosa cells) and it would be interesting to assess the putative variations of peripheral Myosin II in these cells in order to determine whether their shrinkage is related to that observed during Germ Band Elongation.

Dorsal Closure is a morphogenetical event driven by forces generated by cells and tissues. This process involves cellular and tissular mechanics. Dorsal Closure is also important for the shaping of the embryo. And, most important, it is a process highly similar to Wound Healing in animals [36, 37], Eyelid formation in mammals [15], or Epiboly formation in Funduli [38]. Dorsal Closure is then a highly interesting system when it comes to study the importance of mechanics in Biology, providing many possibilities to extrapolate results to other species, and in particular to mammals. Therefore, several studies have already aimed at reaching a better understanding of Dorsal Closure mechanics, and at representing the closure's movement by physical and mathematical means.

## 1.3 Presenting previous models of Dorsal Closure

The first work assessing the mathematical representation of Dorsal Closure was performed by Peralta et al. in 2007 [39]. With laser microsurgery, they were able to cut at a subcellular level the Actin Cable, the canthi, and also to perform large cuts in the Amnioserosa. Thanks to this method, they were able to measure initial recoil velocities. Considering that these velocities are proportional to the constraints accumulated previously at this point, they were able to produce ratios of importance of the forces generated the Actin

Cable, the Zipping and the Amnioserosa.
Considering that the two Leading Edges are symmetrical arcs, as shown in Figure 1.10, they wrote the Leading Edge length as $L = 2r\theta$, denoting the canthus to canthus width as $W = 2rsin\theta$, and the half-height at the center of the antero-posterior axis as $h = r(1 - cos\theta)$. From there, they derived two equations:

$$\frac{dW}{dt} = cos\theta\frac{dL}{dt} + (Lcos\theta - W)\frac{d(ln(k))}{dt} \tag{1.1}$$

$$\frac{dh}{dt} = \frac{1}{2}sin\theta\frac{dL}{dt} + (\frac{L}{2}sin\theta - h)\frac{d(ln(k))}{dt} \tag{1.2}$$

Their laser microsurgery experiments showed that the right term of both equations are an order of magnitude below the left ones. Hence, they neglected them. Dividing 1.1 by 1.2, and considering that $k_z \approx -2\frac{dh}{dt}$, they obtained:

$$\frac{dW}{dt} \approx \frac{-k_z}{tan\theta} \tag{1.3}$$

They extracted $v_{closure}$ measuring Amnioserosa's height dynamics in live confocal movies. Considering that $\frac{dh}{dt} = v_{closure}$ and is constant, and that the Leading Edges remain arc-shaped all along the process, they obtain fairly good results representing the dynamics of $W$.

Even though they obtained fairly good results, their model is in the end based on closure speed measurement. Nevertheless, closure speed is in fact the result of the forces involved during Dorsal Closure. Their work is therefore merely a simulation of the evolution of the geometry over time. Even though they are able to predict the geometry dynamics of the Dorsal Hole, this strategy gives no insight about the physical concepts involved in Dorsal Closure, nor on the relative effects of each force generator.

Solon et al., in *Cell*, 2009 [32], used a mechanically more accurate approach, representing Amnioserosa cells as hexagons, with springs on the

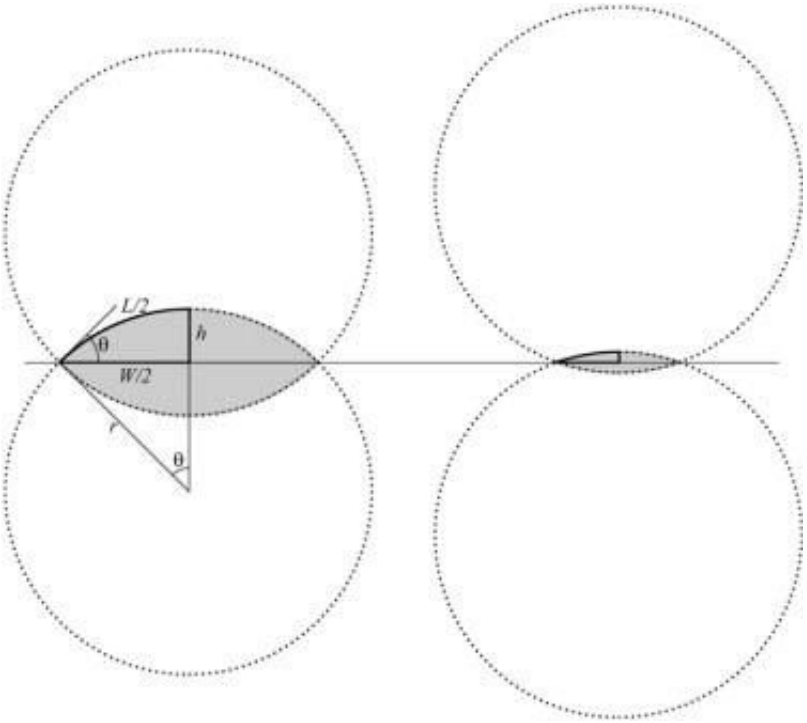


**Figure 1.10:** *The set-up of the model developed in Peralta et al., Biophys. Journal, 2007. The Leading Edges are represented as two symmetrical arcs. The Leading Edges length is* $L = 2r\theta$*, the height at the center of the Amnioserosa, and from the Antero-Posterior axis to the Leading Edge, is* $h = r(1 - cos\theta)$*, and the canthus to canthus length is* $W = 2rsin\theta$*. [39]*

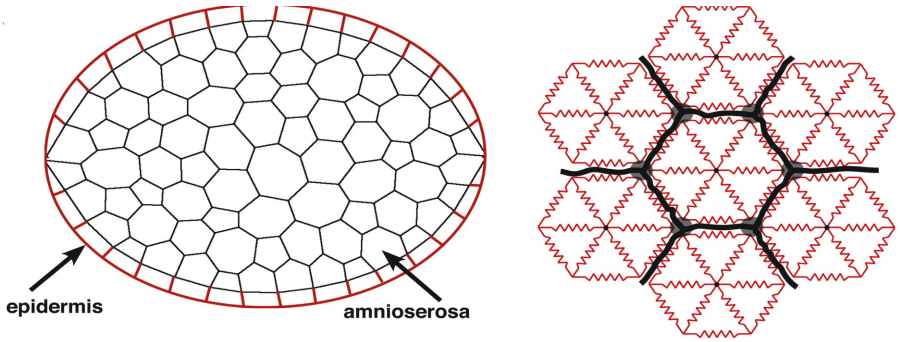


**Figure 1.11:** *Set up of the model developed in Solon et al., Cell, 2009. In the left panel, the network of hexagonal cells. In red is represented the Actin Cable length, that slowly decreases. In the right panel, a representation of the network of springs. [32]*

edges, and also springs connecting the summits to the center of hexagons, as shown in Figure 1.11.

With this model, the Amnioserosa cells oscillations stop after some time, due to a lack of tension in the tissue. The constriction of Amnioserosa resulting from the action of the Zipping and the Actin Cable becomes too important. The ratio between cellular tension and Amnioserosa compression became too much in favor of the latter, preventing cells to oscillate. Interestingly, they argue that the shrinking of the peripheral Amnioserosa cells observed in vivo might restore tension enough to allow central cells to keep on oscillating. Therefore, they introduced a sequential arrest of peripheral cells in the shrinked state, consistently with live observations. As a result, the modelled central cells kept oscillating. These simulations show that the shrinking of the peripheral Amnioserosa cells play an important part in the permanency of Amnioserosa cells oscillations. One can argue that the apoptosis occurring in Dorsal Closure (Toyama), and accounting for 40 to 50% of the closure rate, might serve the same purpose.

Interestingly, their model shows that the oscillation of Amnioserosa cells increases the closure speed. To explain this effect, they formulate the hypothesis that the Actin Cable might act as a Ratchet, preventing cells to go back to their former extended state once they are shrinked. This model

then suggests that the shrinking that is important for cellular oscillation, may come from the ratchet effect.
This model recapitulates rather well the behavior of amnioserosa cells. It is also the first to introduce a mechanical understanding of Amnioserosa cells behavior, and it shows interesting features, such as the need of tension in the Amnioserosa to allow the cells to keep on oscillating, or as the oscillation-dependent fastening of closure. Nevertheless, the effect of zipping is not taken into account. Furthermore, the autonomous essence of the contraction of Amnioserosa cells is not proven, and the ratchet effect, at the base of the interplay between oscillation dependent fastening, peripheral cells shrinking, and Cable induced fastening, remains to be proven.

Another model recapitulates Dorsal Closure, taking into account cells periodic contraction, but without taking into account the zipping. It was developed by Wang et al., in *Biophys. Journal*, 2012 [40]. Also based on the idea that cells contract autonomously, it includes a term in which the contraction is regulated by the amount of myosin in the cells. The amount of myosin itself is regulated by the putative reception of a molecular signal, and molecular degradation:

$$\frac{dm_i}{dt} = k^+ s h_i - k^- m_i \tag{1.4}$$

where $m_i j$ is the amount of myosin in the $j^{th}$ spring of the $i^{th}$ cell. $k^+$ and $k^-$ are the production and degradation rates of the myosin, respectively. $s_i$ is the amount of molecular signal received by the cell, and $h_{ij}$ is a geometric factor handling the repartition of myosin on all the cell's springs. The amount of myosin influences the stiffness of the springs in the cell, causing oscillations. The geometry of the cells and of the tissue is shown on figure 1.12.

This model doesn't take into account the zipping. The canthi were then fixed in space. The Actin Cable is taken into account by adding around the tissue, and attached to the anterior and posterior extremities of the tissue,

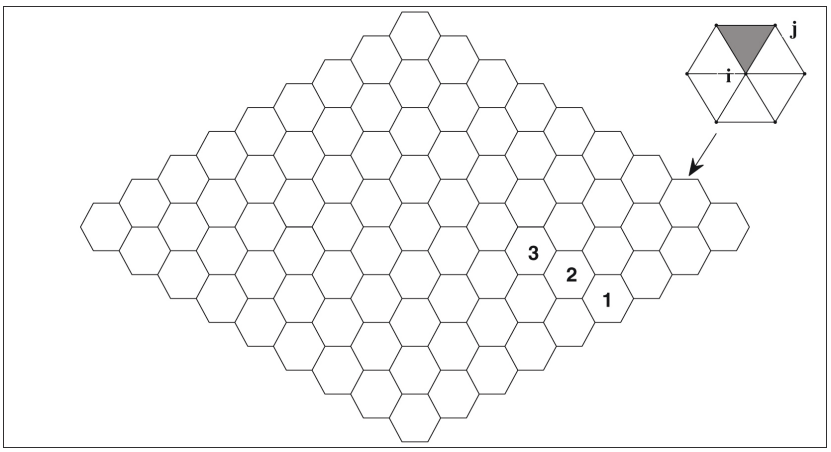


**Figure 1.12:** *The set up of the model developed by Wang et al. The point $i$ represents the center of the $i^{th}$ cell, and the point $j$ the extremity of the $j^{th}$ spring connected to the cell center. [40]*

a spring whose resting length slowly decreases. They include in their simulations a cellular actin cable, surrounding every single cell. They hence built three models: one with only the Cable around the Amnioserosa, one with a Cable only in cells, and one with both the tissular and cellular cable. These models obtained fairly good results, especially recapitulating cellular oscillations, and especially the last one. Moreover, they also decrease the resting length of the radial springs in the cells several times during the process of closure, arguing that the density of contractile molecules (Myosin II) increases during the last phase of closure, based on fluorescence density measurements. Doing so, the global area of Amnioserosa keeps on decreasing. Nevertheless, there is no proof that this increase of fluorescence density is not due to a decrease of cellular area, together with a constant amount of contractile molecules.

Another model was published in 2011 in *Journal of Theoretical Biology* by Almeida et al [41]. While being merely a mathematical model, not recapitulating the tissues physical behavior from a mechanical point of view, it brings an accurate representation of every actor of Dorsal Closure. A Laplace equation $\Delta u = 0$, coming from elastic thin shell theory, was solved

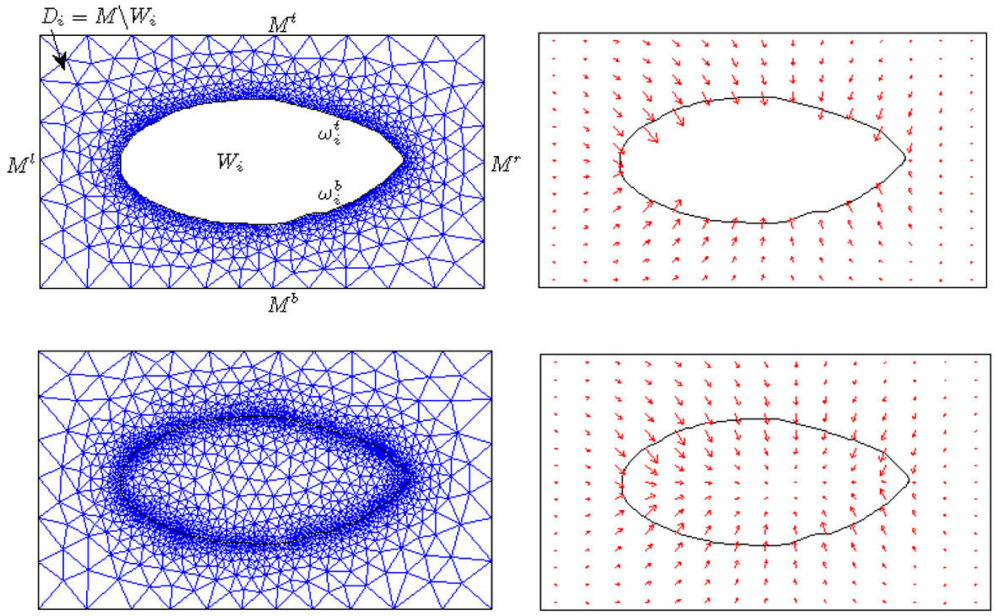


**Figure 1.13:** *Solving domains and meshes (left panels) and examples of velocity fields u, without extension of the model inside amnioserosa (top panels), or with extension (bottom panels). [41]*

on domains presented in figure 1.13, left panel. The forces acting on the closure of the dorsal hole were represented by Neumann boundary conditions, on boundaries presented on Figure 1.13. Neumann conditions are presented in Equation 1.5

$$
\begin{aligned}
u_i &= 0 \; on \; M^l \cup M^r \\
\frac{\partial u_i}{\partial n} &= C_1 n \; on \; M^t \cup M^b \\
\frac{\partial u_i}{\partial n} &= C_2 \kappa n + C_3 n \; on \; \omega_i \backslash Z_i \\
\frac{\partial u_i}{\partial n} &= C_3 n + \begin{pmatrix} 0 \\ -C_4 \end{pmatrix} \; on \; \omega_i^t \cap Z_i \\
\frac{\partial u_i}{\partial n} &= C_3 n + \begin{pmatrix} 0 \\ C_4 \end{pmatrix} \; on \; \omega_i^b \cap Z_i
\end{aligned}
\tag{1.5}
$$

where $n$ is the normal at each interface (its orientation is shown on Fig-

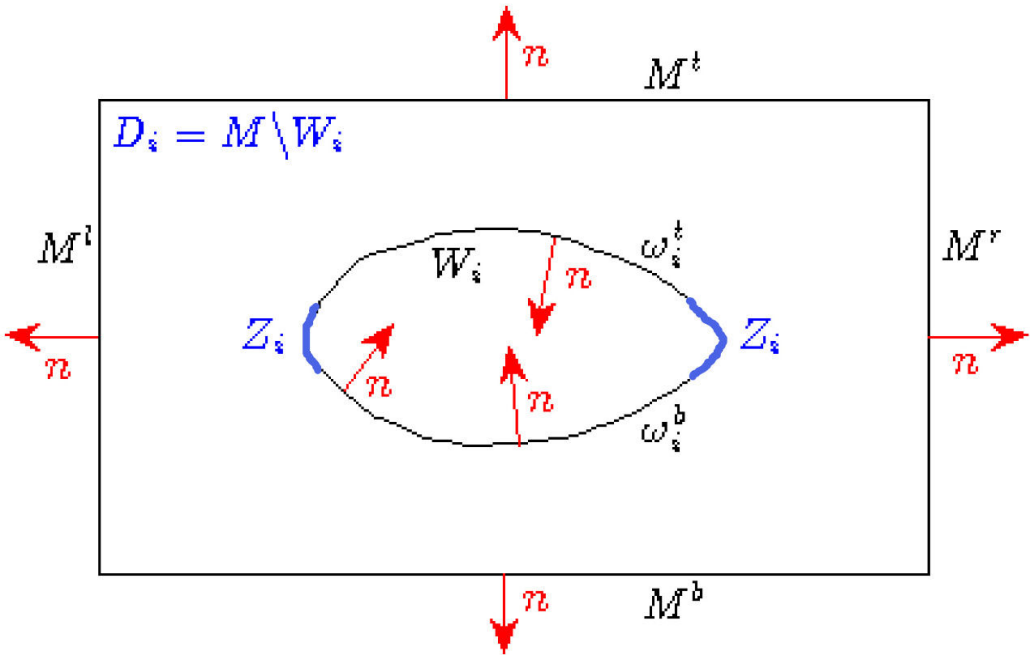


**Figure 1.14:** *Scheme of the normals to each interface, and of the domains on which is applied each boundary condition. [41]*

ure 1.14, together with the domains on which each boundary condition is applied). $C_1$, $C_2$, $C_3$ and $C_4$ are some coefficients representing the opposing force of the dragged epidermis, the Cable tension, the traction of the amnioserosa, and the zipping force, respectively. On $M^t \cup M^b$, $n$, the normal to this boundary, goes outward. Hence, the second equation in 1.5 is resistive. In the third equation, $\kappa$ represents the curvature of the boundary $\omega_i$. The contribution of the Actin Cable is proportional to this curvature. On $\omega_i$, $n$ is inward, thus the contribution of the contribution of the Amnioserosa is constructive. Finally, in $\omega_i \cap Z_i$, the curvature of the Leading Edge is almost null, the contribution of the Actin Cable can then be neglected in this area. On the contrary, the zipping is important in this domain. It is then accounted, considering that its effect is rather in a vertical direction, than in a direction normal to the epidermis-amnioserosa interface. This is why the zipping term is not accounted as a multiplier of the normal to the interface, but as a vector of the form $\begin{pmatrix} x \\ y \end{pmatrix}$.

This model is continuous, it is solved on a mesh covering the whole domain, and uses the same equation in the whole space. Such a model gives good results at a tissue scale: it manages to recapitulate closure both in control embryos, and in spastin mutant embryos (embryos in which the zipping force is absent). Yet, it is not meant to recapitulate cellular behavior.

In conclusion, several works improved our knowledge on how to model Dorsal Closure, each with its strengths and limitations. These limitations leave some particular and interesting features to assess, such as the oscillatory behavior of amnioserosa cells under constraints. Also, other strategies exist to model tissular and cellular behavior. In particular, mass spring networks are often used to model biological tissues.

## 1.4 Understanding the mechanics of biological systems

Dorsal Closure is a widely used system to understand the mechanics of biological systems. But many other interesting works assess the mechanics of biological systems. The mechanics of biological systems is a wide field: understanding molecules, cells and tissues reactions to mechanical stimuli, and their capacity to generate forces, is of a great importance to understand embryo and organs shaping during development, bacterial mobility, tumor packing, cell differentiation... In view of this, many studies gave valuable information on the type of mechanical behavior cells, tissues, molecules or molecular networks experience. In the following paragraphs, we will focus on the works on the reactions of these systems to mechanical stimuli. Altogether, these works give a rather precise framework in which we can accurately perform mechanical modelling in biology.

### 1.4.1 Single molecule experiments

During the early nineties, several laboratories assessed the mechanical properties of single actin filaments. Two methods were used: measuring forces and extension thanks to measurements of the bending of glass needles [42,43], and X-ray diffraction [44,45], measuring the size of an actin monomer inside a muscle filament. Comparing the lengths of the monomers both in the relaxed and contracted state of the muscle fiber, they were able to extract an elastic modulus for single filaments. Both methods found the same value of $E = 2.10^9\ N.m^{-2}$ for the elastic modulus of actin filaments.
Rather simultaneously, other groups studied the buckling of microtubules thanks to optical tweezers [46], or the pushing force generation by microtubules assembly disassembly dynamics [47].
All these works provided many valuable information on the capacity of a cell to react to a constraint, on the molecular origin of these reactions, and the range of parameters values involved. Yet, real biological systems are much more complicated: actin filaments and microtubules are interconnected in complex networks, and therefore may present a much more complex behavior, in particular under shearing constraints.

### 1.4.2 *In Vitro* grown actin networks and cellular properties

Therefore, several groups started to study *In Vitro* the behavior of actin gels and networks. They were thus able to extract a huge amount of information on the mechanics of structures behaving in a very similar way to cells. For instance, it is possible to directly measure the shear and elastic moduli of an actin network, growing this network between the two plates of a rheometer [48].

Other studies allowed to discover that actin networks were also able to

disperse energy after a characteristical time under constraint, which demonstrate a viscous behavior [49, 50]. They also discovered that the amount and type of cross linkers in the actin gel could change that characteristic time [51,52]. Other works also showed that actin networks could either stiffen (when composed of a high density of actin and crosslinkers) or soften (when composed of a low density of these molecules) when under constraint [53–55]. Again, the amount of crosslinkers in the networks modulates the mechanical characteristics of the network, allowing the transition from softening to stiffening, and adjusting the variation of the elastic modulus [56]. Interestingly, it was reported that stiffness could also be modulated through phosphorylation of the regulatory light chain of non-muscle Myosin II, at much faster rates than with crosslinkers [57, 58]. All these results suggest that the cells have at their disposal a great arsenal to adjust their mechanical properties to their environment. These results were confirmed by experiments on single cells, demonstrating that cellular mechanics is mainly due to the cytoskeleton [59–61].

### 1.4.3 Assessing forces present inside a tissue

Knowing the mechanical behavior of cells allows us to understand how cells react to mechanical stimuli. Thus, to fully understand the dynamics of an *In Vivo* tissue, one needs to access the forces applied on the cells inside the tissues.

Numerous studies have used laser micro surgery to assess the forces present at a given time in a tissue [62–64]. Measures of the recoil velocity of the cells surrounding the hole created by the laser, one can estimate the amount of stress that was accumulated in the region prior to ablation. This method is very powerful, but has limitations: it destroys the tissue studied, preventing long term analysis and dynamics studies, and it only allows to compare recoil velocities, to assess the forces patterns within a tissue. This method cannot provide absolute measurements.

Another method is used to measure the absolute force and elastic moduli: the Atomic Force Microscopy. The AFM was genuinely conceived as a microscopy technique, consisting in measuring the flexion of a lever when its extremity is in contact with a surface [65]. A higher flexion of the lever indicates a higher $z$ at the surface of the sample. Yet, forcing the lever to indent the surface, it is possible to extract the surface's mechanical characteristics. This method is used since the early nineties, to assess the mechanics of single molecules, single cells, or tissues, providing a lot of valuable information on live systems [66–69]. Its only limit is the accessibility of the systems it aims at studying, since it needs a direct contact.

Recently, several *In Silico* methods were developed to assess forces patterns in living tissues. Some combined with laser microsurgery [70], others with AFM [71], to assess the mechanics of living systems. Inverse methods (using the biological dynamics as an input, and finding the mechanical characteristics giving the best fit to these data) were also used to extract physical properties [72]. This method, non invasive, allows to study tissues anywhere in the sample. Nevertheless, it often contains approximations (mainly on the dimensionality: 2 or 3D).

In this thesis, we will propose such a method to extract mechanical properties of live Amnioserosa cells, comparing different hypothesis on cellular mechanics, with the objective of giving a better understanding of Amnioserosa cells peculiar behavior.

First, we will introduce the software developed to extract cellular dynamics. Then, the model comparison and validation method will be presented. Finally, a short study of Leading Edge dynamics, based on the software presented in the first section and signal treatment methods, will be reported.

# Chapter 2

# Materials and Methods

*DE-Cadherin::GFP* [73] flies were put in vials capped with an small plate containing a concentration of 1.5% of agar, mixed with a small amount of a source of sugar (blackcurrant syrup). Over the agar, a drop of water and yeast was added. Flies were let at $25°C$ an entire afternoon. In the evening, the agar plate was changed, and the flies let overnight at $25°C$. This method allows to collect the next morning embryos coming from evenings fecondations, the previous ones being laid on the previous agar plate. Dorsal Closure happening between the $10^{th}$ and the $13^{th}$ hour of development, this strategy allows to maximize the amount of embryo collected the next morning at the correct stage.

The chorion (a mineral shell surrounding the embryo) was dissolved by pouring bleach on the agar plate, and letting it act for two to three minutes. Embryos were then filtered from the yeast and rinsed with water in a pill dispenser with a small screen within its cap. Embryos are then collected with tweezers under a binocular, and laid on a coverslip with Halocarbon oil 700, the dorsal side toward the glass, to facilitate imaging. Imaging was performed on a confocal spinning disk microscope Leica-Roper-ERROL, with a 40x magnification oil lens.

A Z-projection of the resulting pictures was then performed with the

software *ImageJ*. A gaussian filtering was then performed with the same software.

The projected pictures were segmented thanks to a software developed during this PhD. This software is presented in the next chapter. This software also allows to extract positional data from the movies. The position of the cells vertices (junctions between three cells) and of the barycenter of each cell was extracted for each frame. Possible point tracking errors were corrected.

Cells were modeled as mass-spring-damper lattices. The corresponding equations were written following a Lagrangian approach, and implemented and solved in $MATLAB^{©}$, thanks to the function *ode*45. The positional information on the surrounding (non-modeled) vertices and cells barycenters was provided as an input to the model, to account for the external constraints.

The solution of the Lagrange equations was provided to a cost function together with the real position of the modeled vertices. The cost function was built following the least squares approach. The cost function was minimized thanks to the function $fmincon$ in $MATLAB^{©}$. The residuals were then tested by calculating their autocorrelation function.

# Chapter 3

# Image treatment and Segmentation

In order to address the cellular mechanics in the Amnioserosa, we need before all to build a tool that allows to easily gather data on cellular movement and area evolution over time. Therefore, we need first to extract the cells position and shape at each frame, from gray-scale images acquired with a confocal microscope. To do so, we built a segmentation and cell tracking algorithm in $MATLAB^{©}$. The strategy we chose is presented in this chapter.

## 3.1 Pre-treatment

Prior to segment the image, and to enhance the efficiency of segmentation, movies from confocal monitoring need to be processed. Even though such treatments are possible with image processing programs like $ImageJ$, we implemented them in $MATLAB^{©}$, for convenience. Indeed, the data collected thanks to the algorithm can later serve as inputs in models implemented in this software. Furthermore, $MATLAB$ offers a more flexible environment than $ImageJ$.

The first step of the image treatment is to perform a lowpass gaussian filtering, to flatten random noise. $MATLAB^{©}$'s $fspecial$ function was used

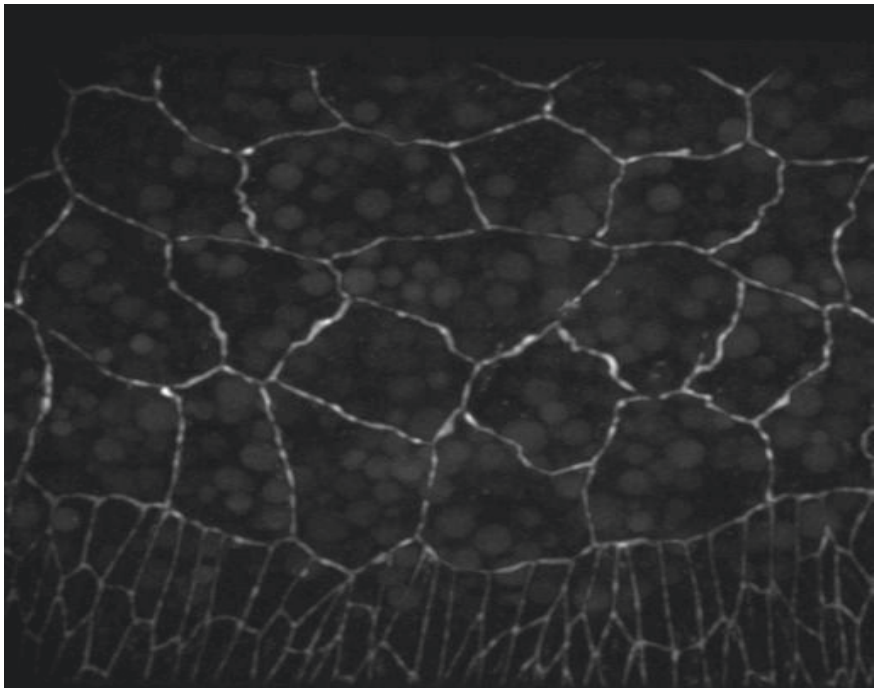

**Figure 3.1:** *Z projection of "raw" confocal images displaying an embryo expressing the fluorescent Cadherin-GFP protein, present at the apical junctions of the cells. The picture has been pre-treated in ImageJ with a Gaussian blur of width 1.*

to generate the 2D gaussian curve. The $filter2$ function was then used to perform filtering. This function basic principle is to pass the bi-dimensional gaussian curve on a subset of points of the picture, and to give to the central pixel a value calculated as the weighted mean of the subset of point surrounding this central pixel. The weights are given by the gaussian value. Hence, one can choose the weights (and therefore the effect filtering has on the picture) by adjusting the mid-height width and the maximum value of the gaussian curve. Adjusting the pixels intensity with this tool enables to flatten the differences between one pixel and its neighbors, and therefore to get rid of random white noise.

White noise is not the only unwanted feature appearing on our pictures.

Unwanted fluorescence is also collected by the confocal microscope. It mainly comes from parts of the embryo we do not wish to monitor, and in particular from the yolk sac, a bag of nutrients lying underneath the Amnioserosa. To improve the quality of our pictures, we wished to remove this background signal. We used for this the *imtophat* function. *imtophat* performs Top-Hat filtering: it subtracts to each picture of the movie its opening.

The opening is a morphological operation on the picture, composed itself by two consecutive operations: erosion and dilatation. To be performed, the opening needs two inputs. One is obviously the original picture. The other one is a structuring element. The structuring element, in our case, is a disk of adjustable size. It is used during the two steps of opening (erosion and dilatation): the pixel values of the picture are compared to those of the structuring element, in a manner depending on the operation performed and that we will present in the following paragraph. To complete the operations, the structuring element is translated all over the picture.

During erosion of binary pictures, at each translation of the structuring element, the pixel at the center is kept non-null only if every pixel inside the structuring element is superior to zero. Hence, small objects (whose size is smaller than the structuring element), are removed from the foreground. Obviously, the outskirts of the structures of importance will be eroded too. Every pixel in a peripheral band one pixel smaller than the structuring element will be removed as well. Thus, a dilatation is performed afterwards. Dilatation follows the same principle, except that each time the structuring element finds a non-null pixel, every pixel inside it will become non-null too. The small structures that were entirely removed will not reappear, but the bigger ones that were simply eroded will regain their original shape, with a good approximation.

For grayscale pictures, the principle is similar: erosion will replace every value of the part of the picture covered by the structuring element by the

lowest of their values, while dilatation will perform the opposite. Combining both of them, the result will be a picture in which the bright objects smaller than the structuring element are absent.

Removing the opening to the original picture, i.e. performing Top-Hat filtering, is often used in image treatment for background subtraction and equalization. From its characteristics, one can easily understand that the structuring element is a key feature for these operations. It removes bright objects smaller than the structuring element from the picture: if the structuring element is wisely chosen, every structure of importance in the picture will be removed. They won't be contained in the opening, and only the background values will remain. Hence, once the opening is subtracted from the original picture, only the important features will remain, and the background will be removed.

Removing the background increases the differences between the local minima and maxima of the picture. The picture has then a better contrast, as shown in Figure 3.2b. Hence, a satisfying contrast is recovered in the regions where it was previously poor, in particular at the edges of the picture, but also on parts of the cell membrane where the signal is low. Thanks to Top-Hat filtering, we were able to compensate the losses of signal due to biological variation or depth effects (some parts of the sample are deeper in the embryo than the others, hence the amount of photons collected is lower) in a satisfactory manner.

The pre-treatment of the picture is now over, the contrast and background intensity having reached satisfactory values. Yet, to reach a full, and proper segmentation, the picture needs to undergo a Watershed transform, and thus several other treatments need to be performed so that the segmentation is as accurate as possible.

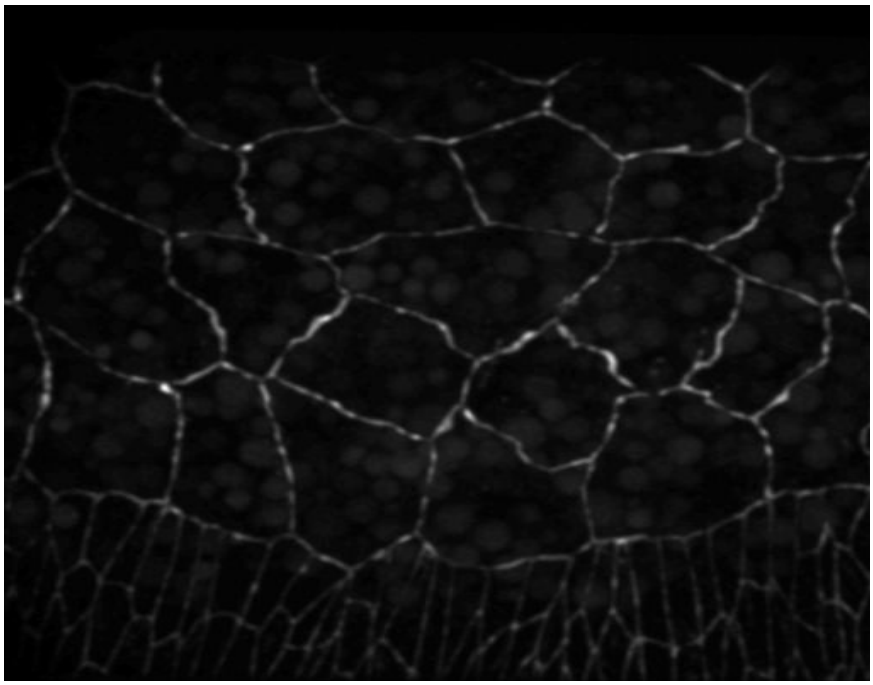

**(a)** *The image after low-pass filtering with a 2-dimensions gaussian filter of width 4 and height 1. The random noise is flattened, and the fluorescence of interest is widened.*

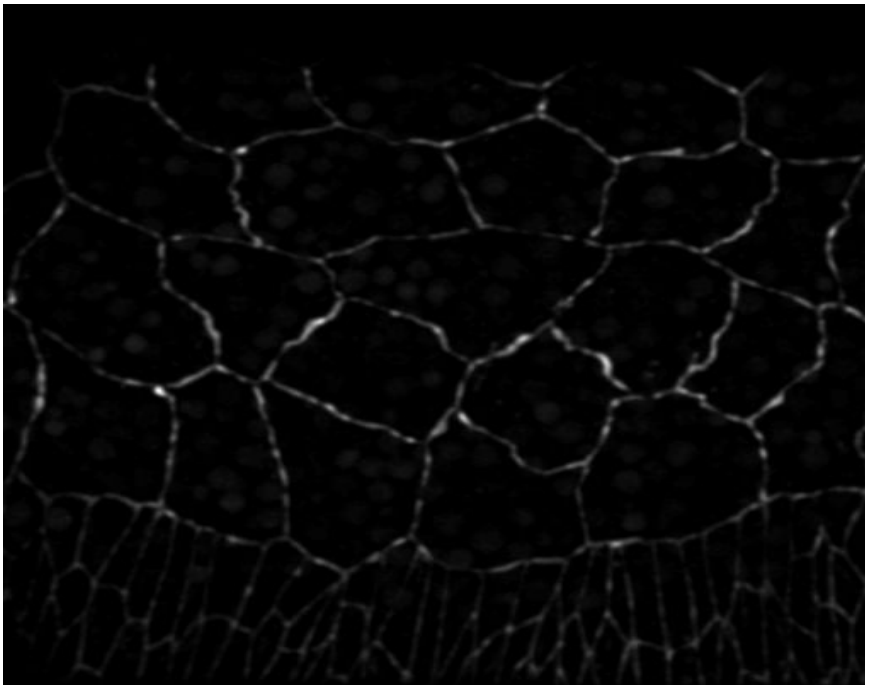

**(b)** *The picture after top hat filtering. The background signal is almost absent, with little effect on the signal of interest. The contrast is hence improved in the regions were it was previously poor.*

**Figure 3.2:** *The same frame, prior to Top-Hat filtering (3.2a) and after (3.2b)*

## 3.2 Segmentation by Watershed

The Watershed transform is a widely used segmentation algorithm. Even though the version of the algorithm used here (*MATLAB*'s *watershed* function) includes a few more refined features, its basic principle is simple: local minima of a greyscale picture are chosen as "water sources", from which the surrounding area is "flooded". Where water coming from two different sources meet, a segment is added. Each region flooded by a source becomes an independent region of the resulting picture.

Even though it is a very powerful tool of image treatment, it is still very sensitive to noise and intensity variation. Pictures hence need to be properly prepared before undergoing such a transformation. In particular, low levels of intensity in the cell wall could lead a region to flood its neighbor. The following treaments applied to the pictures aim at preventing this issue.

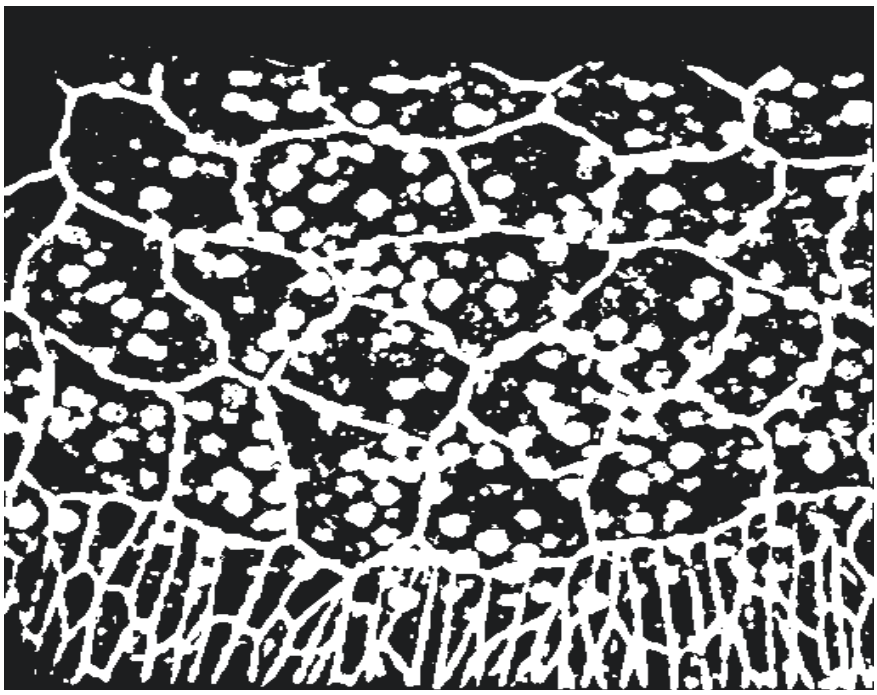

**Figure 3.3:** *The binarized image. The background is now totally removed, at the cost of a huge widening of the signal corresponding to cell walls.*

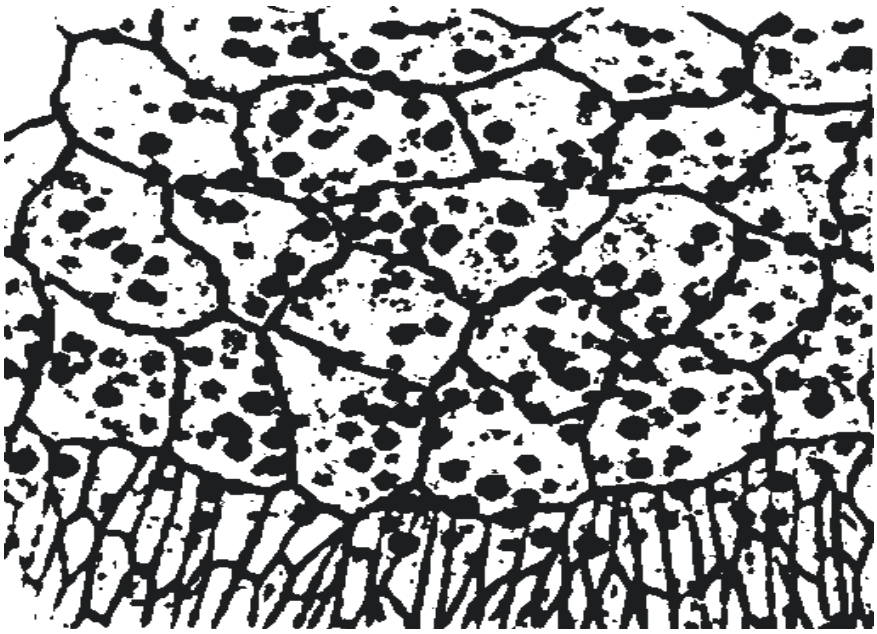

**Figure 3.4:** *The inverted picture. The cell walls are now in black.*

First, the image is binarized. Every pixel which intensity is greater than a certain percentage of the mean value of the picture is set to a value of one, and the rest of the pixels is set to zero. Wisely chosen, the threshold enables to equalize to one all the pixels of the cell membranes. Being necessary, this step yet introduces another issue: pixels from several background regions are given the same value as the cell walls (Figure 3.3). Other treatments are thus needed to correct this problem.

The picture is first inverted: every pixel with a value of one is set to zero, and reciprocally (result shown in Figure 3.4). The cell membranes become black: they are represented by null pixels, and this is important for what follows. Indeed, the last step consists in an Euclidian distance transformation: every null pixel of the picture is given a value corresponding to its Euclidian distance to the non-null pixel. The resulting picture, shown in Figure 3.5, displays equalized cell walls: the crests at the edges of the cells are all at the same levels. This feature has been conserved since the binarization of the picture. It also has clear local minima at the center of the cells. And,

although background signal is still present, its width is much lower than in the binarized picture. Thus, the picture is now ready for Watershed transform.

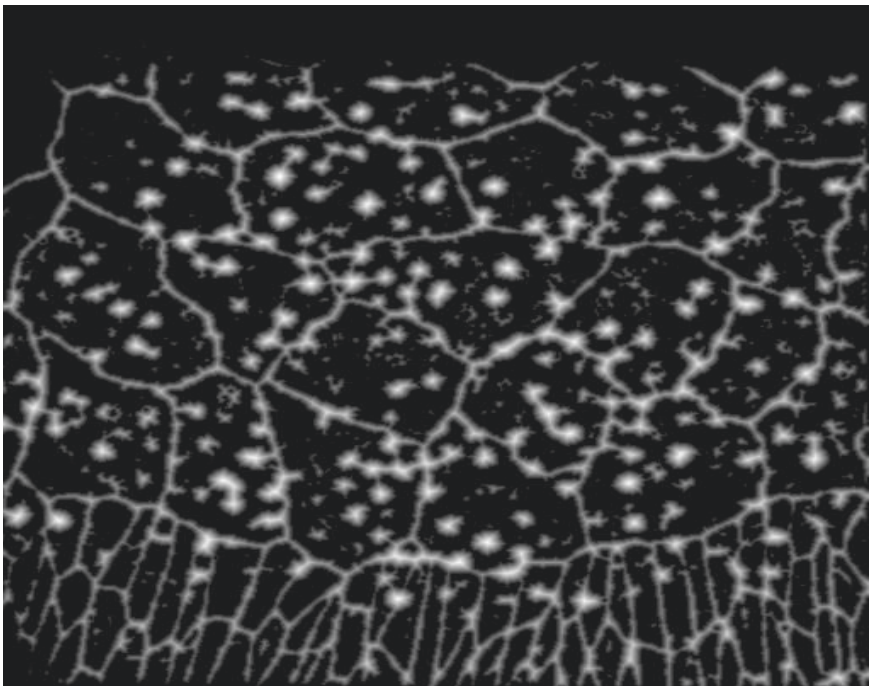

**Figure 3.5:** *The picture after the Euclidian distance transformation.*

The result of the Watershed transform is shown on Figure 3.6. As one can easily see, there are several segmentation defects. These are due to the remaining noise after pre-treatment. To minimize the amount of defects, one has to carefully choose the parameters of every step of the pre-treatment presented earlier. But even then, and even though every step of the protocol presented here have been carefully chosen so that the segmentation would be as efficient as possible, these defects remain, and therefore have to be removed so the final image fits biological data. Actually, a slight oversegmentation of the resulting picture is even required. Indeed, if the parameters were chosen so that no supernumerary segment would be present on the picture after the Watershed transform, a number of segments of interest (in our case, those representing cell junctions), would be absent. Thus, it is prefer-

able to choose the parameters in order to obtain an oversegmented picture.

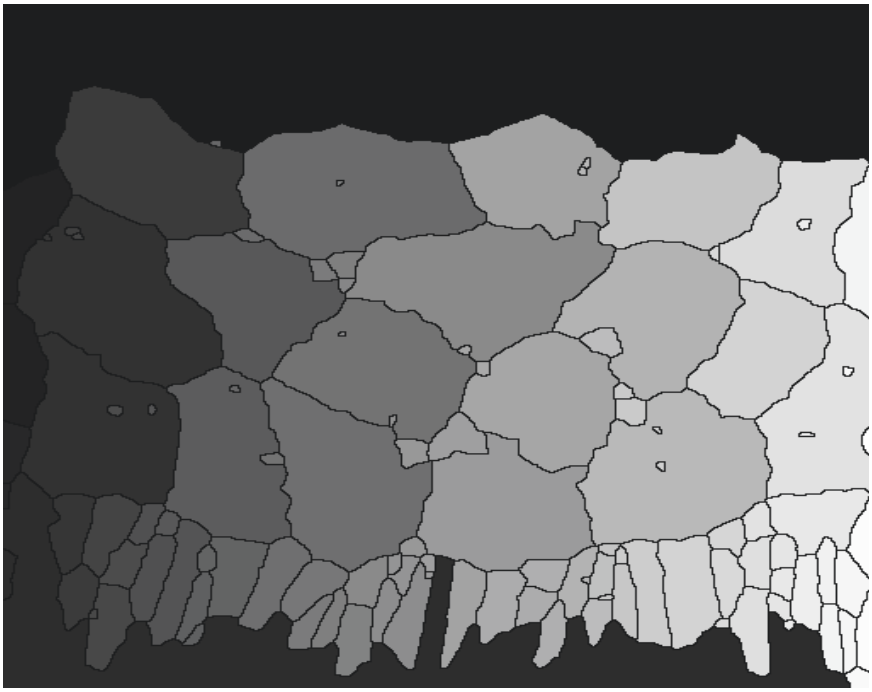

**Figure 3.6**

Nevertheless, removing the unwanted segments can be time-consuming, especially since we are aiming at segmenting movies of several hundreds of frames. Hence, we have been looking for a way to make the whole process as efficient as possible. Also, the segmentation is very sensitive to the parameters chosen during the pre treatment. We were then also looking for a practical way to adjust these parameters. The strategy we chose is presented in the next section.

### 3.2.1 Graphic User Interface and Image post-treatement

For a more convenient running of the program, either for parameters choice and for segmentation correction, we built a Graphic User Interface in *MATLAB*'s *GUIDE*. As shown in Figure 3.7, it includes two main blocks. On the left

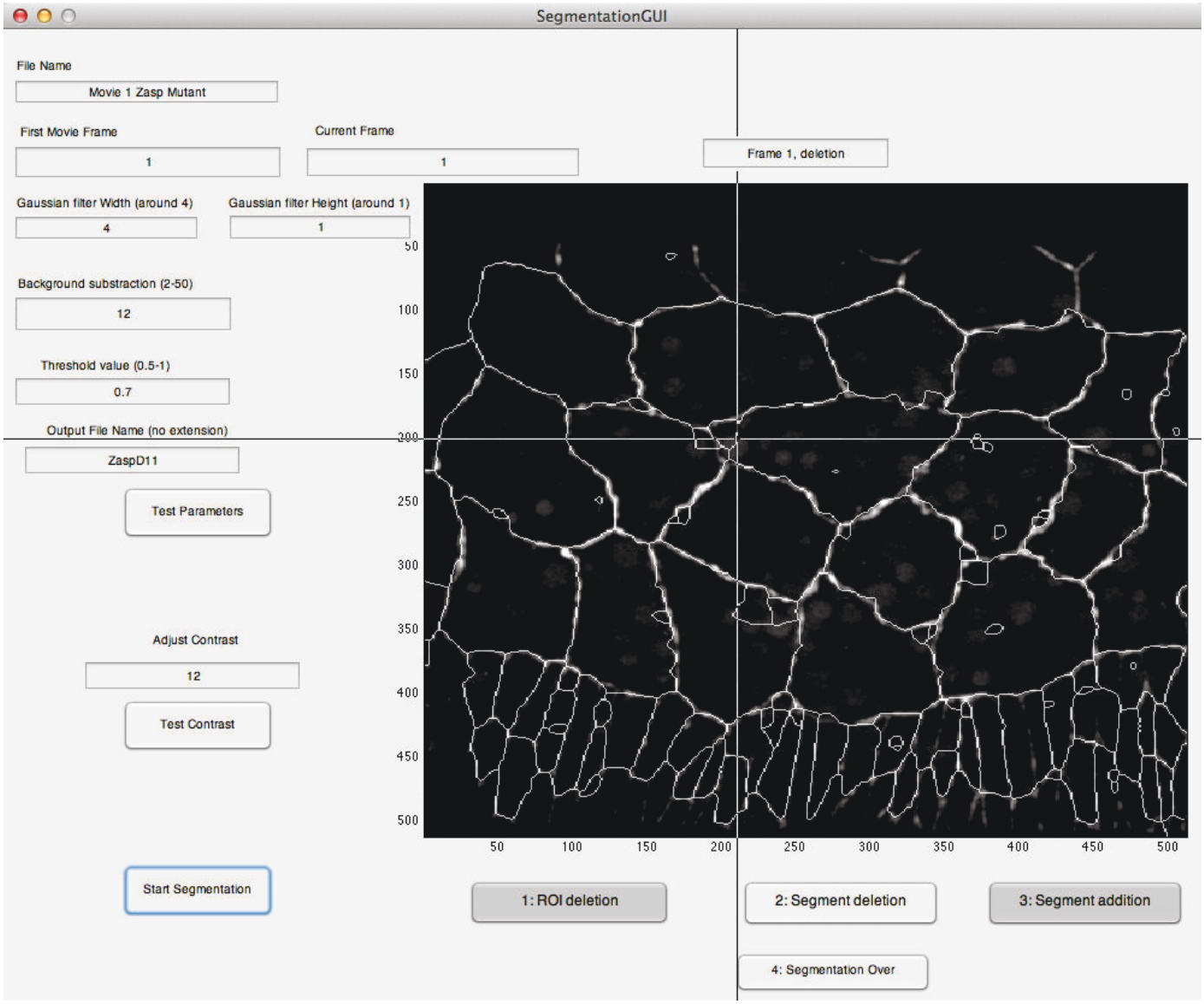


**Figure 3.7**

part, fields in which the user can type parameters values of his choice were inserted. When clicking on "Test Parameters", the segmented picture will appear on the right panel, allowing the user to study the effects of each piece of the pre-treatment (Top-Hat filtering, Gaussian filtering, and thresholding) on the segmented picture. In this part, one can also choose the name of the input file (containing the original movie), and the output file, that will contain every frame and the position of every vertex and cell on each picture.

The user can also choose the frame he will be working on, allowing him to choose the pre-treatment parameters for each frame, avoiding issues coming from frame-to-frame intensity variation. He can also pick up his work where he left off, as every frame is saved when the user decides modifications are finished.

Once the parameters choice is made, the user can easily choose a contrast parameter. Indeed, since the main goal of the GUI is to correct segmentation errors, the user will need to compare the original picture with the one resulting from the watershed. The latter is binary: the pixel value is one for a cell junction, and zero elsewhere, while the former can display a wide range of values. They may be encoded in 8 bits, or 16, having pixel values going either from 0 to 255 or from 0 to 65535. Furthermore, the intensity of the staining depends mainly on the acquisition parameters chosen at the microscope, giving a wide variation of maximum value, or of number of saturated pixels, from a movie to another. Thus, to overcome this difficulty, we introduced a contrast factor, that we will call $f$. The binary picture will be multiplied by $10^f$, and then added to the original picture. The result will be displayed in the right pannel, as shown in Figure 3.7. With the $f$ chosen, it is easy to distinguish both the original and the segmented picture, and which segment corresponds to a cell junction, or does not. It is hence easy to delete inappropriate segments, or to add missing ones, with the help of the second block of the GUI, that we will describe in the next paragraphs.

Being able to remove segments from the picture implies that they were previously individually identified, and labeled. This was done in the following manner. First, every node of the picture is detected, thanks to *MATLAB*'s function *bwmorph*, with the *branchpoint* option. This provides a picture of the same size as the segmented one, but containing only non-null pixels at the positions corresponding to the nodes. Then, this image was dilated. Indeed, the goal of detecting the nodes is to remove them from of the picture, in order to separate segments from each other. In some

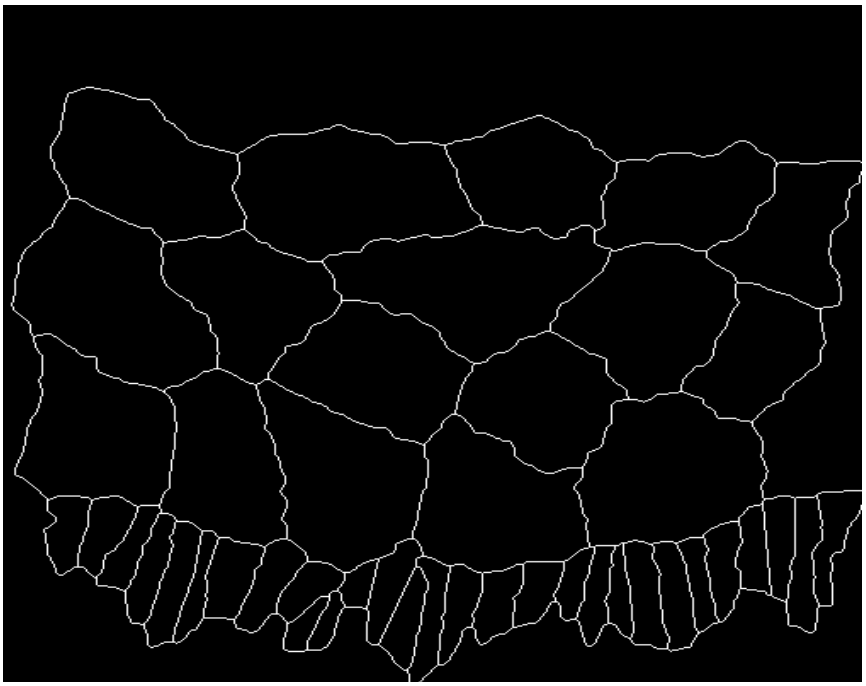

**Figure 3.8**

particular cases of node topology, removing only the nodal pixel wouldn't separate the segments. For instance, when a nodes connects four segments, removing the node pixel would give rise to four other nodes (i.e. points with at least three non-null neighbors).

For instance:

$$\begin{pmatrix} 0 & 0 & 1 & 0 & 0 \\ 0 & 0 & 1 & 0 & 0 \\ 1 & 1 & 1 & 1 & 1 \\ 0 & 0 & 1 & 0 & 0 \\ 0 & 0 & 1 & 0 & 0 \end{pmatrix} \text{ would become } \begin{pmatrix} 0 & 0 & 1 & 0 & 0 \\ 0 & 0 & 1 & 0 & 0 \\ 1 & 1 & 0 & 1 & 1 \\ 0 & 0 & 1 & 0 & 0 \\ 0 & 0 & 1 & 0 & 0 \end{pmatrix},$$

the two matrices representing a subset of pixels in the picture, with the central vertex being a node in the first one, and four new nodes appearing, next to the previous node both in the horizontal and vertical direction, in the second one. To get rid of that issue, the nodes are expanded from a point to a disk of a couple of pixels width. The resulting picture is then subtracted

from the segmented image. Now that every segment is disconnected from the others, it is easy to label each of them independently, using the function *bwlabel*, and to store the position of each pixel included in each different segment in a cell array. Now that the position of each segment is stored, we can move on to the selection of the relevant segments.

To facilitate the selection of the relevant segments, we built a second block containing five buttons. One is a "push button": once the user clicks on "Start segmentation", the program will recollect every parameter chosen earlier, perform the treatment and the watershed, and display the original picture together with the segmented one. The four other buttons are "Toggle buttons" (logical buttons), they return a logical value (0 or 1) depending on whether they are selected or not. Three of them enable the user to choose his course of action for the correction of the segmented picture: "ROI Deletion" allows the user to define a polygonal region on the picture, by clicking on the image on points that wil become the summits of the polygon. Then, every segment having at least one pixel included in the polygon will be found in the data previously stored, and removed. This feature comes particularly handy when the contrast of the picture is poor, and the oversegmentation important. It allows the user to delete vast regions of unwanted segments, within, or around, cells. Yet, since segments are defined after an expansion of the nodes, 'spur' pixels are still present in both nodes region after the deletion. They weren't taken into account in the segment, since they were close enough to the node to be covered by the expanded disk, and were then removed from the picture with the node. Therefore, they were not taken into account in the segment. Hence, the image suffers an erosion after the segment deletion, to remove these remaining pixels.

Having the second button 'On' allows the user to delete individual segments. When clicking on the picture, the program calculates the distance between every pixel contained in a segment and the point chosen by the user by clicking, detects the closest one, and removes the entire segment to which

the point belongs. Again, the picture suffers an erosion to remove the spur pixels. This option enables the user to precisely remove individual segments.

The last option allows the user to add a segment to the picture. The user needs to click on two points of the picture between which he considers a segment should be present. The program then considers several options. If one of the chosen points is close enough to a point contained in a previously existing segment, the new one will be connected to this point. If one of the clicks is at a position close to the image edges, the new segment will be connected to the nearest point of the edge. If neither of these cases is true, the new segment will have an end at the exact point that was chosen by the user. Every combination of the three possibilities is available (segment to segment, segment to edge, edge to segment, clicked point to edge...). Once the two points are chosen, a straight line is added to the picture between them. The picture is then skeletonized, to ensure that the pixels of the added straight line will have only two non-null neighbors, and therefore will not be accounted as a node. This last feature is very convenient for instance when a cell is slightly out of focus for a few frames, and therefore when recovering its boundaries would be at an extreme oversegmentational cost. A huge oversegmentation causing segmental noise (i.e. the accuracy of the positioning of the segments and of the nodes dramatically decreases), this feature enables the user to recover the data of this cell, without impairing the data of the rest of them. Carefully choosing the points at which the new segment will appear, by comparison with the raw picture, makes the error induced by this technique negligible.

Once the user considers that the correction is over, he can click on the last button, "Segmentation Over". The program will then display the final corrected picture, an example of which is presented in Figure 3.8. The new segmented frame is then saved in the file chosen by the user earlier, together with the position of each vertex and cell in the picture. Once the movie is entirely segmented, we can reorder all these data, to finally extract every

cells and vertices dynamics.

### 3.2.2 Data sorting

We have now obtained the position and shape of the cells monitored by confocal microscopy, for every frame. We also obtained the position of each vertex monitored in every frame. We need now to reorder the data, to be able to track individual cells and vertices over time, and therefore obtain their dynamics.

To do so, we simply detect the closest vertex (or cell) in the next frame. For a vertex present in a frame at time $t$, and numbered $n$, its distance to every vertex present in the next picture (time $t+1$) will be calculated. The vertex of the next picture showing the lowest distance is selected, and its position is assigned to the vertex $n$, at time $t+1$. This operation is performed for every vertex present at time $t$.

For cells, the position of their barycenter is first calculated, as the mean of the position of every pixel contained in its limits. It is the barycenter position that is compared from one time point to another, to address the right label to each cell.

The cells and vertices labels are those they were given by the cell labeling and node detection for the first frame.

Thanks to this set of algorithms, we are able to extract a great amount of data from confocal microscopy. We can explore cell connection dynamics, cell area periodicity, point dynamics at the edge between two tissues... A few examples of these data are presented in Figure 3.9. These data will serve as an input to the models presented in the next section. They will also serve to assess the validity of the models.

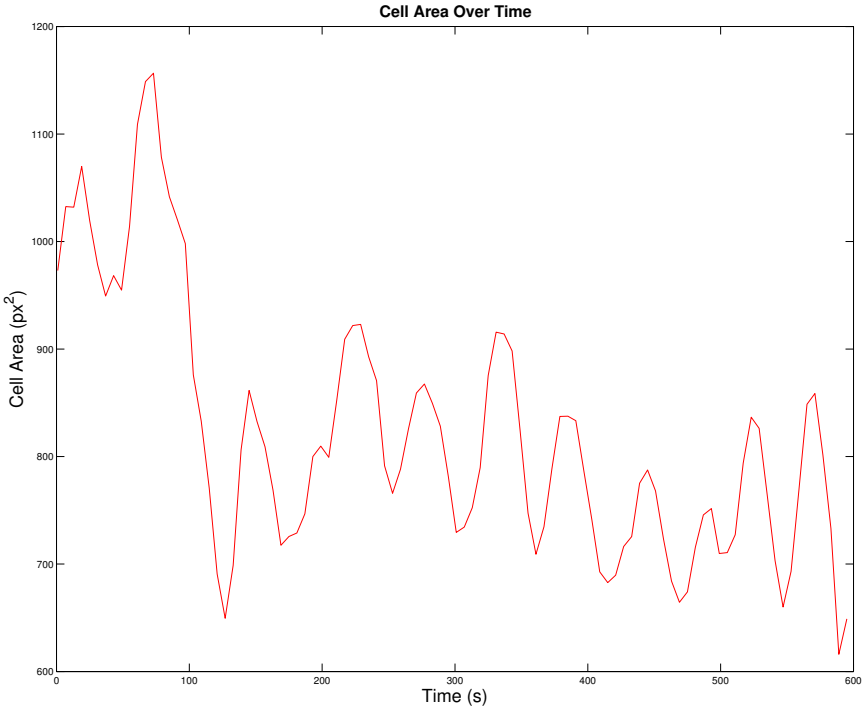


**(a)** *Amnioserosa Cell Area over Time*

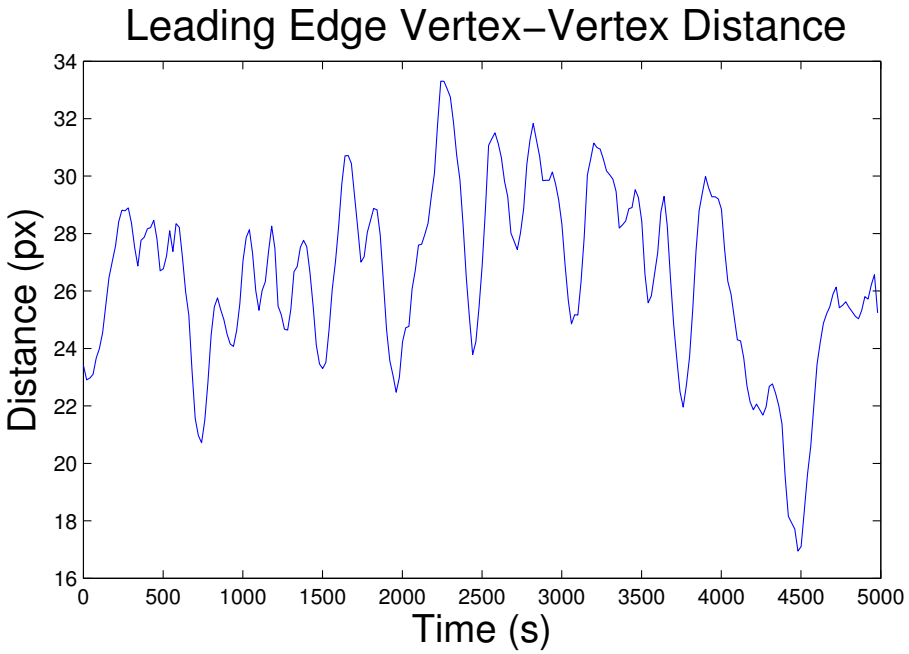


**(b)** *Dynamics of the distance between two adjacent vertices at the edge between the Amnioserosa and the Epidermis.*

**Figure 3.9:** *Examples of data extracted through segmentation, labelling and tracking.*

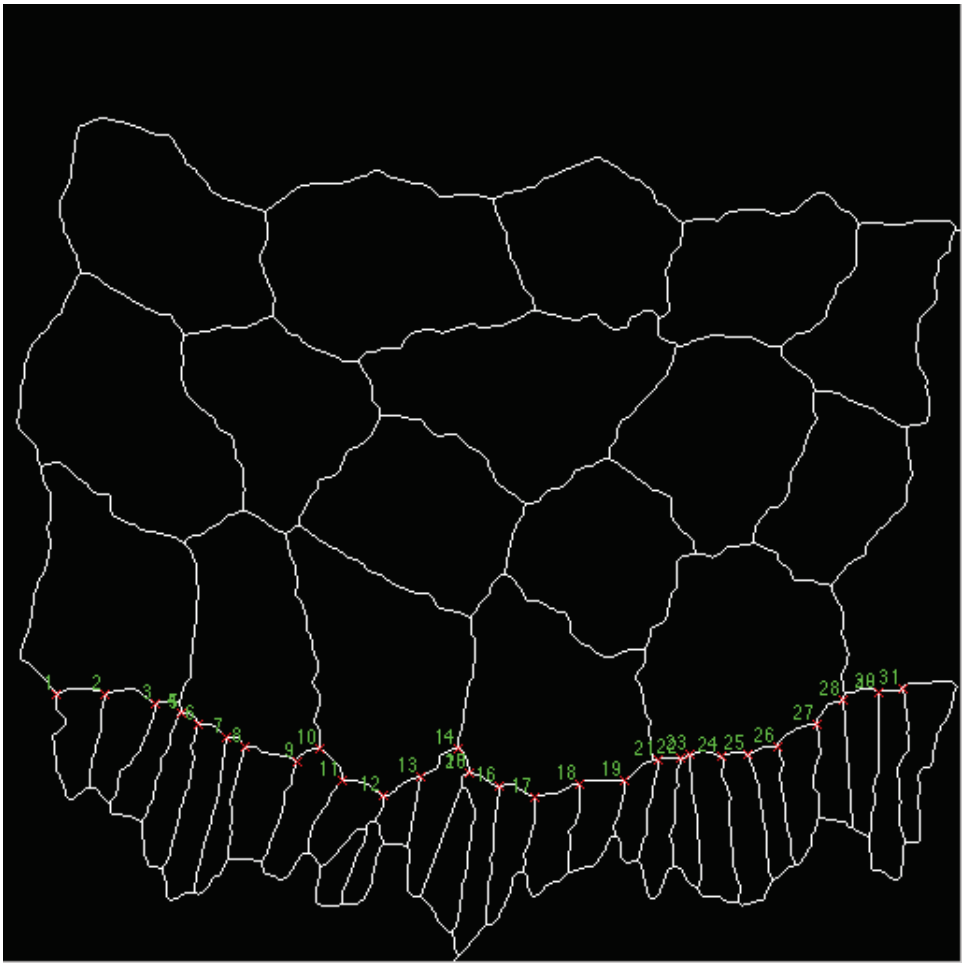


**Figure 3.10:** *Frame of a segmented movie, displaying the position of the nodes present at the edge between the two tissues*

# Chapter 4

# Amnioserosa cells oscillation models

Dorsal Closure is a system that has been widely studied over the years, for its similarity with wound healing, the number of major signaling pathways involved, and the insight of cellular and tissular mechanics it provides.
The role of Amnioserosa cells in Dorsal Closure, and the mechanics of these cells, have been the object of various studies as well, in particular how their apical area oscillations influence closure. Yet, no consensus arose from these studies to explain the action of Amnioserosa cells.
Furthermore, the mechanics of cellular systems have been proven to be an important feature of the generation of shape and patterns during development. Nevertheless, exploring mechanical characteristics of living systems remains very difficult. Hence, many studies have focused on representing *In Silico* cellular behavior, to assess molecular, cellular and tissular mechanics.
To improve our understanding of Amnioserosa cells mechanics, we built several dynamical models of Amnioserosa cells movements. Solving the equations of motions, we compared the results obtained to the positional data extracted thanks to the segmentation. The comparison was performed using the least squares approach.
In this chapter, we consider the vertices (junctions between three cells) to be focal points for forces. Hence, we built models on lattices whose nodes

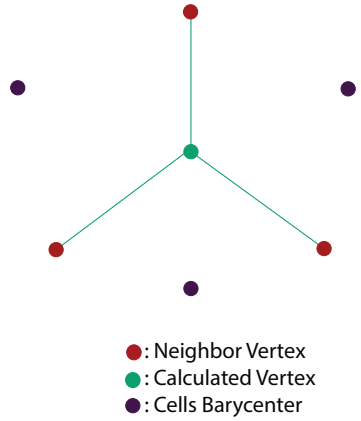


**Figure 4.1:** *Oscillatory Model Set Up. The distance from the central vertex (light green) to the fixed vertices (red, position provided by biological data) is approximated by the equation (4.1).*

positions are the vertices. Since the amnioserosa cells are also capable to contract and expand radially in a periodic manner, we also included the cells barycenters in the lattice.

## 4.1 Oscillatory Model

Amnioserosa cells are known to show a periodic oscillation of their apical area [27]. These oscillations are due to the periodic variation of the concentration of non-muscular myosin II at the center of the apical part of the cell. Myosin II is a molecular motor, binding to actin fibers and generating a contractile force. Hence, a natural way to represent Amnioserosa cells movements is to consider them a set of autonomous oscillators interacting with each other.

### 4.1.1 Equations

We set up an oscillatory model using a simple cosine function (4.1) to make the distance between the vertices and the neighboring cells barycenters vary, as shown in Equation 4.1:

$$d_i = \vec{A}_i \cos(\omega_i t + \phi_i) \tag{4.1}$$

Where $d_i$ is the vertex-vertex distance, $\vec{A}_i$ the amplitude, given as a percentage of the mean of the vertex-vertex distance extracted from the movie, times the unity vector of this distance at each time $\vec{e}(t)$. $\omega_i$ and $\phi_i$ are respectively the pulsation and phase associated to the cell $i$.

### 4.1.2 Optimization

Following the least squares approach, we built the following objective cost function to be minimized:

$$J = \sum_{t=1}^{T_{max}} \|y_q(t) - q(t)\|^2 ,$$

where $T_{max}$ is the last movie frame, $y_q(t)$ the real position of the vertex at each time $t$, and $q(t)$ the position provided by the model. The minimization of this cost function aims at finding the best fitting parameters (here, $\omega_i$ and $\phi_i$).

### 4.1.3 Results

This strategy unfortunately fails at representing the vertices movements, as shown in Figure 4.2. This result suggests that to represent Amnioserosa cells dynamics, other contributions have to be taken into account, such as cells capacity to store and disperse energy. Hence, in the following, we studied the importance of various possible mechanical contributions.

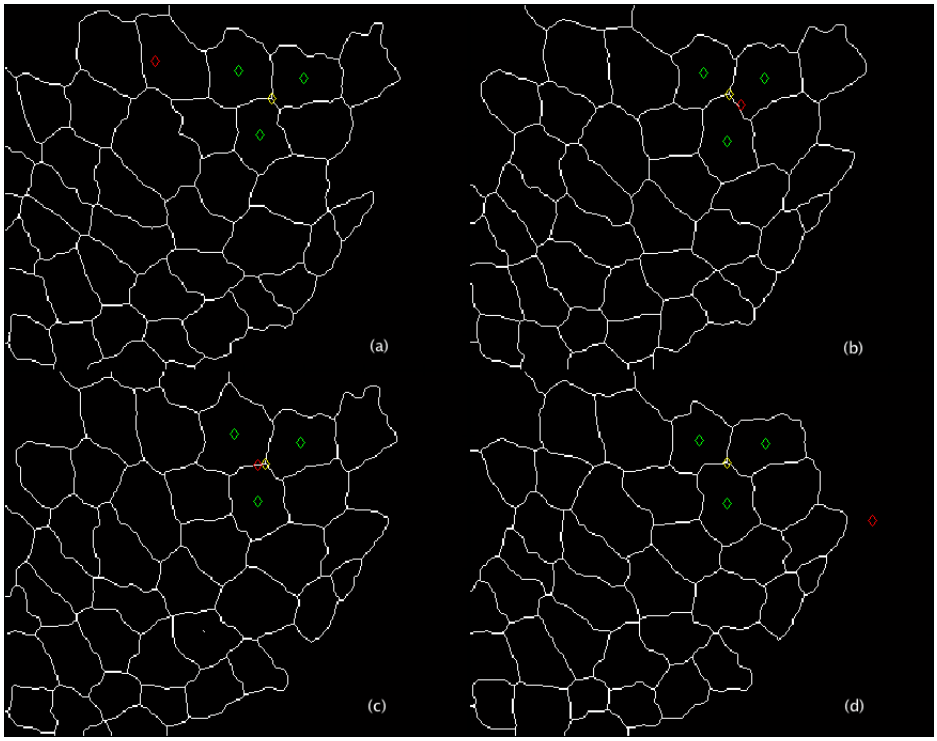


**Figure 4.2:** *Oscillatory Model results. In green, the cells' barycenter, extracted from segmentation and provided to the model. In yellow, the position over time of the real vertex, and in red, the calculated vertex. In (a), $t = 0$, $t = 18s$ in (b), $36s$ in (c) and $60s$ in (d).*

## 4.2 Mechanical Model

### 4.2.1 Cellular Mechanics

Cellular mechanics has been widely studied over the years. It has been shown that cells have the capacity to store energy ; they may have an elastic behavior. They are also able to disperse energy, for instance by reorganizing their cytoskeleton ; they are viscous. And, last but not least, they may have an active reaction to mechanical stimuli, either by increasing their stiffness (stress-stiffening), or by decreasing it (stress-softening).
Dynamical models were hence built and optimized with the least squares technique, taking into account cells possible behavior. The strategy followed is detailed in the next sections.

### 4.2.2 Elastic Model

We first implemented a linear elastic model. Indeed, depending on the characteristics of the Acto-Myosin network present in the cells, the characteristic time of transition between an elastic behavior and a viscous behavior might be bigger than the period of the solicitations due to the neighbor cells expansion and contraction period.
The modelled node connects the central vertex of Figure 4.1 to its neighbor vertices with springs, and ignores any contribution coming from the center of the cells. We obtain the system of equations depicted in equation 4.2. The extremity of the springs corresponding to the neighbor vertices are given the position of these vertices at each time $t$. The other end of the springs is attached to a point mass $m$. The resting lengths $l_{0,ij}$ between the vertex $i$ and its neighbors $j = 1, 2, 3$ are calculated as the mean distance between the couple of vertices $i, j$, extracted from the movie. $y_i$ and $y_j$ are the positions of the calculated vertex and its neighbors, respectively.

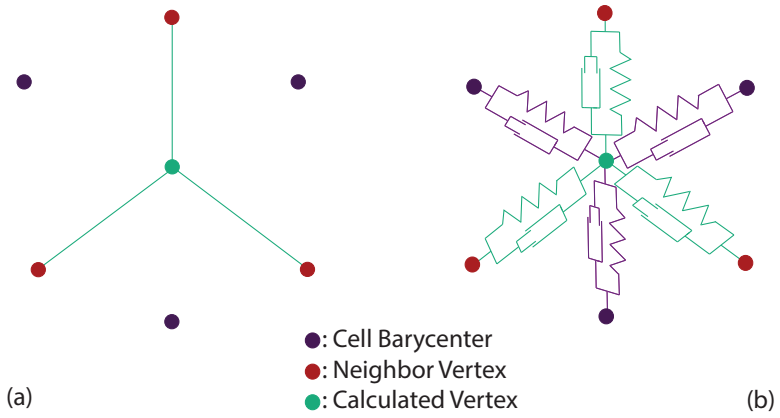


**Figure 4.3:** *Minimal Mechanical Model. (a) The schematized cellular junctions. The position of the cells barycenter (purple dots) and the neighbor vertices (red dots) are provided to the model. The position of the central (light green) vertex satisfies the equation (4.2) in case of a pure elastic behavior, and (4.3) in case of a visco elastic behavior. (b) Schematization of the equations. Different viscous and/or elastic parameters are used, depending on whether the vertex is linked to a vertex (through a membrane, light green spring and dashpot) or to a barycenter (through a cell, purple spring and dashpot).*

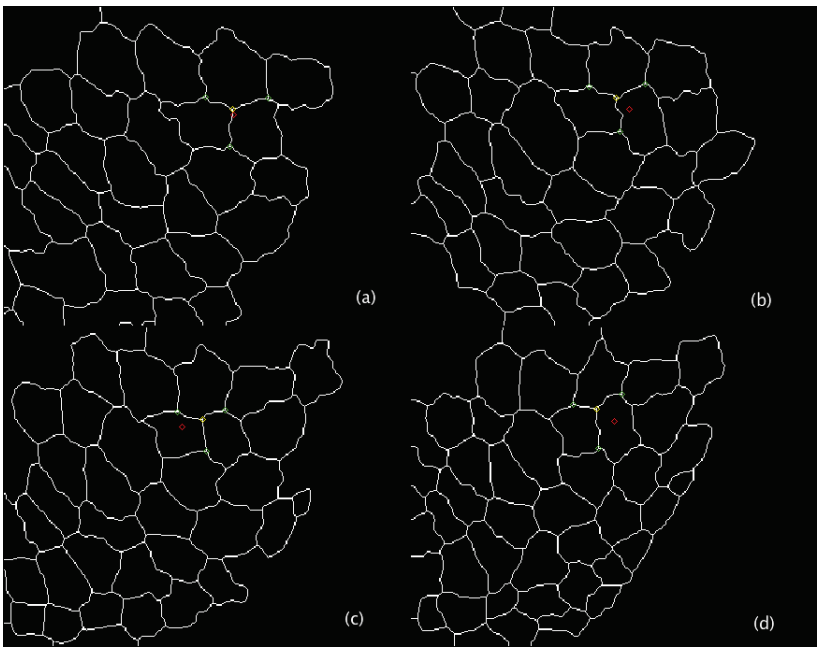


**Figure 4.4:** *Elastic Model results. In green, the neighbor vertices, extracted from segmentation and provided to the model. In yellow, the position over time of the real vertex, and in red, the calculated vertex. In (a), $t = 60$, $t = 210s$ in (b), $360s$ in (c) and $510s$ in (d).*

$$\ddot{\vec{y_i}} = -\frac{K_{vertex}}{m} \sum_{j=1}^{n_{vertex}} (\vec{y_i} - \vec{y_j} - \vec{l_{0,ij}}) \tag{4.2}$$

The parameters to optimize in this model are $K_{vertex}$ and $m$. The cost function is the same as in the previous section. We manage to obtain a calculated point moving around the real vertex, as shown in Figure 4.4. Even though this strategy gives better results than the previous one, the average distance between the model and the biological data is still unsatisfying, i.e., the cost function value is too high.

Adding the radial component decreased the functional value, but even then, the model failed to recapitulate properly the point dynamics. Movements are too wide, and unrelated to the real points dynamics. We hence

moved toward a model taking into account viscosity.

### 4.2.3 Visco-Elastic Model

In this new version of the model, we added a viscous term between vertices, and between the barycenters and the calculated vertex. An elastic term between the cells barycenter and the central vertex was also added, as shown in equation 4.3. Two different sets of viscous and elastic parameters were optimized, one for the vertex-vertex connections, and another for barycenter-vertex connections. Hence, the parameters to optimize are $K_{vertex}$, $K_{bary}$ (the elastic modulus of the connectivity between barycenters and vertices), $\mu_{vertex}$, the damping coefficient for a vertex vertex link, $\mu_{bary}$, the damping coefficient for a vertex barycenter connectivity, and $m$, the points mass. The setup is represented in figure 4.3.

Using such a strategy, we are close to what we think are the real mechanical characteristics of the cells, given that elasticity alone cannot recapitulate properly the vertex movement. We take into account both elasticity and viscosity, and we also take into account in a different manner the radial and peripheral contributions of the cells, which were shown to be different.

$$\begin{aligned} \ddot{\vec{y_i}} = &- \sum_{j=1}^{n_{vertex}} (K_{vertex}.(\vec{y_i} - \vec{y_j} - \vec{l_{0,ij}}) - \mu_{vertex}.(\dot{\vec{y_i}} - \dot{\vec{y_j}})) \\ &- \sum_{k=1}^{n_{bary}} (K_{bary}.(\vec{y_i} - \vec{y_k} - \vec{l_{0,ik}}) - \mu_{bary}.(\dot{\vec{y_i}} - \dot{\vec{y_k}})) \end{aligned} \tag{4.3}$$

As expected, the results are rather satisfying. The vertex position found after optimization remains quite close to the real one. Indeed, the objective cost function value is much smaller than in the previous case.
Nevertheless, even though this model seems satisfying, it does not include any term taking into account myosin II quantity variation. Therefore, we

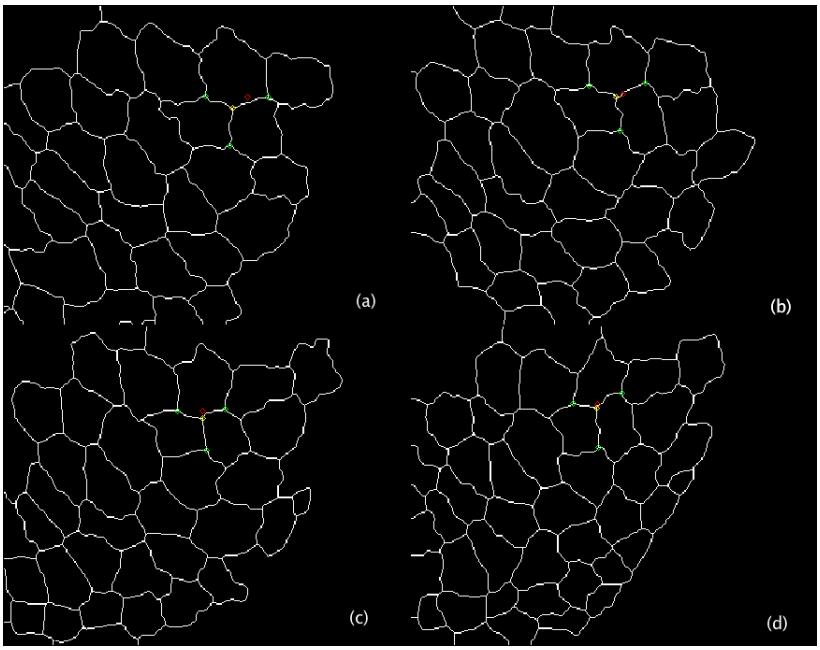


**Figure 4.5:** *Visco-Elastic Model results. In green, the neighbor vertices, extracted from segmentation and provided to the model. In yellow, the position over time of the real vertex, and in red, the calculated vertex. In (a), $t = 60$, $t = 210s$ in (b), $360s$ in (c) and $510s$ in (d).*

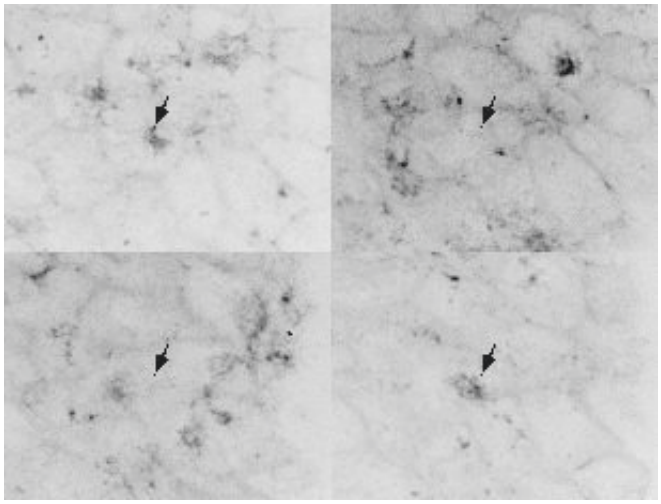

**Figure 4.6:** *Still images of an embryo expressing the fusion of GFP with Spaghetti-squash (i.e. the regulatory light chain of myosin II). One can observe the periodic appearance of patches of myosin II at the center of the cells.*

decided to add a new term to the model. Given the capacity of the cells to change their mechanical properties when under constraints, we decided to add a term of nonlinear elasticity, where the elastic modulus would be equal to a constant term, plus a term depending on the elongation.

### 4.2.4 Non Linear Elastic component

As discussed earlier, cells have the capacity to adapt their stiffness, depending on the amount of strain they undergo. This behavior relies on the adaptation of their concentration in cytoskeletal cross linkers, in molecular motors, or of the efficiency of these motors thanks to phosphorylation. Phosphorylation was recently proven to have an influence on Dorsal Closure [74]. There is a possibility that the variation in Myosin II concentration in Amnioserosa cells comes as a result of the constraints theses cells underwent. To explore this possibility, we introduce a non-linear elasticity term between the calculated vertex and the barycenters. And to represent the fact that

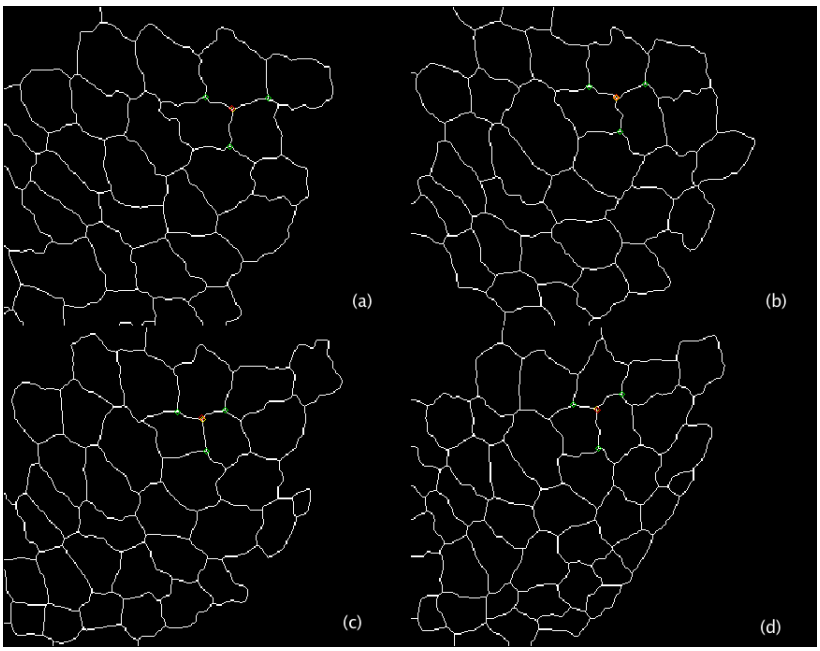


**Figure 4.7:** *Non Linear Visco Elastic Model results. In green, the neighbor vertices, extracted from segmentation and provided to the model. In yellow, the position over time of the real vertex, and in red, the calculated vertex. In (a), $t = 60$, $t = 210s$ in (b), $360s$ in (c) and $510s$ in (d).*

acto-myosin complexes have a strong pulling capacity, but hardly oppose to compression, we made this contribution come to zero when the barycenter-vertex distance felt under the resting length (i.e., when $\vec{y_i} - \vec{y_j} < \vec{l_{0,ij}}$).

Adding this characteristic decreased even more the functional value. The calculated point remains very close to the real one, and the dynamics look coherent with the data extracted from the movie. This result suggests that Amnioserosa cells mechanics is driven by their viscous and elastic characteristics, together with their capacity to modify these characteristics when under constraints. Yet, these results remain to be confirmed by expanding the model from the sub cellular level to the cellular scale.

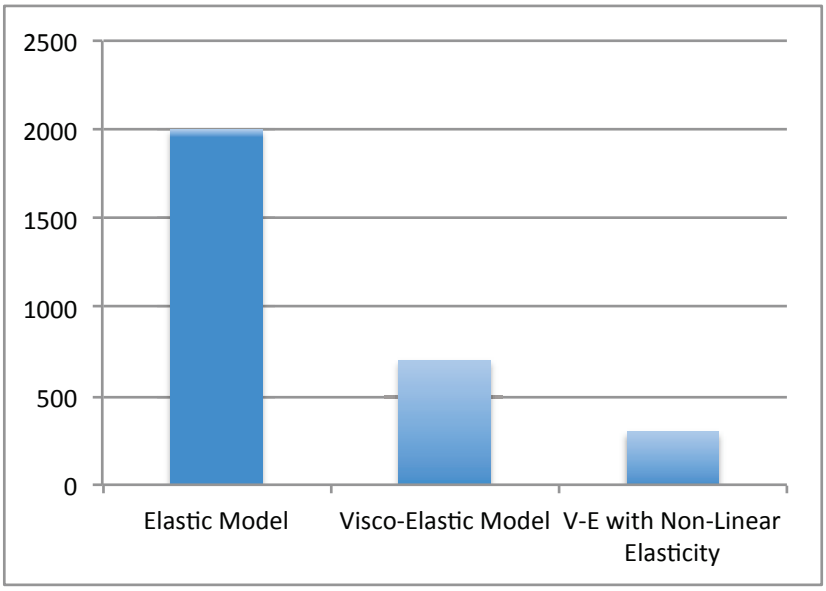


**Figure 4.8:** *Bar graph of the cost function values for the different types of mechanical models applied to one point.*

## 4.3 Generalization of the Mechanical model

Now that we have proven the validity of our approach on a very simple system, calculating the dynamics of one point alone, we built more general models. We still want to assess which set of characteristics represents best the biological data. Therefore, we are still testing the cases discussed in the previous section. We built models capable of taking into account $n$ cells with $n_v$ vertices.

### 4.3.1 The Lagrangians

Similarly to the models presented in the previous sections, vertices are represented by point masses of Cartesian 2D coordinates (with respect to a fixed frame). Their position is denoted by $q_i(t) \in \Re^2$ at time $t \geq 0$ for $i = 1, 2, \ldots, n_v$. We assume that the mass of each of such points is $m$ (considered equal for each point) and, for the sake of brevity, let $q_i(t)^2 := \|q_i(t)\|^2$. Thus, the velocity of the mass point $i$ at time $t$ is denoted by $\dot{q}_i(t) \in \Re^2$ and

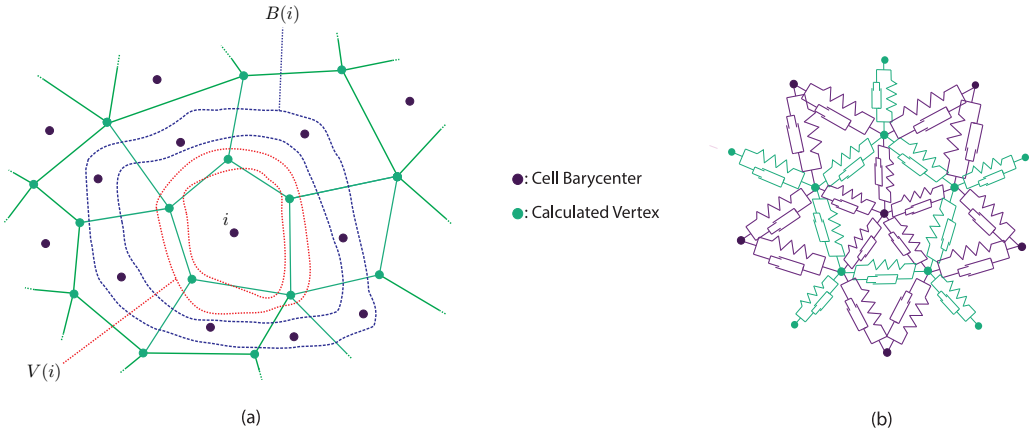


**Figure 4.9:** *Mechanical Model Set Up.(a) A scheme of a system of cells. The segments in light green represent the apical junctions of the cell, and part of its neighbor's. The light green dots represent the vertices. The purple dots depict the neighbor cell's barycenter. (b) The model joins these same points with two distinct spring-damper systems: one joining the vertices together (along the apical junctions, light green), the other joining the vertices with the cells barycenter (across the cells, purple)*

similarly let $\dot{q}_i(t)^2 := \|\dot{q}_i(t)\|^2$. As discussed earlier, the model requires the introduction of the cell barycenters, each of which is without mass and with coordinate $r_j(t) \in \Re^2$ known upon measurements for all $j = 1, 2, \ldots, n$. To complete the model, we need in general to introduce the set of the indexes of neighbor vertices and barycenters of a given vertex $i$, which will be denoted by $V(i)$ and $B(i)$, respectively. The system has $2n_v$ degrees of freedom. As said earlier, several types of mechanical characteristics are tested. The following sections present the corresponding Lagrangians.

### The Linear Elastic Model

In the case of the Linear Elastic Model, the total energy associated with the point mass $i$ is given by the following Lagrangian:

$$L_{\mathrm{LEM}_i} = \frac{1}{2} m \dot{q}_i(t)^2 - \frac{K_v}{2} \sum_{j \in V(i)} (q_i(t) - q_j(t) - l_{1,ij})^2 - \frac{K_b}{2} \sum_{j \in B(i)} (q_i(t) - r_j(t) - l_{2,ij})^2 \tag{4.4}$$

where $K_v$ and $K_b$ are the azimuthal (vertex-vertex connectivity) and radial (vertex-barycenter connectivity) elastic moduli, respectively; $l_{1,ij}$ and $l_{2,ij}$ the resting lengths of the springs between vertex $i$ and another vertex or barycenter $j$, respectively. These resting lengths are extracted from the movie, and are calculated as the mean distance between the vertex $i$, and the corresponding point (vertex or barycenter) in such a way to reduce the number of parameters to be estimated. To this end, we need to compute the Euler Lagrange equations by using the Lagrangian $L = \sum_{i=1}^{n_v} L_{\mathrm{LEM}_i}$ as follows:

$$\frac{d}{dt}\left(\frac{\partial L}{\partial \dot{q_{ij}}}\right) - \frac{\partial L}{\partial q_{ij}} = 0\,,\ i = 1, 2, \ldots, n_v,\ j = 1, 2$$

where $q_{ij}$ denotes the $j$-th component of the mass point $i$. The resulting $2n_v$ equations can be written as follows:

$$
\begin{aligned}
(4.5) \qquad & m\ddot{q}_i(t) - K_v \sum_{j \in V(i)} (q_i(t) - q_j(t) - l_{1,ij}) \\
& - K_b \sum_{j \in B(i)} (q_i(t) - r_j(t) - l_{2,ij}) = 0,\ i = 1, 2, \ldots, n_v.
\end{aligned}
$$

Thus, the identification of the LEM requires to estimate two parameters, namely $K_v/m$ and $K_b/m$.

### The Linear Visco-Elastic Model

In the Lagrangian formalism, to represent the dissipation of energy, it is necessary to account for the Rayleigh's dissipation function. Such a function for the mass point $i$ is here denoted as follows:

$$
\begin{aligned}
(4.6) \qquad D_{\mathrm{LVEM}_i} = & -\frac{\mu_v}{2} \sum_{j \in V(i)} (\dot{q}_i(t) - \dot{q}_j(t))^2 \\
& - \frac{\mu_b}{2} \sum_{j \in B(i)} (\dot{q}_i(t) - \dot{r}_j(t))^2,
\end{aligned}
$$

Where $\mu_v$ and $\mu_b$ are the azimuthal and radial viscosity, respectively; moreover, $\dot{r}_j$ is the velocity of the $j$-th barycenter. The first term concerning the kinetic energy is the same of the LEM, i.e., $L_{\mathrm{LVEM}_i} = L_{\mathrm{LEM}_i}$. Thus, after putting all together with $L = \sum_{i=1}^{n_v} L_{\mathrm{LVEM}_i}$ and $D = \sum_{i=1}^{n_v} D_{\mathrm{LVEM}_i}$, we obtain the Euler Lagrange equations:

$$
\frac{d}{dt}\left(\frac{\partial L}{\partial \dot{q}_{ij}}\right) - \frac{\partial L}{\partial q_{ij}} - \frac{\partial D}{\partial \dot{q}_{ij}} = 0 i = 1, 2, \ldots, n_v, j = 1, 2
$$

And hence $2n_v$ equations with four parameters to be estimated, i.e., $K_v/m$, $K_b/m$, $\mu_v/m$, and $\mu_b/m$.

### The Nonlinear Visco-Elastic Model

The NLVEM takes into account the possible effect of a nonlinear elastic term, namely an elastic modulus depending linearly with elongation. Hence,

in this case the Lagrangian is composed of the following contributions for mass point $i$:

$$L_{\mathrm{NLVEM}_i} = L_{\mathrm{LVEM}_i} - \frac{k_0}{3} \sum_{j \in B(i)} (q_i(t) - r_j(t) - l_{1,ij})^3 \tag{4.7}$$

$$D_{\mathrm{NLVEM}_i} = D_{\mathrm{LVEM}_i} .$$

We can proceed to compute the Euler Lagrange equations as in the previous case. The identification of the NLVEM demands the estimation of five parameters to be estimated, i.e., $K_v/m$, $K_b/m$, $\mu_v/m$, $\mu_b/m$, and $k_0/m$.

### The Input Driven Linear Visco Elastic Model

We discussed earlier in this chapter the fact that cells could act as autonomous oscillators. We have also shown that this action taken alone failed to recapitulate cellular movement. Yet, it is possible that this behavior, taken into account together with viscosity and elasticity, would accurately represent cellular dynamics. Hence, we also developed a model in which the cells are viscous, elastic, and under the action of radial external forces accounting for Myosin II dynamics: the Input Driven Visco-Elastic Model.

Thus, the IDLVEM is just the same of the LVEM, except that the cells under the action of external forces acting on the vertices accounting for stress-independent myosin dynamics, i.e.:

$$f_i(t) = \bar{A}_i \sum_{j \in B(i)} \cos(\omega t + \phi_j) \, , \; i = 1, 2, \ldots, n_v$$

where, in order to reduce the number of parameters to estimate, the amplitude $\bar{A}_i$ is taken as the mean distance between the vertex $i$ and the neighbor barycenters in $B(i)$ and the frequency $\omega$ is considered constant from a cell to another; finally, the phase $\phi_j$ is a parameter to be identified. For the other cases, the parameters optimized are those that account for elasticity and viscosity. Summing up, the parameters to be determined are the following: $\phi_1$, $\phi_2$, …, $\phi_n$, $K_v/m$, $K_b/m$, $\mu_v/m$, and $\mu_b/m$.

### 4.3.2 Optimization

To find the best fitting parameters, we performed a least squares optimization, in order to find the models parameters allowing to obtain the best fit possible to biological data, for each model.

Based on the video processing presented in the previous chapter, we have indeed at disposal the measures of $q_i(t)$, $r_j(t)$ and $\dot{r}_j(t)$ for all $i$ and $j$ at given time instants $t = kT$ with $k = 1, 2, \ldots, K$ with uniform sampling time $T$ equal to 6 s. Let us denote such measures with $y_{q_i}(k)$, $y_{r_j}(k)$, and $\dot{y}_{r_j}(k)$ and let $y_q(k) := (q_1(k), q_2(k), \ldots, q_{n_v}(k)) \in \Re^{n_v}$, $y_r(k) := (r_1(k), r_2(k), \ldots, r_n(k)) \in \Re^n$, and $\dot{y}_r(k) := (\dot{r}_1(k), \dot{r}_2(k), \ldots, \dot{r}_n(k)) \in \Re^n$. Moreover, let $l_1 := \mathrm{col}(l_{1,ij}, i = 1, 2, \ldots, n_v, j \in V(i))$, $l_2 := \mathrm{col}(l_{2,ik}, i = 1, 2, \ldots, n_v, k \in B(i))$, and finally $l_0 = (l_1, l_2)$.

Following the least squares approach, we may regard the discretized Euler Lagrange equations derived from either LEM or LVEM or NLVEM or IDLVEM as constraints to take into when performing the optimization to find the best fitting parameters denoted by the parameter vector $p$, which depends on the specific model, as described in Section 6.3. Toward this end, let us refer to the generic discretized Euler Lagrange equation given by

$$q(k+1) = F_T\left(q(k), y_r(k), \dot{y}_r(k), l_0, p\right) ,$$
$$k = 1, 2, \ldots, K-1$$

with the objective cost function

$$J = \sum_{k=1}^{K} \left\| y_q(k) - q(k) \right\|^2$$

to be minimized. Such constraints are obtained by the Runge-Kutta method with the variable time step. For a proper comparison with biological data, the model output was resampled to fit data sampling. For a set of biological data taken at time steps $k = 1, 2, \ldots, K$ and integration steps going from $t_{int} = t_0, \ldots, t_{fin}$, the integration step $t_{int}$ corresponding to the data time step $k$ is taken as the nearest integer of the ratio of the final integration

time over the last data time step, times $k$, i.e.: $t_{int} = [k.\frac{t_{fin}}{K}]$. Thus, in the various modeling cases we need to solve the following prototype problem

$$\min_{p,q(2),\ldots,q(K)} \sum_{k=2}^{K} \|y_q(k) - q(k)\|^2 \tag{4.8a}$$

(4.8b) subject to

$$q(k+1) - F_T\left(q(k), y_r(k), \dot{y}_r(k), l_0, p\right) = 0,$$

$$k = 1, 2, \ldots, K-1 \tag{4.8c}$$

$$q(1) - y_q(1) = 0\,. \tag{4.8d}$$

### 4.3.3 Model Identification

After identifying the best fitting parameters by solving 6.2, it is necessary to asses the validity of the resulting model by using some specific tools. More precisely, as usually done in identification problems, we performed the autocorrelation test of the residuals $e_z(k) = q_i(k) - \hat{q}_i(k)$ w.r.t. a given output $q_i(k)$, where $\hat{q}_i(k)$ is its prediction given by the identified model, by using its autocorrelation function

$$R_z(\sigma) = \frac{\sum_{t=\sigma}^{N}(e_z(k) - \bar{e_z})(e_z(k-\sigma) - \bar{e_z})}{\sum_{t=0}^{N}(e_z(k) - \bar{e_z})^2} \tag{4.9}$$

where $\bar{e_z} = \sum_{k=1}^{K} e_z(k)/(K+1)$. The plots of (6.3) for the various identified models are shown in Figure 6.4, where the confidence bands are defined as $\pm 1.96/\sqrt{K}$. Table 6.1 reports the mean percentage of the out-of-band scores obtained by the autocorrelation functions over all the vertices.

**Table 4.1:** *Mean percentages of out-of-band points of the autocorrelation functions.*

| | LEM | LVEM | NLVEM | IDLVEM | LVEMcons | NLVEMcont |
|---|---|---|---|---|---|---|
| % | 2.8 | 4.6 | 3.9 | 1.9 | 7.9 | 2.9 |

The results of the identification are displayed also in the form of a movie showing the position of the predicted points on the segmented movie). The

cell area extracted from the movie is also plotted versus the predicted one, as shown in Figures 4.10 to 4.14. These results will be discussed in Chapter 6.

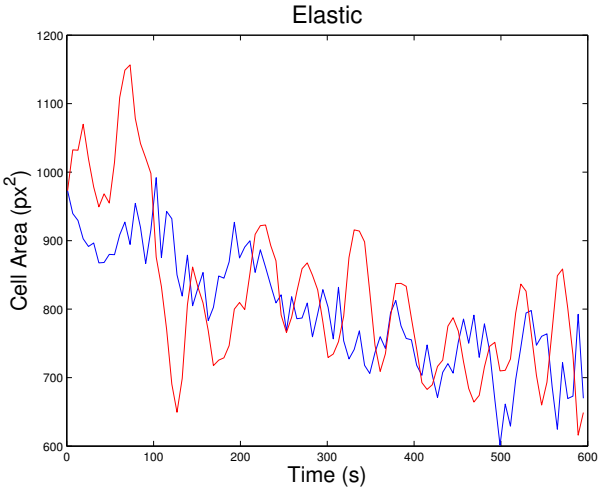


**(a)** *Plot of the cell area over time (red curve) and its prediction based on the identified model (blue curve).*

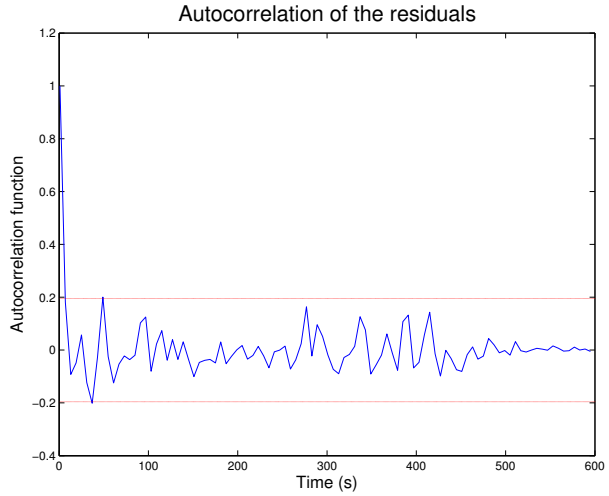


**(b)** *Plot of the autocorrelation function (the 95% bands are depicted with the red lines).*

**Figure 4.10:** *Plots of the autocorrelation function, and of the cells area over time versus its prediction, for the Linear Elastic Model.*

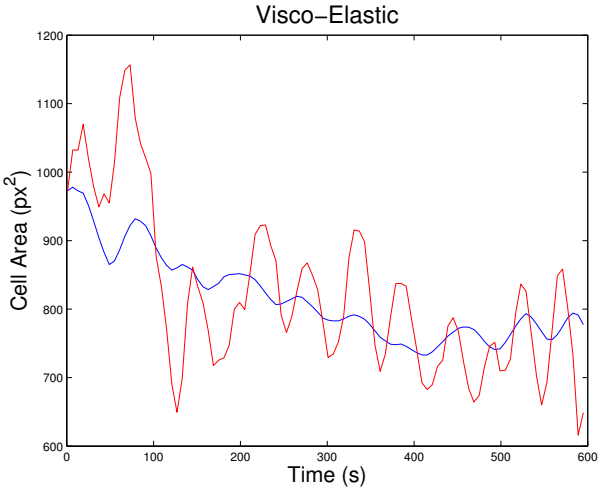


**(a)** *Plot of the cell area over time (red curve) and its prediction based on the identified model (blue curve).*

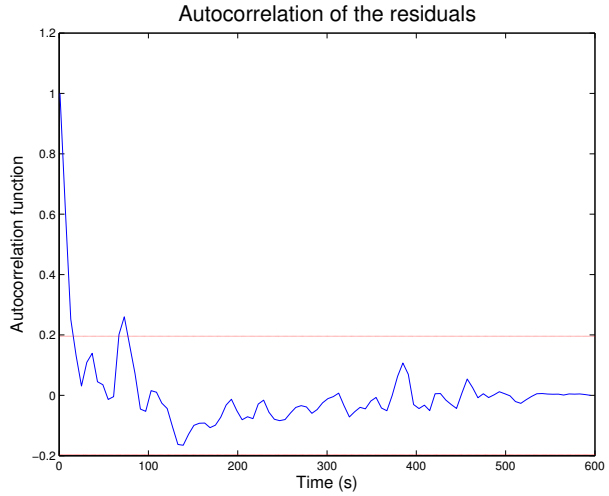


**(b)** *Plot of the autocorrelation function (the 95% bands are depicted with the red lines).*

**Figure 4.11:** *Plots of the autocorrelation function, and of the cells area over time versus its prediction, for the Linear Visco Elastic Model.*

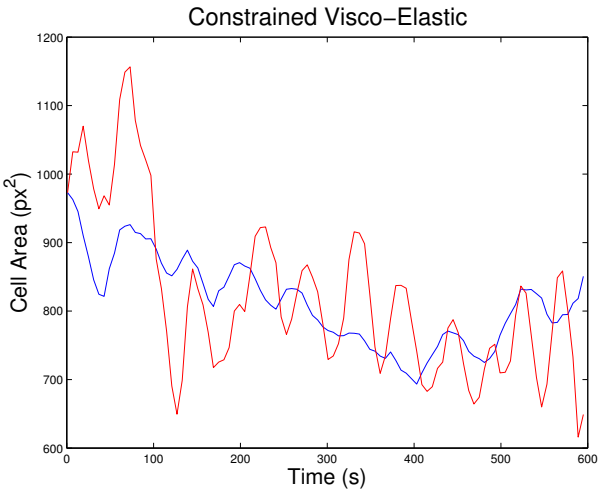


**(a)** *Plot of the cell area over time (red curve) and its prediction based on the identified model (blue curve).*

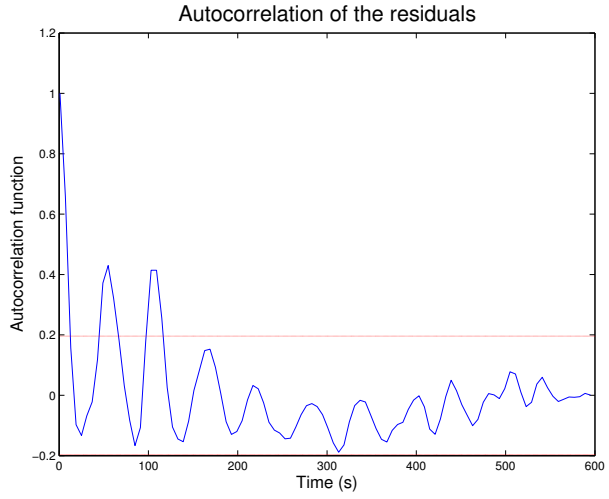


**(b)** *Plot of the autocorrelation function (the 95% bands are depicted with the red lines).*

**Figure 4.12:** *Plots of the autocorrelation function, and of the cells area over time versus its prediction, for the Linear Visco Elastic Model, with constrained viscosity.*

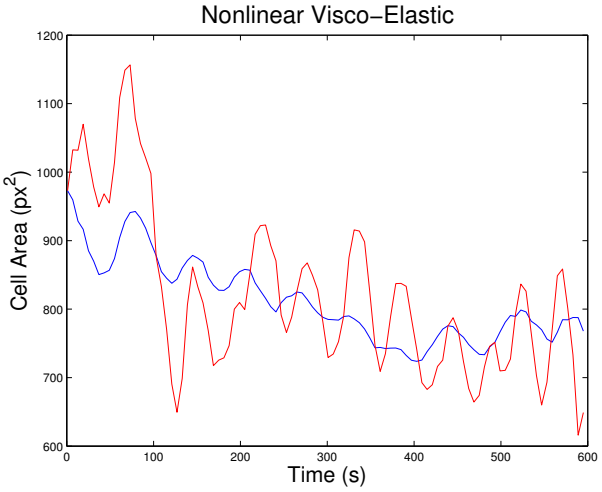


**(a)** *Plot of the cell area over time (red curve) and its prediction based on the identified model (blue curve).*

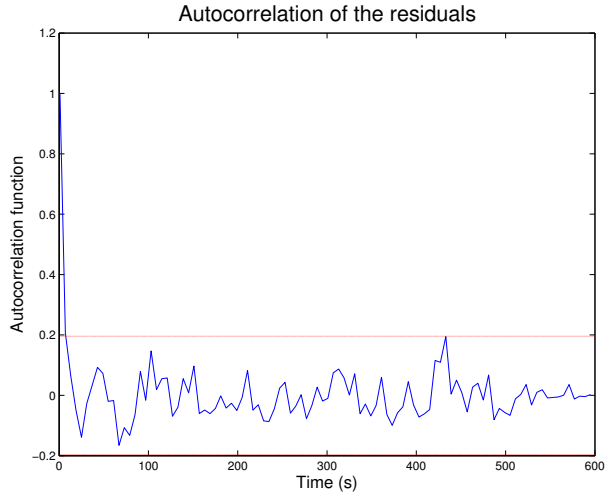


**(b)** *Plot of the autocorrelation function (the 95% bands are depicted with the red lines).*

**Figure 4.13:** *Plots of the autocorrelation function, and of the cells area over time versus its prediction, for the Non Linear Visco Elastic Model.*

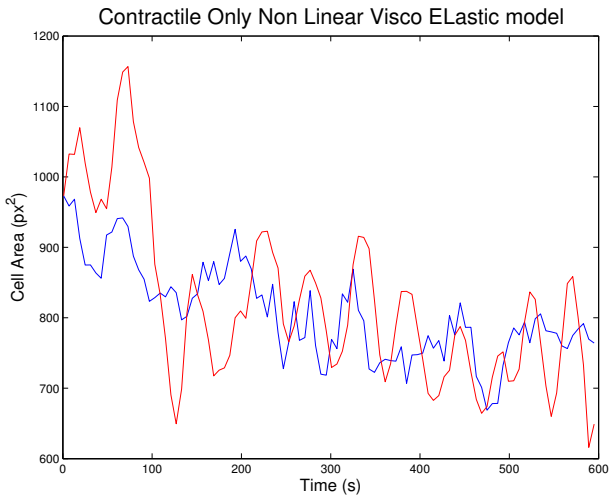


**(a)** *Plot of the cell area over time (red curve) and its prediction based on the identified model (blue curve).*

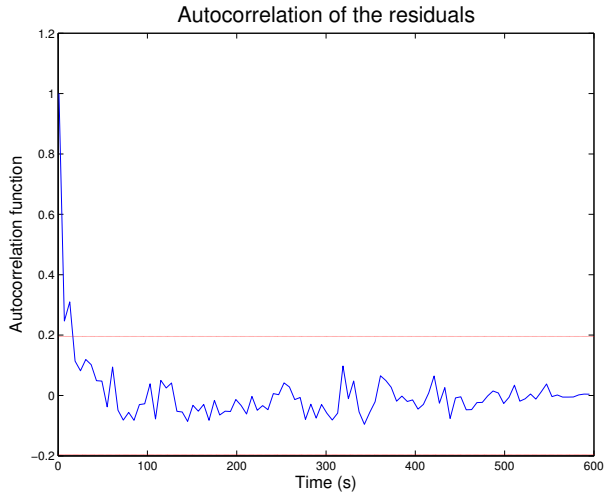


**(b)** *Plot of the autocorrelation function (the 95% bands are depicted with the red lines).*

**Figure 4.14:** *Plots of the autocorrelation function, and of the cells area over time versus its prediction, for the Non Linear Visco Elastic Model, contractile only.*

# Chapter 5

# A study of Leading Edge dynamics

As discussed in the introduction, the actin cable is an important feature of dorsal closure. Formed by the dorsal most epidermal cells, it is known to increase the closure rate.
Various studies have discussed the type of action the Actin Cable would perform on Dorsal Closure. Some of them describe it as a "Purse String" mechanism, i.e. a rope-like structure surrounding the dorsal hole and decreasing its length, therefore contributing to the decrease of the area it encloses.
Other recent works suggest that the effect of the Actin Cable could be a "Ratchet-like" mechanism. Given that Amnioserosa cells oscillate, their area alternates between shrinked and expanded states, the actin cable may prevent the amnioserosa cells to reach back an expanded state, once they are shrinked.
Another possibility, since the Actin Cable is a trans-cellular structure, would be that it helps synchronizing the Leading Edge cells, increasing the synchrony, and hence the efficiency, of their dorsalward movements.
With the segmentation and point tracking tool at hand, we wanted to assess these putative effects of the Actin Cable on Dorsal Closure. A fly strain showing an absence of Actin Cable during Dorsal Closure (carrying a mutation called *Zasp52*$\Delta$), and also expressing the fluorescent protein Shg::GFP,

present at the cells membrane, was generated in the lab.
Although the Actin Cable is defective in this mutant, the rest of the Dorsal Closure seems rather unharmed: the embryo reaches a full closure (even though delayed), the Leading Edge cells still elongate during the process, and amnioserosa cells still oscillate. These observations suggest that the mutation is highly specific and only affects the Actin Cable. Therefore, studying the differences of behavior of the Leading Edge between mutant and control embryos, we expect to find valuable information on the role of Actin Cable during Dorsal Closure.

First, we segmented movies of *Zasp52*$\Delta$ mutant and control embryos, and tuned the program to characterize Leading Edge cells and not only Amnioserosa cells. We were able to detect the vertices of the Leading Edge cells. Vertices are much closer to each other in the Leading Edge than in the Amnioserosa, and yet show important global movements: due to the Dorsal Closure dynamics, the whole set of vertices is likely to move together. Hence, a vertex may move from its position at time $t$, to a point at time $t+1$ close to the position of its neighbor vertex at time $t$, causing tracking defects that were absent in the Amnioserosa. These defects were corrected manually, changing the values in the matrix carrying the vertices positions. The tracking was then run again starting with the changed value.
Another issue was the insertion of mixer cells [75] among the Leading Edge cells. The distance between the two points between which the mixer cell fitted were ignored in the following calculations.

Once the positions are determined, we can go on to calculate the dorsal ward movements in mutant and wild type. To do so, the distance covered by a vertex between the time points $t$ and $t+1$ was given the sign of the angle of the trajectory with respect to the horizontal:
Let $\vec{q_i}(t) = (x_i(t), y_i(t))$ and $q_i(t+1) = (x_i(t+1), y_i(t+1))$ be the position of the $i^{th}$ vertex at time $t$ and $t+1$, respectively. $\vec{MN} = \vec{q_i}(t+1) - \vec{q_i}(t)$. Let $\overline{D_i}$ be the signed distance covered by a vertex. Hence,

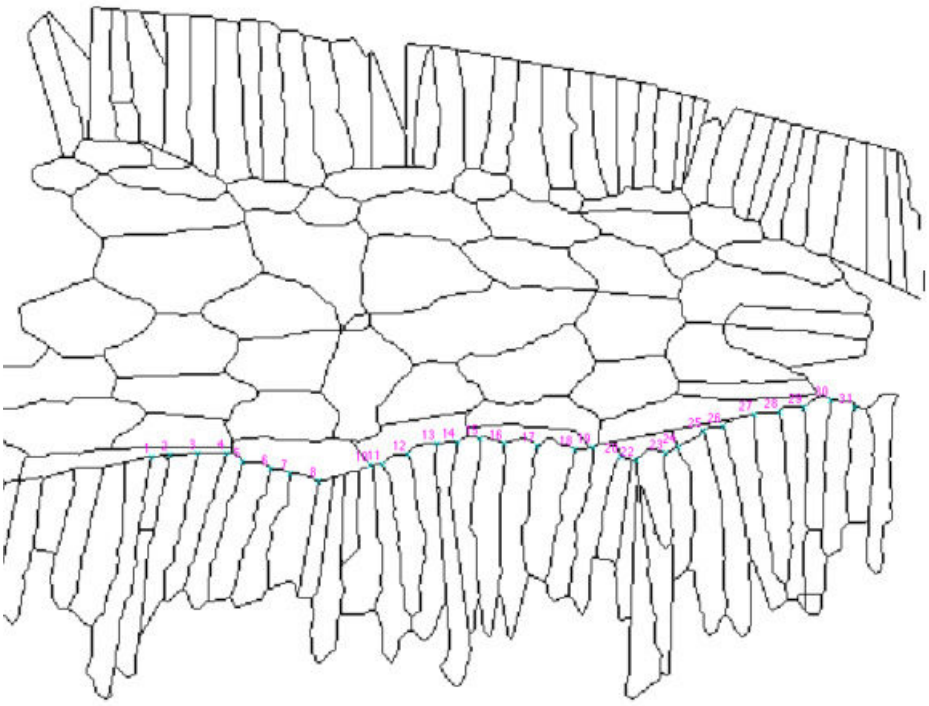

**(a)** *Control Embryo*

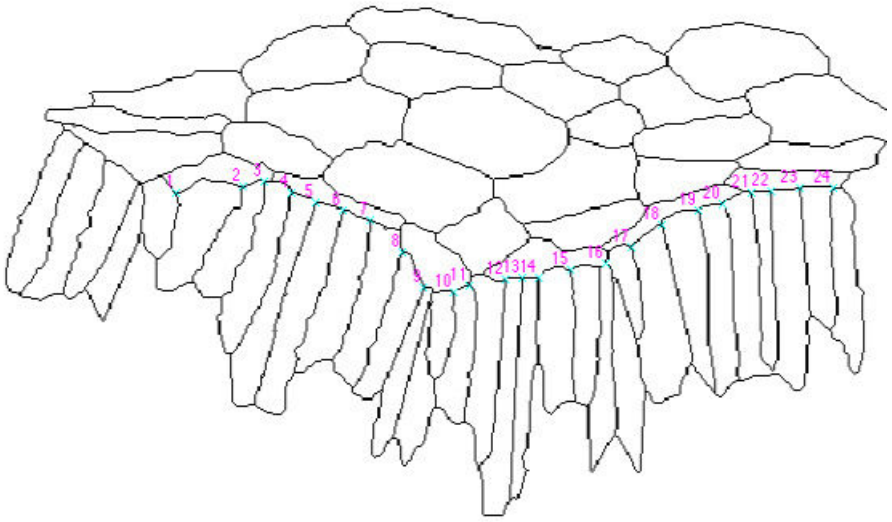

**(b)** *Zasp52δ mutant embryo*

**Figure 5.1:** *Segmented pictures for a control and a Mutant embryo. The tracked points are labeled.*

(5.1)
$$\overline{D_i} = \sqrt{(x_i(t+1) - x_i(t))^2 + (y_i(t+1) - y_i(t))^2}.sgn(arctan(\frac{y_i(t+1) - y_i(t)}{x_i(t+1) - x_i(t)})),$$

since $tan((Ox), \vec{MN}) = \frac{y_i(t+1) - y_i(t)}{x_i(t+1) - x_i(t)}$.
The segmented embryos are oriented with their antero-posterior axis along the horizontal axis. Therefore, the strategy presented here allows to count the number of dorsalward, and ventralward movements, and to measure their amplitude. The results obtained are presented in Figure 5.2 and 5.3, for a Control and a Mutant embryo, respectively. To compare these two embryos, the same time sampling and magnification were used.

The first striking information emerging from these figures is the obvious presence of negative displacements. This observation is hard to reconcile with the Ratchet theory.

Another hypothesis on the Actin Cable action is that it would generate an inward force by contracting and decreasing its length, thus participating in the decrease of the dorsal hole. With these histograms, this hypothesis also appears unlikely. Indeed, the difference between the mean displacement values is not striking between the mutant and the control embryo. It is even lesser for the control embryo, but in a non conclusive manner, since such a small difference could come from either biologic variation or a small defect in the antero-posterior orientation of the embryos.

Another striking feature is the spreading of the displacement values in the mutant embryo, compared to the control embryo. Wider movements are totally absent in the control embryo, while small displacements occur less in the mutant embryo. It is not such a surprising observation: one can easily observe on a live movie that mutant embryos movements of the Leading Edge are much wider than the control ones. Yet, this observation, together with the fact that the mean displacement is not strikingly different between the two cases, shows that the Actin Cable constrains the cells, in the same

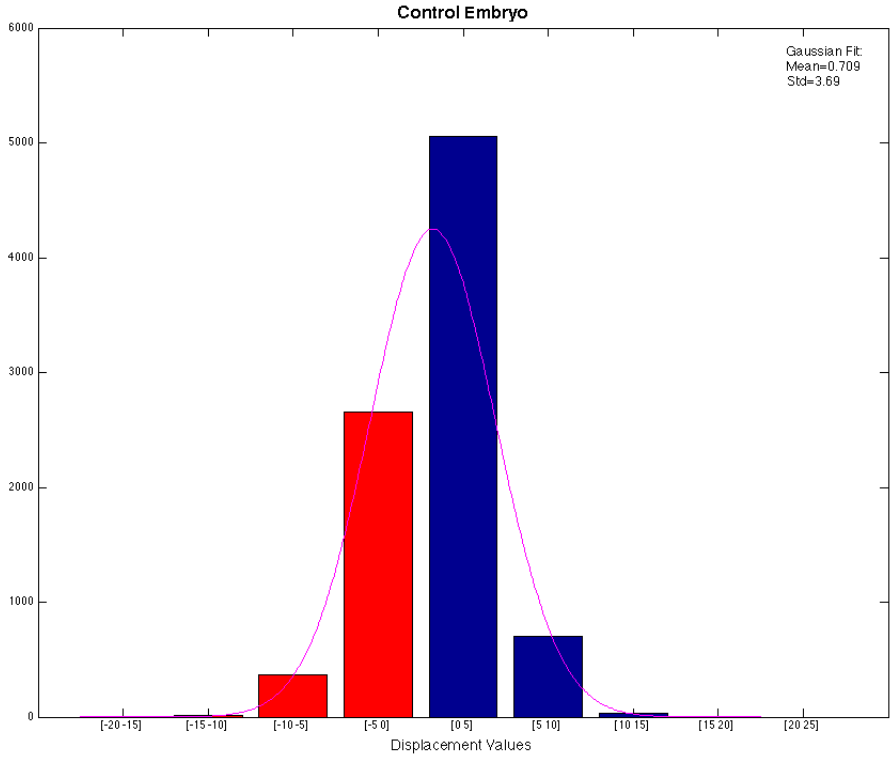


**Figure 5.2:** *Histogram grouping the values of signed distance covered by a vertex in eight classes, in a Control Embryo. In red, the negative values, in blue, the positive values, and in magenta, the gaussian fit of the repartition of the data.*

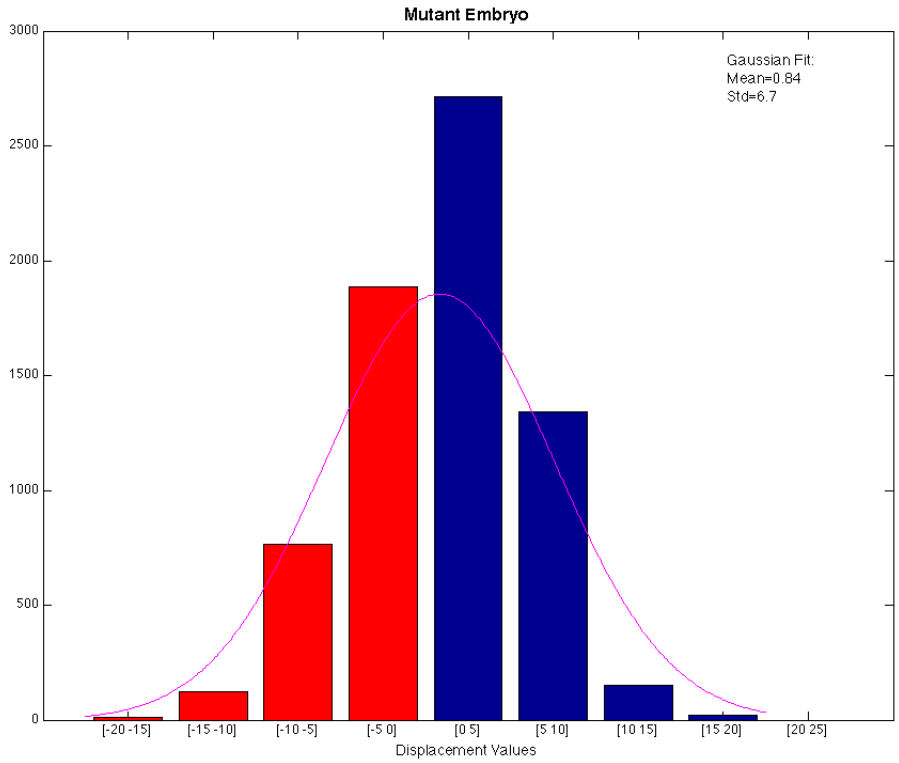


**Figure 5.3:** *Histogram grouping the values of signed distance covered by a vertex in eight classes in a Mutant Embryo. In red, the negative values, in blue, the positive values, and in magenta, the gaussian fit of the repartition of the data.*

manner in their forward and backward movements.

Hence, the Actin Cable constrains cells movements both forwardly and backwardly, and the forward bias observed in the histograms does not show any difference between mutant and control embryos (the mean displacement value is comprised between +0.5 and +1 in both cases). Thus, the Actin cable does not only prevent backward movements, but only prevents long range movements. Neither does it increase the forward movement. Therefore, we wondered whether the Actin Cable would improve the efficiency of the forward movement by synchronizing cellular movements.

Leading Edge displacements have indeed the appearance of a sinusoidal signal perturbed by noise. We wondered what type of effect the Actin Cable would have on this signal, and in particular whether it would help synchronizing the Leading Edge movement, i.e. reduce the dispersion of the phases and frequencies. Therefore, we have used the Hilbert transform of the vertices' movement to extract the phases and frequencies values.

In order to obtain the phase and the frequency of the Leading Edge movement, we need to extract the instantaneous phase of the movement. As shown in Figure 5.4, the vertices movement behaves like a perturbed sinusoidal signal. Hence, it can be considered as a real signal. Being a real signal, it can be written as $g(t) = A(t)cos(\theta(t))$. In a real signal, negative frequencies are always present. Indeed, $cos(\theta(t)) = \frac{e^{i\theta(t)} - e^{-i\theta(t)}}{2}$. Hilbert transform allows to get rid of the negative frequencies. Since $H\{g\}(t) = A(t)sin(\theta(t))$, we can write:

$$\frac{g(t) + iH\{g\}(t)}{2} = A(t)(cos(\theta(t) + i.sin(\theta(t))) \tag{5.2}$$

which yields:

$$g(t) + iH\{g\}(t) = A(t).e^{\theta(t)} \tag{5.3}$$

From there, extracting the instantaneous phase is straightforward, negative frequencies are absent, and we got rid of the ambiguity coming from the periodicity of the *sin* and *cos* functions.

The general expression of the instantaneous phase is $\theta(t) = \omega(t).t + \phi(t)$. $\omega$ and $\phi$ may vary over time. Interestingly, for every vertex considered here, the instantaneous phase can be fitted with a great accuracy by a linear function, as shown in Figure 5.5. This result indicates that the frequency and the initial phase of the movement can be considered constant for every vertex. Therefore, we can extract the frequency and the phase of the movement of every vertex, fitting the data with a polynomial of order one. The frequency is the coefficient of order one, and the initial phase the coefficient of order zero. As one can see in Figure 5.5, the Control embryo has two regimes. This breaking point appears $3200s$ after the beginning of the movie, that correlates with the formation of the Actin Cable. Hence, two curve fittings were performed for the Control embryo, one for the first 3200 seconds, and one for the rest of the movie, and two frequencies and initial phases were extracted for each vertex. Once these values were extracted, we calculated the mean values and the standard deviations for the initial phase and the frequency, for the two regimes of the Control embryo and for the Mutant embryo. Results are shown in Figure 5.6.

The first phase of the Control embryo shows a mean frequency and initial phase with a dispersion of the same order than the Mutant (see values in Table 5.1). On the contrary, the formation of the Actin Cable generates a change of mean frequency (decreased by a factor of almost 3). It also dramatically increases the spreading of the frequency values (by a factor of 5, roughly). The study of the values of the phase, and its standard deviation, only show that the dispersion of the values seems to be embryo dependent: it does not vary between the two phases, but vary greatly between the Control and the Mutant embryos. No tendency emerges from the mean values.

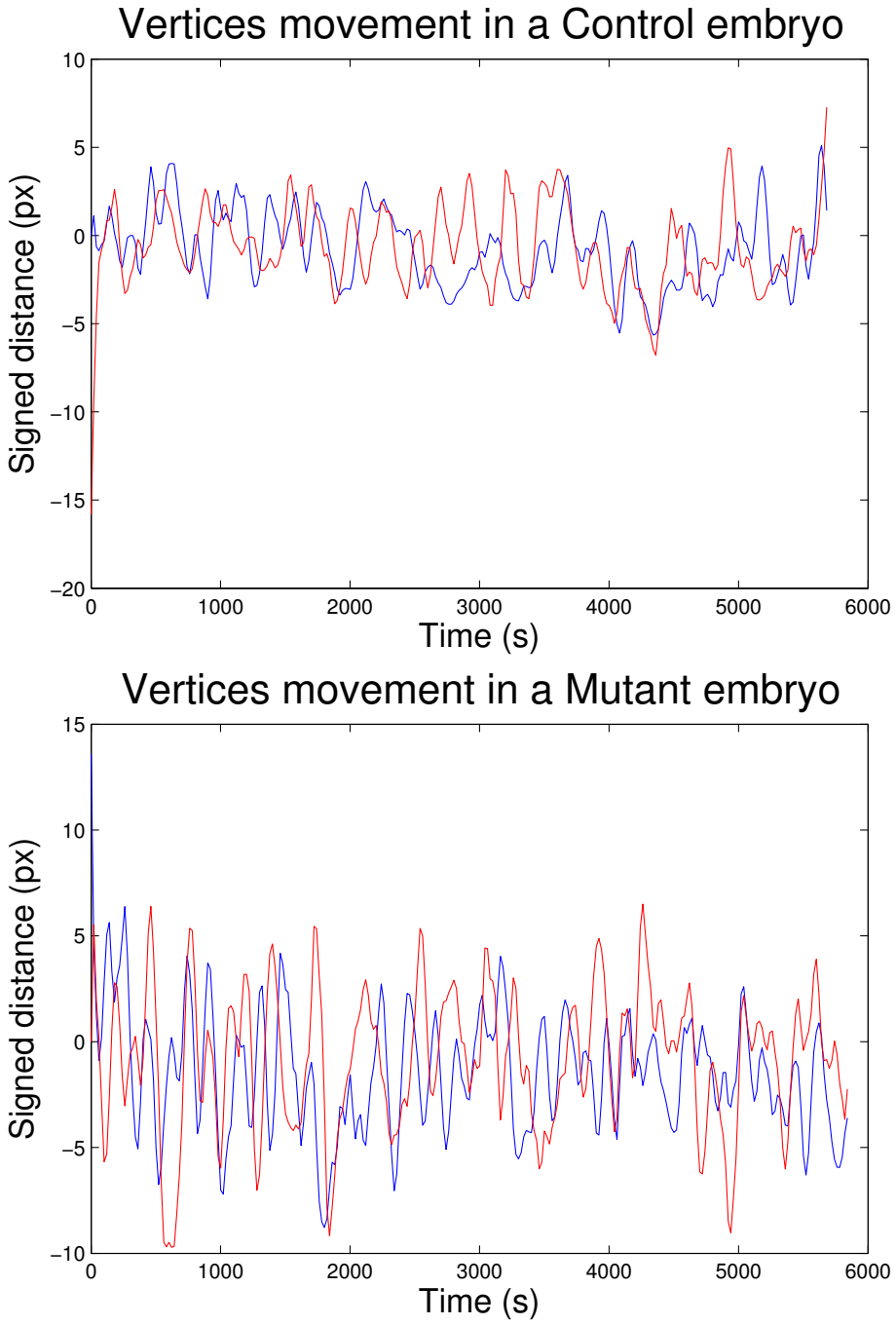


**Figure 5.4:** *Plot of the signed distance for two vertices. In the upper panel, the dynamics of two vertices in a Control embryo. In the lower panel, the dynamics of two vertices in a Mutant embryo.*

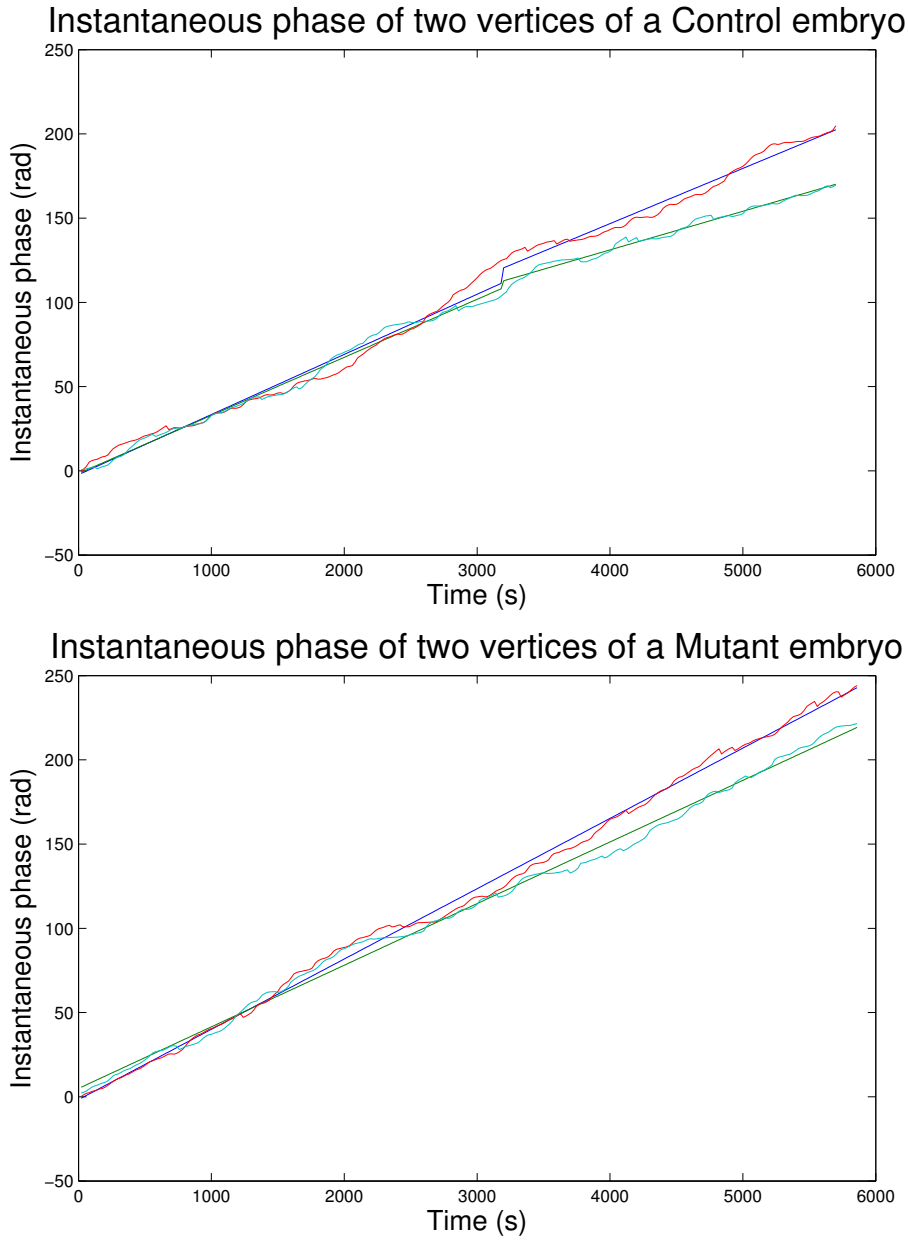


**Figure 5.5:** *Plot of the Instantaneous phase of two vertices, in a Control embryo (upper panel), and in a Mutant embryo (lower panel). In blue and green, the trends, in cyan and red, the real values.*

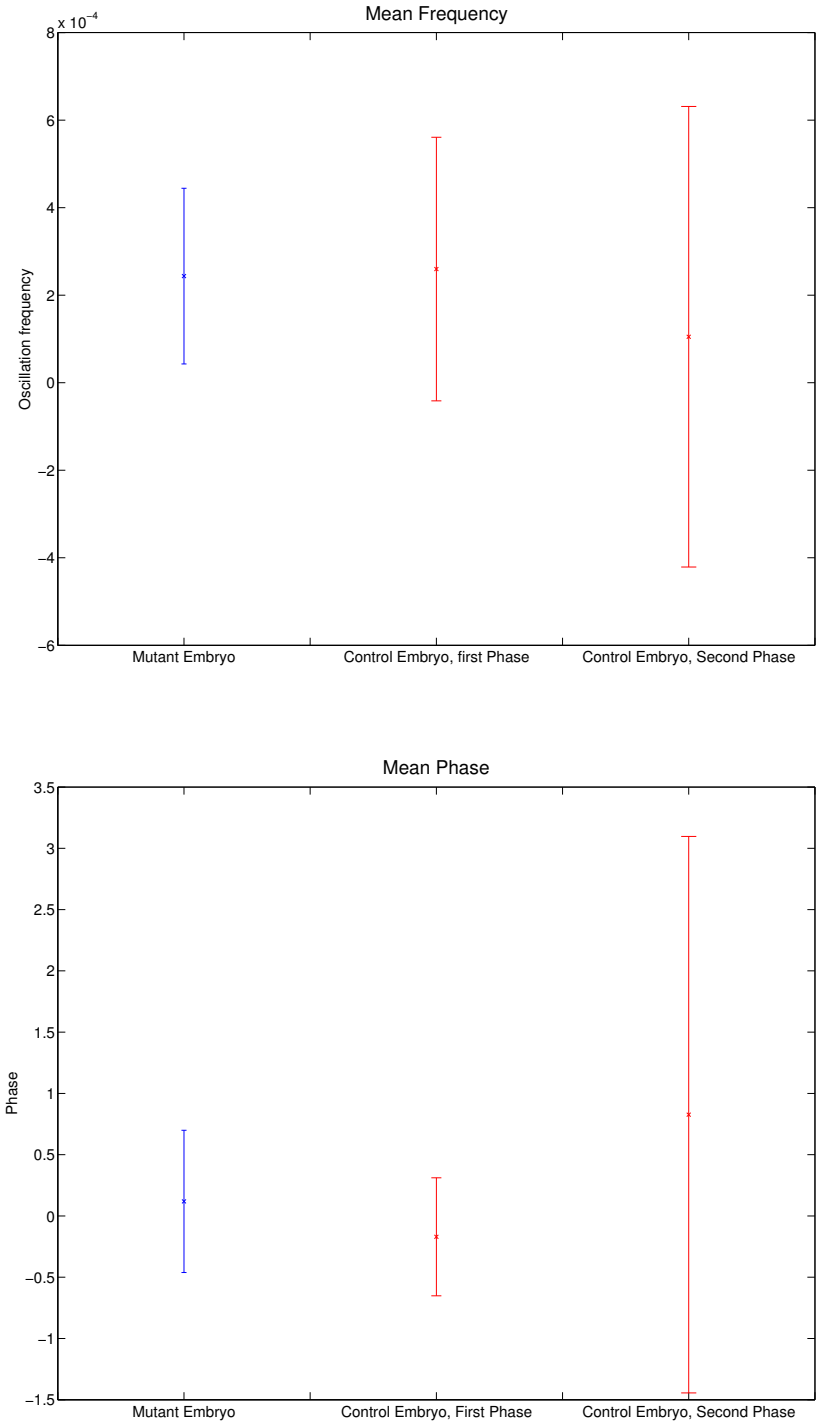


**Figure 5.6:** *Plot of the Instantaneous phase of two vertices, in a Control embryo (upper pannel), and in a Mutant embryo (lower pannel). In blue en green, the trends, in cyan and red, the real values.*

| | | Mean | S.D. | % ($\frac{f}{\sigma}$ & $\frac{\phi}{\sigma}$) |
|---|---|---|---|---|
| Frequency | Mutant | $3.9.10^{-5}\,Hz$ | $3.18.10^{-5}\,Hz$ | 81% |
| | Control, $1^{st}$ Phase | $4.14.10^{-5}\,Hz$ | $4.79.10^{-5}\,Hz$ | 116 % |
| | Control, $2^{nd}$ Phase | $1.59.10^{-5}\,Hz$ | $8.39.10^{-5}\,Hz$ | 526 % |
| Phase | Mutant | $0.12\,rad$ | $0.58\,rad$ | 483% |
| | Control, $1^{st}$ Phase | $-0.17\,rad$ | $0.48\,rad$ | 282 % |
| | Control, $2^{nd}$ Phase | $0.8\,rad$ | $2.27\,rad$ | 284 % |

**Table 5.1**

This study showed that the formation of the Actin Cable does not increase the mean forward movement. Neither does it prevent bacward movements. The Actin Cable constrains the cells movements, both forwardly (dorsalward movement) and backwardly (ventralward movement). Yet, constraining the movement increases the frequency spectrum present in the oscillatory movements of the Leading Edge, and the formation of the Cable increases the closure speed. Hence, since the Actin Cable does not seem to have any mechanical effect, the influence of the geometrical changes induced by the appearance of the Cable (Dorsal hole shape, Leading Edge straightness) must be assessed.

# Chapter 6

# Modeling and Identification of Amnioserosa Cell Dynamics by Using Mass Spring Lattices

**Submitted in:** IEEE Transactions on Computational Biology And Bioinformatics

## 6.1 Abstract

We propose various mechanical models of a live amnioserosa cell during *Drosophila melanogaster*'s dorsal closure and identify the related parameters. Such models are based on a Lagrangian approach and account for specific biomechanical behaviors. The identification of the parameters that fit best the cellular dynamics extracted from live images is accomplished according to a least-squares approach, where the dynamic behavior is explicitly taken into account as a constraint. For the purpose of comparison, the validation of the resulting models is performed by using the autocorrelation function of the residuals.

## 6.2 Introduction

Mass-spring-damper lattice models are successfully used to model 2D cellular systems [76, 77], as they recapitulate two main physical features of live tissues, namely viscosity and elasticity. Whereas viscosity enables the system to dissipate the energy it receives, elasticity allows the system to store energy. Viscosity and elasticity have been widely used in biology to model the dynamics of cells and tissues under constraints, whether considering them only viscous [78], or both viscous and elastic [79]. In addition, cells can react to external actions or molecular signals, and to adapt their mechanical characteristics. Such phenomenon is due to mechanical stress, and it is either called stress softening in case of decrease of cell's stiffness or stress stiffening in case of increase [58, 80]. Moreover, cell and tissue dynamics may also be modelled with an extra nonlinear elastic term and hence with a stiffness that depends on the applied force.

Mechanical characteristics are also very difficult to probe in vivo. Most of the biomechanical studies are performed in vitro, on single molecules [43,81], single cells [82, 83], or minimal systems such as in-vitro grown molecular networks [84,85]. Laser perturbations can also provide valuable information [63, 70], although it can be very damaging for the organism studied. In view of this, numerical studies may be helpful to provide a handy tool for estimating the mechanical properties of biological systems in a non-invasive manner. In the past few years, several works were focused on forces and deformations in live organisms [72, 86]. Yet, none of them allows one to study the parameter variations over time, and neither do they permit to assess the mechanical characteristics of a tissue.

In this work, we address the problem of estimating the mechanical characteristics of a living tissue using Lagrangian formalism and least squares optimization. This method only requires positional measures extracted from movies of the tissue acquired thanks to confocal fluorescence microscopy. A system of Lagrangian equations with generalized coordinates is derived to account for specific mechanical behaviors that depend on a set of param-

eters specific for each model. Such parameters are estimated by solving a constrained least squares problem and validated by means of a convenient statistical test. An approach to modeling and identification of planar cell polarity dynamics is reported in [87] with the goal of matching theory, simulation, and experiment. In this paper, we pursue a similar objective, as the accuracy of the fit with biological data allows one to identify the particular mechanical model of the cellular dynamics.

The paper is organized as follows. Section 6.3 presents the complete family of models under investigation. The method adopted for the identification of such models and the results of the validation on the identified models are shown and discussed in Section 6.4. Finally, the conclusions are drawn in Section 6.5.

## 6.3 Lagrangian modeling

*Drosophila melanogaster* embryo's dorsal closure is a process consisting in the closure of a dorsal hole in the epidermis, covered by a tissue called amnioserosa, and surrounded by a cable made of actomyosin fibers. The use of *Drosophila* powerful genetics may be ascribed to the ease of live imaging, it shows great similarities with ventral enclosure in *Caenorhabditis elegans* [88] and *Funduli*'s epiboly formation [89], as well as wound healing [37] and eyelid formation in mammals [90]. Interestingly, amnioserosa cells play a major part in the process, although it leads to their removal [24]. They also show a peculiar behavior: their area varies periodically. This is due to the periodic assembly/disassembly of the apical cytoskeleton [27]. Indeed, in the center of the apex, the non-muscular myosin II interacts with actin filaments to induce cyclic contractions, whereas this complex is continuously present at the edges of the cell, enabling stable cell adhesion. Myosin II is also phosphorylated during the process, increasing cell contractility. This feature is a crucial component for dorsal closure dynamics [74], and is also known to be involved in cell-stiffening [58]. Nevertheless, there is no proof that stress-stiffening is involved in Amnioserosa cells contraction, and cell area

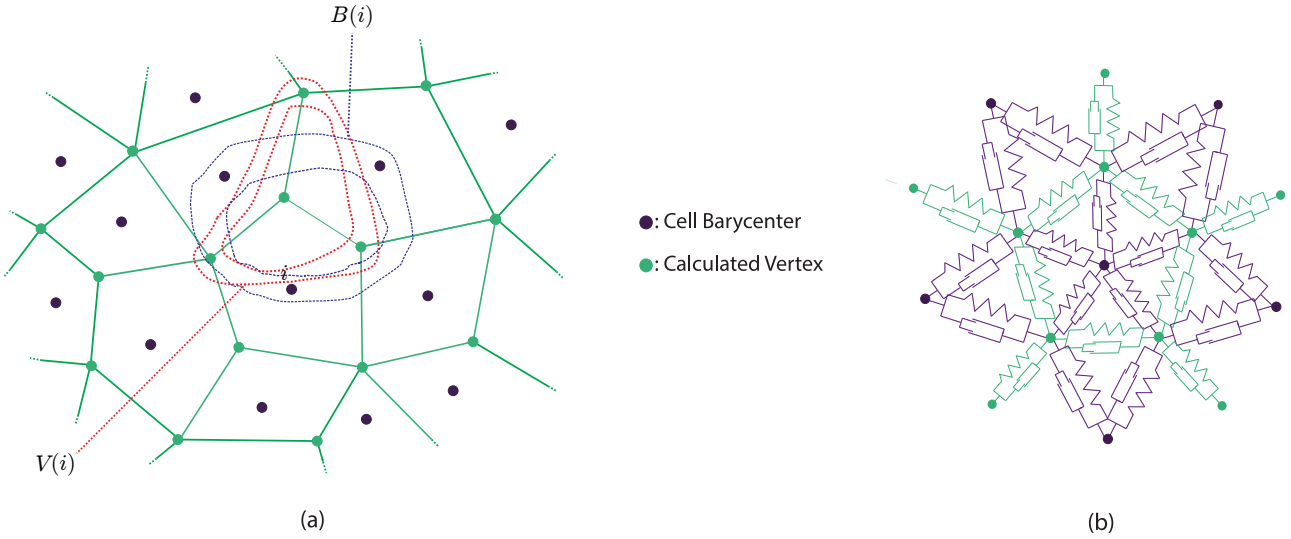


**Figure 6.1:** *(a) An example of system of cells. The green and purple nodes represent calculated vertices and cell barycenters, respectively. The green segments stand for the apical junctions of the cells. (b) As detailed, two distinct types of spring-damper link are considered: some joining the vertices together (corresponding to the apical junctions, in green) and other joining vertices with the cell barycenters (in purple).*

variation may come either from molecular signalling (i.e., the stiffening is independent of the stress applied) or from the stress-stiffening phenomenon, as it will be discussed later on.

In order to avoid heavy computation and preserve the predictive capability of our model, we decided to group mechanical parameters into two distinct sets: one accounting for the radial contribution of the cells, and one accounting for the azymuthal contribution. Except for the points mass, which we consider constant for every vertex.

To represent the cellular dynamics, we rely on lattice models such as that depicted in Fig. 6.1. Such a model is in general composed of $n$ cells with $n_v$ vertices, each of which is a junction among cells. Such vertices are regarded as the focal points of forces in the tissue and represented by point masses of Cartesian 2D coordinates (with respect to a fixed frame) denoted by $q_i(t) \in \Re^2$ at time $t \geq 0$ for $i = 1, 2, \ldots, n_v$ with $q_{i,j}$ denoting

the $j$-th component of the coordinate of the mass point $i$ (clearly, $j = 1, 2$). We assume that the mass of each of such points is $m$ and, for the sake of brevity, let $q_i(t)^2 := q_{i,1}(t)^2 + q_{i,2}(t)^2$. Thus, the velocity of the mass point $i$ at time $t$ is denoted by $\dot{q}_i(t) \in \Re^2$ and similarly let $\dot{q}_i(t)^2 := \dot{q}_{i,1}(t)^2 + \dot{q}_{i,2}(t)^2$. Moreover, let $q_i(t)^3 := q_{i,1}(t)^3 + q_{i,2}(t)^3$.

The model requires also the introduction of the cell barycenters, each of which is without mass and with coordinate $r_j(t) \in \Re^2$ known upon measurements for all $j = 1, 2, \ldots, n$. To complete the model, we need in general to introduce the set of the indexes of neighbor vertices and barycenters of a given vertex $i$, which will be denoted by $V(i)$ and $B(i)$, respectively. The system has $2n_v$ degrees of freedom and in the following we will describe different dynamic models by using a Lagrangian approach with a specific energy function. More precisely, we will analyze four models: (a) linear elastic (LEM), (b) linear visco-elastic (LVEM), (c) nonlinear visco-elastic (NLVEM), and (d) input-driven linear visco-elastic (IDLVEM).

In the case of the LEM, the total energy associated with the point mass $i$ is

$$\begin{aligned} L_{\mathrm{LEM}_i} = \frac{1}{2} m \dot{q}_i(t)^2 - \frac{K_v}{2} \sum_{j \in V(i)} (q_i(t) - q_j(t) - l_{1,i,j})^2 \\ - \frac{K_b}{2} \sum_{j \in B(i)} (q_i(t) - r_j(t) - l_{2,i,j})^2 \end{aligned} \tag{6.1}$$

where $K_v$ and $K_b$ are the azimuthal (vertex-vertex connectivity) and radial (vertex-barycenter connectivity) elastic moduli, respectively; $l_{1,i,j}$ and $l_{2,i,j}$ the resting lengths of the springs between vertex $i$ and another vertex or barycenter $j$, respectively. These resting lengths are calculated using the video sequence as the mean distance between the vertex $i$, and the corresponding point (vertex or barycenter) in such a way to reduce the number of parameters to be estimated. Based on (6.1), we obtain the Euler Lagrange equations

$$\frac{d}{dt} \left( \frac{\partial L}{\partial \dot{q}_{i,j}} \right) - \frac{\partial L}{\partial q_{i,j}} = 0 \,, \; i = 1, 2, \ldots, n_v, \; j = 1, 2$$

where

$$L = \sum_{i=1}^{n_v} L_{\mathrm{LEM}_i}$$

is the Lagrangian. The resulting $2n_v$ equations can be written as follows:

$$\begin{aligned} & m\ddot{q}_i(t) - K_v \sum_{j \in V(i)} (q_i(t) - q_j(t) - l_{1,i,j}) \\ & - K_b \sum_{j \in B(i)} (q_i(t) - r_j(t) - l_{2,i,j}) = 0,\ i = 1, 2, \ldots, n_v. \end{aligned}$$

Thus, the identification of the LEM requires to estimate two parameters, namely $K_v/m$ and $K_b/m$.

For the LVEM, it is necessary to account for the Rayleigh's dissipation function, which is often used in Lagrangian mechanics to represent energy loss due to friction. Such a function for the mass point $i$ is here denoted as follows:

$$\begin{aligned} D_{\mathrm{LVEM}_i} = & -\frac{\mu_v}{2} \sum_{j \in V(i)} (\dot{q}_i(t) - \dot{q}_j(t))^2 \\ & -\frac{\mu_b}{2} \sum_{j \in B(i)} (\dot{q}_i(t) - \dot{r_j}(t))^2 \end{aligned}$$

where $\mu_v$ and $\mu_b$ are the azimuthal and radial viscosity, respectively; moreover, $\dot{r_j}$ is the velocity of the $j$-th barycenter (the values of such velocities are extracted from the movie). The first term concerning the kinetic energy is the same of the LEM, i.e., $L_{\mathrm{LVEM}_i} = L_{\mathrm{LEM}_i}$. Thus, after putting all together with $L = \sum_{i=1}^{n_v} L_{\mathrm{LVEM}_i}$ and $D = \sum_{i=1}^{n_v} D_{\mathrm{LVEM}_i}$, we obtain the Euler Lagrange equations

$$\begin{gathered} \frac{d}{dt}\left(\frac{\partial L}{\partial \dot{q_{i,j}}}\right) - \frac{\partial L}{\partial q_{i,j}} - \frac{\partial D}{\partial \dot{q}_{i,j}} = 0\,,\ i = 1, 2, \ldots, n_v, \\ j = 1, 2 \end{gathered}$$

and hence $2n_v$ equations with four parameters to be estimated, i.e., $K_v/m$, $K_b/m$, $\mu_v/m$, and $\mu_b/m$.

The NLVEM takes into account the possible effect of a nonlinear elastic term, namely an elastic modulus depending linearly with elongation. Hence,

in this case the Lagrangian is composed of the following contributions for mass point $i$:

$$L_{\mathrm{NLVEM}_i} = L_{\mathrm{LVEM}_i} - \frac{k_0}{3} \sum_{j \in B(i)} (q_i(t) - r_j(t) - l_{1,i,j})^3$$

$$D_{\mathrm{NLVEM}_i} = D_{\mathrm{LVEM}_i} .$$

We can proceed to compute the Euler Lagrange equations as in the previous case. The identification of the NLVEM demands the estimation of five parameters to be estimated, i.e., $K_v/m$, $K_b/m$, $\mu_v/m$, $\mu_b/m$, and $k_0/m$.

The IDLVEM is just the same of the LVEM but under the action of external forces acting on the vertices accounting for stress-independent myosin dynamics, i.e.,

$$f_i(t) = \bar{A}_i \sum_{j \in B(i)} \cos(\omega t + \phi_j) \, , \; i = 1, 2, \ldots, n_v$$

where, in order to reduce the number of parameters to estimate, the amplitude $\bar{A}_i$ is taken as the mean distance between the vertex $i$ and the neighbor barycenters in $B(i)$ and the frequency $\omega$ is considered constant for all the cells; finally, the phase $\phi_j$ is a parameter to be identified. For the other cases, the parameters optimized are those that account for elasticity and viscosity. Summing up, the parameters to find are the following: $\omega$, $\phi_1$, $\phi_2, \ldots$, $\phi_n$, $K_v/m$, $K_b/m$, $\mu_v/m$, and $\mu_b/m$.

The nonlinear elasticity of the NLVEM in the former, and the autonomous contractility of the IDLVEM are considered only in terms of radial contribution, since changes in molecular concentrations are monitored only at the center of the cells.

## 6.4 Model identification and validation

The positions of the vertices and barycenters as well as the related resting lengths can be extracted from the video sequence such as that in Figure 6.2. Movies acquired by fluorescence confocal microscopy were first pre-treated with a 2D lowpass gaussian filtering to remove high frequency random noise,

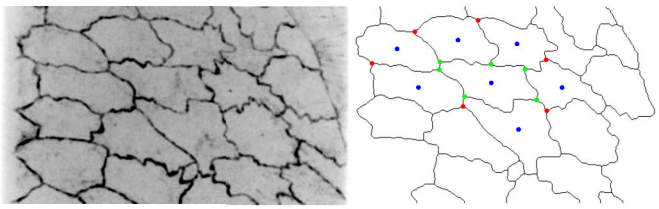

**Figure 6.2:** *Left pannel: Confocal image of Amnioserosa cells showing the apical (top) side of their membranes in dark. On the right pannel, the same picture was segmented (i.e. separated in distinct regions: the cells). In blue, the cell's barycenter, in red, the neighbor vertices, and in green, the position of the vertices to be modeled.*

followed by a top-hat filtering, to remove background signal. The pictures were then binarized thanks to a threshold, and the Euclidian distance transform of the binarized picture was computed. This pre-treatment aims at preparing the pictures for the last step of segmentation, which consists in performing a watershed transform, separating the cells present in the pictures in labeled regions. A graphic interface was developed "ad hoc" to allow the user to easily correct possible errors in the segmentation as well as to control the parameters of the pre-treatment. Once the cells are labeled as regions in the pictures, one can easily access to their center of mass (barycenter of the points contained in the region) and to the vertices (nodes of the pictures).

Based on this video processing, we have at disposal the measures of $q_i(t)$, $r_j(t)$ and $\dot{r}_j(t)$ for all $i$ and $j$ at given time instants $t = kT$ with $k = 1, 2, \ldots, K$ with uniform sampling time $T$ equal to 6 s. Let us denote such measures with $y_{q_i}(k)$, $y_{r_j}(k)$, and $\dot{y}_{r_j}(k)$ and let $y_q(k) := (q_1(k), q_2(k), \ldots, q_{n_v}(k)) \in \Re^{2n_v}$, $y_r(k) := (r_1(k), r_2(k), \ldots, r_n(k)) \in \Re^{2n}$, and $\dot{y}_r(k) := (\dot{r}_1(k), \dot{r}_2(k), \ldots, \dot{r}_n(k)) \in \Re^{2n}$. Moreover, let $l_1 := \mathrm{col}(l_{1,i,j}, i = 1, 2, \ldots, n_v, j \in V(i))$, $l_2 := \mathrm{col}(l_{2,i,k}, i = 1, 2, \ldots, n_v, k \in B(i))$, and finally $l_0 = (l_1, l_2)$.

Following the least squares approach, we may regard the discretized Euler Lagrange equations derived from either LEM or LVEM or NLVEM or IDLVEM as constraints to take into account when performing the optimiza-

tion to find the best fitting parameters. In the following, such parameters will be denoted by the vector $p$, which depends on the specific model, as described in Section 6.3. Toward this end, let us refer to the generic discretized Euler Lagrange equation given by

$$q(k+1) = F_T\left(q(k), y_r(k), \dot{y}_r(k), l_0, p\right) ,$$
$$k = 1, 2, \ldots, K-1$$

with the objective cost function

$$J = \sum_{k=1}^{K} \left(y_q(k) - q(k)\right)^2$$

to be minimized. Such constraints are obtained by the Runge-Kutta method with the variable time step. For a proper comparison with the measures, the model output was resampled to fit data sampling. Since the measures taken at time steps $k = 1, 2, \ldots, K$ have to be associated with the time sequence of the integration (denoted by $t_{\text{int}} = t_0, t_1, \ldots, t_{\text{f}}$, we link the generic integration step $t_{\text{int}}$ with the nearest integer of the ratio of the final integration time over the last data time step, i.e., $[k\, t_{\text{f}}/K]$. Thus, in the various modeling cases we need to solve the following prototype problem

$$\min_{p, q(2), \ldots, q(K)} \sum_{k=2}^{K} \left(y_q(k) - q(k)\right)^2 \tag{6.2a}$$

subject to

$$q(k+1) - F_T\left(q(k), y_r(k), \dot{y}_r(k), l_0, p\right) = 0, \tag{6.2b}$$
$$k = 1, 2, \ldots, K-1$$

$$q(1) - y_q(1) = 0\,. \tag{6.2c}$$

After identifying the best fitting parameters by solving 6.2, it is necessary to asses the validity of the resulting model by solving the problem (6.2) with some specific tools. More precisely, as usually done in identification problems, we performed the autocorrelation test of the residuals $e_z(k) = q_i(k) - \hat{q}_i(k)$ w.r.t. a given output $q_i(k)$, where $\hat{q}_i(k)$ is its prediction given

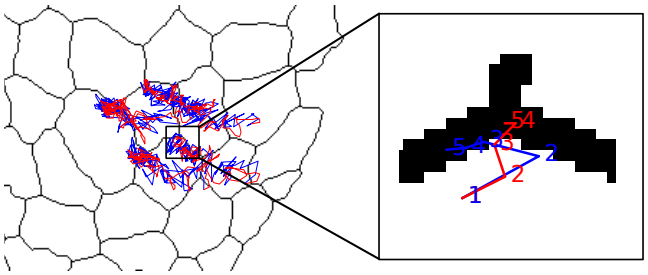


**Figure 6.3:** *In the left pannel, the last segmented movie frame ($t = 600s$), with the trajectories of each vertex. In blue, the model output, in red, the real trajectories. In the box, a close-up of one vertex, with the first five points of the model output (blue), and the real trajectories (red). The cost function calculates the sum over the whole movie of the square of the distance between each corresponding point (n°1 blue and red, n°2...).*

by the identified model, by using its autocorrelation function

$$R_z(\sigma) = \frac{\sum_{t=\sigma}^{N}(e_z(k) - \bar{e_z})(e_z(k-\sigma) - \bar{e_z})}{\sum_{t=0}^{N}(e_z(k) - \bar{e_z})^2} \tag{6.3}$$

where $\bar{e_z} = \sum_{k=1}^{K} e_z(k)/(K+1)$. The plots of (6.3) for the various identified models are shown in Figure 6.4, where the confidence bands are defined as $\pm 1.96/\sqrt{K}$. Table 6.1 reports the mean percentage of the out-of-band scores obtained by the autocorrelation functions over all the vertices.

**Table 6.1:** *Mean percentages of out-of-band points of the autocorrelation functions.*

| | LEM | LVEM | NLVEM | IDLVEM |
|---|---|---|---|---|
| % | 2.8 | 4.6 | 3.9 | 1.9 |

The results of the identification are displayed also in the form of a movie showing the position of the predicted points on the segmented movie (see Figure 6.3). The cell area extracted from the movie is also plotted versus the predicted one, as shown in Figure 6.5.

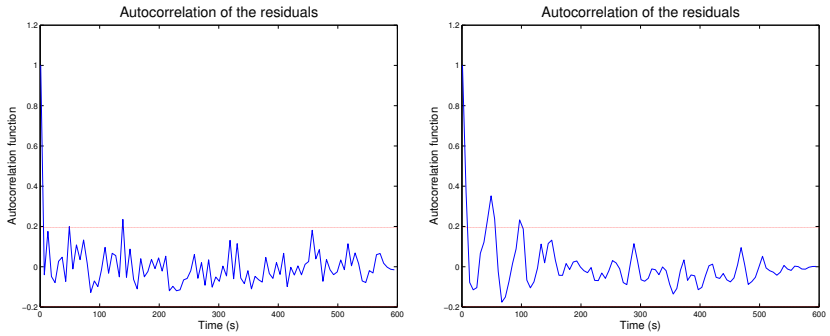


**(a)** *LEM*




**(b)** *LVEM*

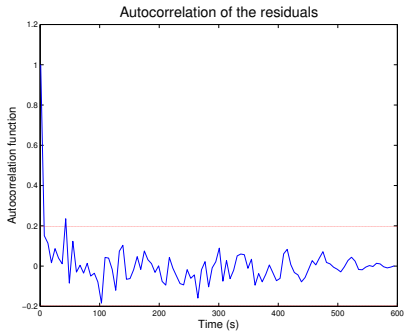


**(c)** *NLVEM*

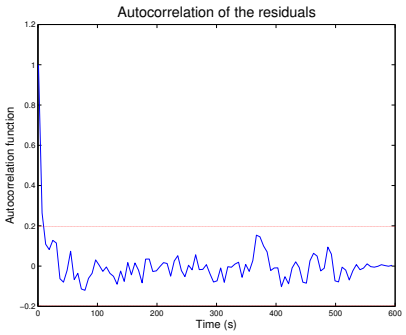


**(d)** *IDLVEM*

**Figure 6.4:** *Autocorrelation functions (the* 95% *bands are depicted with the red lines).*

Based on the results shown in Figures 6.4 -6.5 and Table 6.1, some comments are in order. First, the cellular contraction may be regarded as an autonomous mechanical phenomenon, as the cellular dynamics corresponding to the IDLVEM is inconsistent with the biological data, even though the number of points outside the confidence band is very satisfactory. Second, the LEM is also ruled out. Although it provides a rather satisfactory autocorrelation function (2.8% of out-of -band points), it displays a non periodic area variation over time and seems to be quite sensitive to noises, as shown in Figure 6.5. Third, the LVEM exhibits a large enough percentage of out-of-band points. Moreover, the corresponding cellular dynamics provides area oscillations with a rather small amplitude, which may be ascribed to abnormally high viscous parameters, as resulting from the identification. Even repeating the identification with additional constraints that keep the

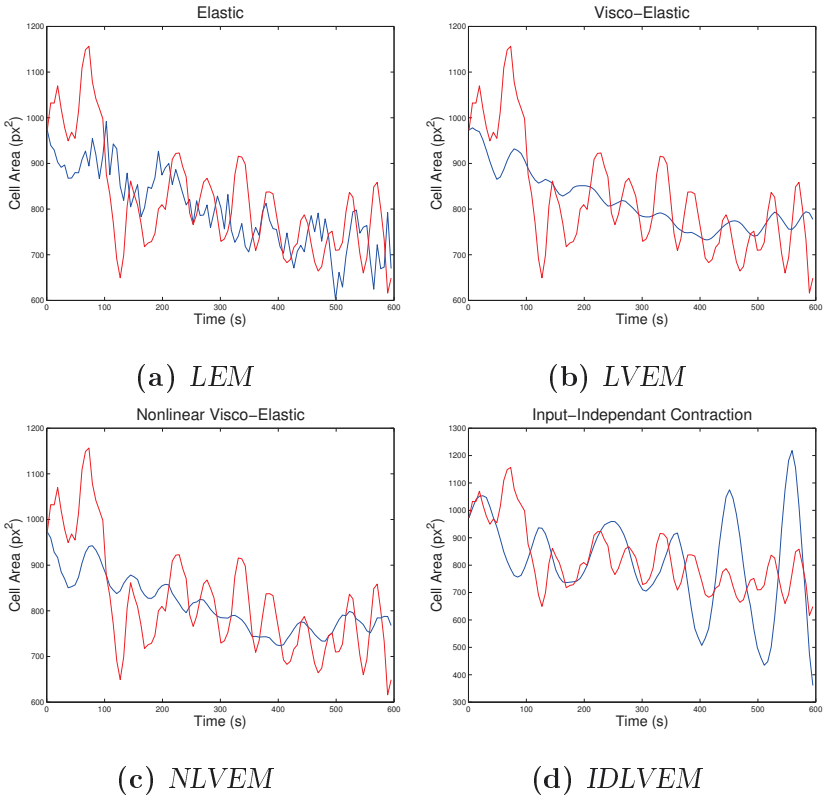


**(a)** *LEM* **(b)** *LVEM*

**(c)** *NLVEM* **(d)** *IDLVEM*

**Figure 6.5:** *Cell areas over time (red curve) and their prediction based on the identified model (blue curve).*

viscous parameters low, we obtained bad results (not shown here). Summing up, the model with the best fit appears to be the NLVEM. The prediction of cellular dynamics is more precise than any other model, and the analysis of the autocorrelation functions shows a rather satisfactory percentage of out-of-band points.

## 6.5 Conclusions

Though a lot of literature exists on modeling of cellular dynamics, very little is available on the identification of the various models proposed up to now. In this paper, we have presented the results of a complete investigation on both modeling and parameter identification of the planar dynamics of

amnioserosa cells from live images. To our knowledge, such a joint work is novel in the literature and bridges the gap between model construction and identification of the related parameters, which needs to be supported by a successful validation. Based on this framework, we have estimated the parameters of the various mechanical models and found the best fitting model, which is just that accounts for nonlinear elasticity.

Results on Dorsal Closure dynamics based on such a method are novel in the literature, even though Amnioserosa cells and Dorsal Closure dynamics have already been subject to various studies. Enabling us to discriminate between several putative mechanical behaviors for cells, this approach is thus a valuable tool to assess biological problematics.

Future work may concern the development of adaptive models that may provide an increased precision thanks to the on-line tuning. Moreover, this approach may be applied to the various cell types and fates of Dorsal Closure to uncover their variations and differences of mechanical characteristics.

# Bibliography


[1] Thomas Hunt Morgan. What are "Factors" in Mendelian Explanations? *Journal of Heredity*, (1):365–367, 1909.

[2] T. H. Morgan. SEX LIMITED INHERITANCE IN DROSOPHILA. *Science (New York, N.Y.)*, 32(812):120–2, 1910.

[3] Keith R. Benson. TIMELINE: T. H. Morgan's resistance to the chromosome theory. *Nature Reviews Genetics*, 2(6):469–474, 2001.

[4] Miko, Ilona. Thomas Hunt Morgan and the Discovery of Sex Linkage \textbar Learn Science at Scitable. *Nature Education*, 2008.

[5] Thomas Hunt Morgan. *The mechanism of Mendelian heredity*. Constable, London, 1915.

[6] H. J. Muller. Artificial Transmutation of the Gene. *Science*, 66(1699):84–87, 1927.

[7] C. Nüsslein-Volhard and E. Wieschaus. Mutations affecting segment number and polarity in Drosophila. *Nature*, 287(5785):795–801, 1980.

[8] E. Wieschaus, C. Nusslein-Volhard, and H. Kluding. Krüppel, a gene whose activity is required early in the zygotic genome for normal embryonic segmentation. *Dev. Biol.*, 104(1):172–186, 1984.

[9] José A. Campos-Ortega and Volker Hartenstein. A Summary of Drosophila Embryogenesis. In *The Embryonic Development of Drosophila melanogaster*, pages 3–8. Springer Berlin Heidelberg, 1985.

[10] José A. Campos-Ortega and Volker Hartenstein. Stages of Drosophila Embryogenesis. In *The Embryonic Development of Drosophila melanogaster*, pages 9–84. Springer Berlin Heidelberg, 1985.

[11] *PARKHURST LAB – embryo*.

[12] Thomas H. Millard and Paul Martin. Dynamic analysis of filopodial interactions during the zippering phase of Drosophila dorsal closure. *Development*, 135(4):621–626, 2008.

[13] Peter A. Lawrence, Bénédicte Sanson, and Jean-Paul Vincent. Compartments, wingless and engrailed: patterning the ventral epidermis of Drosophila embryos. *Development*, 122(12):4095–4103, 1996.

[14] Antonio Jacinto, William Wood, Tina Balayo, Mark Turmaine, Alfonso Martinez-Arias, and Paul Martin. Dynamic actin-based epithelial adhesion and cell matching during Drosophila dorsal closure. *Current Biology*, 10(22):1420–1426, 2000.

[15] Paul Martin and Susan M. Parkhurst. Parallels between tissue repair and embryo morphogenesis. *Development*, 131(13):3021–3034, 2004.

[16] W. M. Bement, P. Forscher, and M. S. Mooseker. A novel cytoskeletal structure involved in purse string wound closure and cell polarity maintenance. *J Cell Biol*, 121(3):565–578, 1993.

[17] P. E. Young, A. M. Richman, A. S. Ketchum, and D. P. Kiehart. Morphogenesis in Drosophila requires nonmuscle myosin heavy chain function. *Genes Dev.*, 7(1):29–41, 1993.

[18] D. P. Kiehart, C. G. Galbraith, K. A. Edwards, W. L. Rickoll, and R. A. Montague. Multiple forces contribute to cell sheet morphogenesis for dorsal closure in Drosophila. *J. Cell Biol.*, 149(2):471–490, 2000.

[19] Josef D. Franke, Ruth A. Montague, and Daniel P. Kiehart. Nonmuscle Myosin II Generates Forces that Transmit Tension and Drive Con-

traction in Multiple Tissues during Dorsal Closure. *Current Biology*, 15(24):2208–2221, 2005.

[20] Beth E. Stronach and Norbert Perrimon. Investigation of leading edge formation at the interface of amnioserosa and dorsal ectoderm in the Drosophila embryo. *Development*, 128(15):2905–2913, 2001.

[21] Julia A. Kaltschmidt, Nicola Lawrence, Véronique Morel, Tina Balayo, Beatriz García Fernández, Anne Pelissier, Antonio Jacinto, and Alfonso Martinez Arias. Planar polarity and actin dynamics in the epidermis of Drosophila. *Nat Cell Biol*, 4(12):937–944, 2002.

[22] Nicholas Harden. Signaling pathways directing the movement and fusion of epithelial sheets: lessons from dorsal closure in Drosophila. *Differentiation*, 70(4-5):181–203, 2002.

[23] Caroline Laplante and Laura A. Nilson. Asymmetric distribution of Echinoid defines the epidermal leading edge during Drosophila dorsal closure. *J Cell Biol*, 192(2):335–348, 2011.

[24] Adrienne R. Wells, Roger S. Zou, U. Serdar Tulu, Adam C. Sokolow, Janice M. Crawford, Glenn S. Edwards, and Daniel P. Kiehart. Complete canthi removal reveals that forces from the amnioserosa alone are sufficient to drive dorsal closure in Drosophila. *Mol. Biol. Cell*, 25(22):3552–3568, 2014.

[25] Lawrence H. Frank and Christine Rushlow. A group of genes required for maintenance of the amnioserosa tissue in Drosophila. *Development*, 122(5):1343–1352, 1996.

[26] Nicole Gorfinkiel, Guy B. Blanchard, Richard J. Adams, and Alfonso Martinez Arias. Mechanical control of global cell behaviour during dorsal closure in Drosophila. *Development*, 136(11):1889–1898, 2009.

[27] Guy B. Blanchard, Sughashini Murugesu, Richard J. Adams, Alfonso Martinez-Arias, and Nicole Gorfinkiel. Cytoskeletal dynamics and

supracellular organisation of cell shape fluctuations during dorsal closure. *Development*, 137(16):2743–2752, 2010.

[28] Sonia Muliyil and Maithreyi Narasimha. Mitochondrial ROS Regulates Cytoskeletal and Mitochondrial Remodeling to Tune Cell and Tissue Dynamics in a Model for Wound Healing. *Developmental Cell*, 28(3):239–252, 2014.

[29] Yusuke Toyama, Xomalin G. Peralta, Adrienne R. Wells, Daniel P. Kiehart, and Glenn S. Edwards. Apoptotic force and tissue dynamics during Drosophila embryogenesis. *Science*, 321(5896):1683–1686, 2008.

[30] Holley E. Lynch, Sarah M. Crews, Brett Rosenthal, Elliott Kim, Robert Gish, Karl Echiverri, and M. Shane Hutson. Cellular mechanics of germ band retraction in Drosophila. *Developmental Biology*, 384(2):205–213, 2013.

[31] Michael Brauchle, Simon Hansen, Emmanuel Caussinus, Anna Lenard, Amanda Ochoa-Espinosa, Oliver Scholz, Simon G. Sprecher, Andreas Plückthun, and Markus Affolter. Protein interference applications in cellular and developmental biology using DARPins that recognize GFP and mCherry. *Biology Open*, 3(12):1252–1261, 2014.

[32] Jerome Solon, Aynur Kaya-Çopur, Julien Colombelli, and Damian Brunner. Pulsed Forces Timed by a Ratchet-like Mechanism Drive Directed Tissue Movement during Dorsal Closure. *Cell*, 137(7):1331–1342, 2009.

[33] Aroshan K. Jayasinghe, Sarah M. Crews, David N. Mashburn, and M. Shane Hutson. Apical oscillations in amnioserosa cells: basolateral coupling and mechanical autonomy. *Biophys. J.*, 105(1):255–265, 2013.

[34] Adam C. Martin, Matthias Kaschube, and Eric F. Wieschaus. Pulsed contractions of an actin-myosin network drive apical constriction. *Nature*, 457(7228):495–499, 2009.

[35] Mauro Rauzi, Pierre-François Lenne, and Thomas Lecuit. Planar polarized actomyosin contractile flows control epithelial junction remodelling : Nature : Nature Publishing Group, 2010.

[36] Yaiza Belacortu and Nuria Paricio. Drosophila as a model of wound healing and tissue regeneration in vertebrates. *Dev. Dyn.*, 240(11):2379–2404, 2011.

[37] D. P. Kiehart. Wound healing: The power of the purse string. *Curr. Biol.*, 9(16):R602–605, 1999.

[38] Mathias Köppen, Beatriz García Fernández, Lara Carvalho, Antonio Jacinto, and Carl-Philipp Heisenberg. Coordinated cell-shape changes control epithelial movement in zebrafish and Drosophila. *Development*, 133(14):2671–2681, 2006.

[39] X. G. Peralta, Y. Toyama, M. S. Hutson, R. Montague, S. Venakides, D. P. Kiehart, and G. S. Edwards. Upregulation of Forces and Morphogenic Asymmetries in Dorsal Closure during Drosophila Development. *Biophys J*, 92(7):2583–2596, 2007.

[40] Qiming Wang, James J. Feng, and Len M. Pismen. A Cell-Level Biomechanical Model of Drosophila Dorsal Closure. *Biophys J*, 103(11):2265–2274, 2012.

[41] Luís Almeida, Patrizia Bagnerini, Abderrahmane Habbal, Stéphane Noselli, and Fanny Serman. A mathematical model for dorsal closure. *J. Theor. Biol.*, 268(1):105–119, 2011.

[42] Akiyoshi Kishino and Toshio Yanagida. Force measurements by micromanipulation of a single actin filament by glass needles. *Nature*, 334(6177):74–76, 1988.

[43] H. Kojima, A. Ishijima, and T. Yanagida. Direct measurement of stiffness of single actin filaments with and without tropomyosin by in vitro nanomanipulation. *Proceedings of the National Academy of Sciences*, 91(26):12962–12966, 1994.

[44] H. Higuchi, T. Yanagida, and Y. E. Goldman. Compliance of thin filaments in skinned fibers of rabbit skeletal muscle. *Biophys. J.*, 69(3):1000–1010, 1995.

[45] H E Huxley, A Stewart, H Sosa, and T Irving. X-ray diffraction measurements of the extensibility of actin and myosin filaments in contracting muscle. *Biophys J*, 67(6):2411–2421, 1994.

[46] Harald Felgner, Rainer Frank, and Manfred Schliwa. Flexural rigidity of microtubules measured with the use of optical tweezers. *Journal of Cell Science*, 109(2):509–516, 1996.

[47] M. Dogterom. Measurement of the Force-Velocity Relation for Growing Microtubules. *Science*, 278(5339):856–860, 1997.

[48] G. Leimbach Sato. Mechanical properties of actin. *The Journal of biological chemistry*, 260(14):8585–92, 1985.

[49] P. A. Janmey, S. Hvidt, J. Käs, D. Lerche, A. Maggs, E. Sackmann, M. Schliwa, and T. P. Stossel. The mechanical properties of actin gels. Elastic modulus and filament motions. *J. Biol. Chem.*, 269(51):32503–32513, 1994.

[50] Chauying J. Jen, Larry V. Mc Intire, and Joseph Bryan. The viscoelastic properties of actin solutions. *Archives of Biochemistry and Biophysics*, 216(1):126–132, 1982.

[51] Paul A. Janmey, Soeren Hvidt, Joyce Peetermans, Jennifer Lamb, John D. Ferry, and Thomas P. Stossel. Viscoelasticity of F-actin and F-actin/gelsolin complexes. *Biochemistry*, 27(21):8218–8227, 1988.

[52] M. L. Gardel, J. H. Shin, F. C. MacKintosh, L. Mahadevan, P. Matsudaira, and D. A. Weitz. Elastic behavior of cross-linked and bundled actin networks. *Science*, 304(5675):1301–1305, 2004.

[53] David A. Head, Alex J. Levine, and F. C. MacKintosh. Deformation of cross-linked semiflexible polymer networks. *Phys. Rev. Lett.*, 91(10):108102, 2003.

[54] Cornelis Storm, Jennifer J. Pastore, F. C. MacKintosh, T. C. Lubensky, and Paul A. Janmey. Nonlinear elasticity in biological gels. *Nature*, 435(7039):191–194, 2005.

[55] J. Xu, Y. Tseng, and D. Wirtz. Strain hardening of actin filament networks. Regulation by the dynamic cross-linking protein alpha-actinin. *J. Biol. Chem.*, 275(46):35886–35892, 2000.

[56] C. P. Broedersz, C. Storm, and F. C. MacKintosh. Nonlinear elasticity of composite networks of stiff biopolymers with flexible linkers. *Phys. Rev. Lett.*, 101(11):118103, 2008.

[57] Ning Wang, Iva Marija Tolić-Nørrelykke, Jianxin Chen, Srboljub M. Mijailovich, James P. Butler, Jeffrey J. Fredberg, and Dimitrije Stamenović. Cell prestress. I. Stiffness and prestress are closely associated in adherent contractile cells. *Am. J. Physiol., Cell Physiol.*, 282(3):C606–616, 2002.

[58] Jonathan Stricker, Tobias Falzone, and Margaret Gardel. Mechanics of the F-actin Cytoskeleton. *J Biomech*, 43(1):9, 2010.

[59] C. T. Lim, E. H. Zhou, and S. T. Quek. Mechanical models for living cells—a review. *Journal of Biomechanics*, 39(2):195–216, 2006.

[60] Karen E. Kasza, Amy C. Rowat, Jiayu Liu, Thomas E. Angelini, Clifford P. Brangwynne, Gijsje H. Koenderink, and David A. Weitz. The cell as a material. *Curr. Opin. Cell Biol.*, 19(1):101–107, 2007.

[61] Daniel A. Fletcher and R. Dyche Mullins. Cell mechanics and the cytoskeleton. *Nature*, 463(7280):485–492, 2010.

[62] M. Shane Hutson, Yoichiro Tokutake, Ming-Shien Chang, James W. Bloor, Stephanos Venakides, Daniel P. Kiehart, and Glenn S. Edwards.

Forces for Morphogenesis Investigated with Laser Microsurgery and Quantitative Modeling. *Science*, 300(5616):145–149, 2003.

[63] Xiaoyan Ma, Holley E. Lynch, Peter C. Scully, and M. Shane Hutson. Probing embryonic tissue mechanics with laser hole drilling. *Phys Biol*, 6(3):036004, 2009.

[64] Matteo Rauzi, Pascale Verant, Thomas Lecuit, and Pierre-François Lenne. Nature and anisotropy of cortical forces orienting Drosophila tissue morphogenesis. *Nat Cell Biol*, 10(12):1401–1410, 2008.

[65] G. Binnig, C. F. Quate, and Ch Gerber. Atomic force microscope. *Physical Review Letters*, 56(9):930–933, 1986.

[66] Philippe Tracqui, Alexis Broisat, Jackub Toczek, Nicolas Mesnier, Jacques Ohayon, and Laurent Riou. Mapping elasticity moduli of atherosclerotic plaque in situ via atomic force microscopy. *J. Struct. Biol.*, 174(1):115–123, 2011.

[67] Kevin D. Costa. Imaging and probing cell mechanical properties with the atomic force microscope. *Methods Mol. Biol.*, 319:331–361, 2006.

[68] N J Tao, S M Lindsay, and S Lees. Measuring the microelastic properties of biological material. *Biophys J*, 63(4):1165–1169, 1992.

[69] E. A-Hassan, W. F. Heinz, M. D. Antonik, N. P. D'Costa, S. Nageswaran, C. A. Schoenenberger, and J. H. Hoh. Relative microelastic mapping of living cells by atomic force microscopy. *Biophys. J.*, 74(3):1564–1578, 1998.

[70] M. Shane Hutson, J. Veldhuis, Xiaoyan Ma, Holley E. Lynch, P. Graham Cranston, and G. Wayne Brodland. Combining Laser Microsurgery and Finite Element Modeling to Assess Cell-Level Epithelial Mechanics. *Biophysical Journal*, 97(12):3075–3085, 2009.

[71] Mike McElfresh, Eveline Baesu, Rod Balhorn, James Belak, Michael J. Allen, and Robert E. Rudd. Combining constitutive materials modeling

with atomic force microscopy to understand the mechanical properties of living cells. *Proc. Natl. Acad. Sci. U.S.A.*, 99 Suppl 2:6493–6497, 2002.

[72] S. Ishihara, K. Sugimura, S. J. Cox, I. Bonnet, Y. Bellaïche, and F. Graner. Comparative study of non-invasive force and stress inference methods in tissue. *Eur. Phys. J. E*, 36(4):1–13, April 2013.

[73] H. Oda and S. Tsukita. Real-time imaging of cell-cell adherens junctions reveals that Drosophila mesoderm invagination begins with two phases of apical constriction of cells. *J Cell Sci*, 114(3):493–501, January 2001.

[74] Sabine C. Fischer, Guy B. Blanchard, Julia Duque, Richard J. Adams, Alfonso Martinez Arias, Simon D. Guest, and Nicole Gorfinkiel. Contractile and Mechanical Properties of Epithelia with Perturbed Actomyosin Dynamics. *PLoS One*, 9(4), 2014.

[75] Melanie Gettings, Fanny Serman, Raphaël Rousset, Patrizia Bagnerini, Luis Almeida, and Stéphane Noselli. JNK Signalling Controls Remodelling of the Segment Boundary through Cell Reprogramming during Drosophila Morphogenesis. *PLoS Biol*, 8(6):e1000390, 2010.

[76] Peter E. Hammer, Michael S. Sacks, Pedro J. del Nido, and Robert D. Howe. Mass-Spring Model for Simulation of Heart Valve Tissue Mechanical Behavior. *Ann Biomed Eng*, 39(6):1668–1679, 2011.

[77] K. Celler, I. Hödl, A. Simone, T. J. Battin, and C. Picioreanu. A mass-spring model unveils the morphogenesis of phototrophic Diatoma biofilms. *Sci Rep*, 4, 2014.

[78] H. H. Chen and G. W. Brodland. Cell-level finite element studies of viscous cells in planar aggregates. *J Biomech Eng*, 122(4):394–401, 2000.

[79] Alessandro Abate, Stéphane Vincent, Roel Dobbe, Alberto Silletti, Neal Master, Jeffrey D. Axelrod, and Claire J. Tomlin. A Mathe-

matical Model to study the Dynamics of Epithelial Cellular Networks. *IEEE/ACM Trans Comput Biol Bioinform*, 9(6):1607–1620, 2012.

[80] M. L. Gardel, F. Nakamura, J. Hartwig, J. C. Crocker, T. P. Stossel, and D. A. Weitz. Stress-dependent elasticity of composite actin networks as a model for cell behavior. *Phys. Rev. Lett.*, 96(8):088102, 2006.

[81] Marcus Otten, Wolfgang Ott, Markus A. Jobst, Lukas F. Milles, Tobias Verdorfer, Diana A. Pippig, Michael A. Nash, and Hermann E. Gaub. From genes to protein mechanics on a chip. *Nat Meth*, 11(11):1127–1130, 2014.

[82] Md Mozzammel Haque, Mihaela G. Moisescu, Sándor Valkai, András Dér, and Tudor Savopol. Stretching of red blood cells using an electro-optics trap. *Biomed Opt Express*, 6(1):118–123, 2015.

[83] Nadja Nijenhuis, Xuegen Zhao, Alex Carisey, Christoph Ballestrem, and Brian Derby. Combining AFM and Acoustic Probes to Reveal Changes in the Elastic Stiffness Tensor of Living Cells. *Biophysical Journal*, 107(7):1502–1512, 2014.

[84] Michael Murrell and Margaret L. Gardel. Actomyosin sliding is attenuated in contractile biomimetic cortices. *Mol. Biol. Cell*, 25(12):1845–1853, 2014.

[85] Melanie Norstrom and Margaret L. Gardel. Shear thickening of F-actin networks crosslinked with non-muscle myosin IIB. *Soft Matter*, 2011(7):3228–3233, 2011.

[86] G. Wayne Brodland, Vito Conte, P. Graham Cranston, Jim Veldhuis, Sriram Narasimhan, M. Shane Hutson, Antonio Jacinto, Florian Ulrich, Buzz Baum, and Mark Miodownik. Video force microscopy reveals the mechanics of ventral furrow invagination in Drosophila. *PNAS*, 107(51):22111–22116, 2010.

[87] Keith Amonlirdviman R. L. Raffard. An Adjoint-Based Parameter Identification Algorithm Applied to Planar Cell Polarity Signaling. *Automatic Control, IEEE Transactions on*, (Special Issue):109 – 121, 2008.

[88] E. M. Williams-Masson, A. N. Malik, and J. Hardin. An actin-mediated two-step mechanism is required for ventral enclosure of the C. elegans hypodermis. *Development*, 124(15):2889–2901, 1997.

[89] R. E. Keller and J. P. Trinkaus. Rearrangement of enveloping layer cells without disruption of the epithelial permeability barrier as a factor in Fundulus epiboly. *Dev. Biol.*, 120(1):12–24, 1987.

[90] Yoshihiko Shimizu, Dean Thumkeo, Jeongsin Keel, Toshimasa Ishizaki, Hiroko Oshima, Masanobu Oshima, Yoichi Noda, Fumio Matsumura, Makoto M. Taketo, and Shuh Narumiya. ROCK-I regulates closure of the eyelids and ventral body wall by inducing assembly of actomyosin bundles. *J Cell Biol*, 168(6):941–953, 2005.